A FEASIBILITY STUDY OF NON-HOMOGENEOUS SOFT MAGNETIC CORE FOR ELECTRICAL MACHINES - AN APPLICATION OF ADDITIVE MANUFACTURING

By

Thang Quoc Pham

A DISSERTATION

Submitted to
Michigan State University
in partial fulfillment of the requirements
for the degree of

Electrical Engineering - Doctor of Philosophy

2021

ABSTRACT

A FEASIBILITY STUDY OF NON-HOMOGENEOUS SOFT MAGNETIC CORE FOR ELECTRICAL MACHINES - AN APPLICATION OF ADDITIVE MANUFACTURING

By

Thang Quoc Pham

The development of a new generation of energy efficient, high torque and power density electrical machines is part of a solution toward the global energy problem. An important step in improving electrical machine performance involves optimization of the machine geometry, winding configuration, and overcoming limitations within traditional magnetic materials. In electrical machine, the magnetic iron core accounts for a significant portion of its weight and size. Under a rotating magnetic field, conventional iron cores are subjected to a non-uniform magnetic field distribution. This leads to uneven saturation distribution, extra core loss, and sub-optimal utilization of the permeability at certain regions within the iron cores. Deploying materials with non-homogeneous magnetic permeability can lead to a more uniform magnetic flux density distribution and potentially better power density. Additionally, a multi-permeability iron core, where the permeability is tuned as a function of both position and electrical machine performance, can lead to a more efficient use of the core and an additional degree of freedom for core design. This work evaluates the use of iron cores with non-homogeneous magnetic permeability for electrical machines. It is numerically demonstrated that an iron core with spatially tuned permeability can be used to manipulate the airgap flux density waveform, torque, and iron loss in electrical machines.

Exploration and exploitation of non-homogeneous iron cores for electrical machines requires an accurate, low cost modelling technique. Finite element analysis can be used to model non-homogeneous iron cores but it can lead to an expensive computational require-

ment. Traditional magnetic equivalent circuits can provide quick estimation of the electrical machine performance in comparison to finite elements. However, this technique typically models just the main flux path and/or ignores the permeability in the iron cores. In this work, a technique is developed to model non-homogeneous, multi permeability iron cores in electrical machines. It is shown that the proposed technique closely approximates finite element results and reduces the simulation time nearly 80%. It is also demonstrated that the modelling technique can be integrated into a multi-objective optimization problem for development of novel iron cores.

Additive manufacturing, also known as 3D-printing, is a layer-based manufacturing technique which can fabricate unique, complex shapes. It also has the potential to fabricate non-homogeneous iron cores. Adoption of these complex iron cores for development of high performance electrical machines requires understanding of the magnetic properties and demonstration that printed iron cores can reach variable levels of permeability. In this work, the B-H characteristics are experimentally extracted using conventional magnetic characterization techniques. A simplified magnetic anisotropy test bed was developed to quantify levels of magnetic anisotropy. It is shown that 3D-printed iron cores can achieve different levels of relative permeability and low levels of magnetic anisotropy.

Dedicated to my mother and my late father
for their love and support through this life journey

ACKNOWLEDGMENTS

First, I would like to express my sincere gratitude and appreciation to Dr. Shanelle Foster for her utmost patience, constant guidance, encouragement, and support in helping me to complete my PhD program, and to become a researcher and engineer. I'd like to also thank Dr. Elias Strangas, Dr. Patrick Kwon, and Dr. Bingsen Wang for their time, support, teaching, and guidance as part of my committee, and helped me toward completing my program.

I'd also like to thank members of the Electric Machines and Power Electronics Research (EMPowER) Laboratory at Michigan State University and the Electrical Machines and Drives Institute at TU Graz. Thank you Steve Hayslett, Matt Meier, Dr. Reemon Haddad, Dr. Andrew Babel, Cristián López-Martínez, Christiane Mellak, Dr. Annette Mütze, Abdullah Alfehaid, Anmol Aggarwal, Bhuvan Khosoo, Orwell Madovi, Ibrahim Allafi, Prathima Nuli, Dr. Heinrich Eickhoff, Dr. Hannes Grübler, Dr. Rodney Singleton, Dr. Matt Woongkul Lee, Dr. Shaopo Hwang, John Nachazel, Tia Smith, Lauren Kalizewski, Josh Ward, and Shubham Shedge. I also want to thank Dr. Truong Do, Geeta Kumari, Dr. Per Askland, and Dr. Carl Boehlert for their assistance in the field of material science. Their support helped me toward completion of my program.

I'd like to specifically thank Dr. William Jensen and Hawke Suen, who helped and assisted me on multiple projects. Their assistance aided me tremendously toward the completion of my work.

I would also like to thank members of the Department of Electrical and Computer Engineering in helping me toward the completion of my degree. Thank you Brian Wright, Gregg Mulder, Meagan Kroll, Roxanne Peacock, Michelle Stewart, and Laurie Rashid.

Additionally, I also want to express my appreciation to the Vietnam Education Foundation and the Austrian Marshall Plan Fellowship for the partial financial support during my study.

I want to dedicate my work to my mother Thuy and my late father Hoàng for all their love and support on my life journey. I would also like to express tremendous gratitude to my aunts and uncles in taking care of my mother while she's fighting against cancer, when I am far away from home.

TABLE OF CONTENTS

LIST OF TABLES

LIST OF FIGURES

Chapter 1

Introduction

The development of energy efficient electrical machines is part of a solution toward global energy and environmental problem. Over the last several decades, the advancements in designs of energy efficient machines has been propelled by computational finite element analysis. Progress in material engineering for electrical machines moves at a slower speed compared to advances in the computational speed, indicated by Moore's law. Development of future electrical machines that are more power dense and energy efficient is contingent on overcoming the limitations from traditional materials for machines [1].

Steel laminations, since the early 1900s, and soft magnetic composites, since the mid 1990s, have been traditionally used for fabrication of the iron cores in electrical machines [2]. Conventional electrical machine design includes shaping the iron cores [3]. The iron core shape, together with the non-linear characteristics of the steel, result in a non-uniform magnetic flux density distribution within the cores when subjected to rotating magnetic fields [4]. The magnetic flux path in the iron cores are also non-uniform [5]. In the stator core of a rotating radial machine, the magnetic flux path within the teeth are more radially, and are more circumferentially within the yoke. In the rotor core that employs air pockets or barriers to guide the flux, certain regions can be exposed to high stress and saturation. Magnetic materials with non-homogeneous properties can potentially yield a more uniform magnetic flux distribution and improve machine performance.

Non-homogeneous iron cores have been explored to improve performance of magnetic devices and electrical machines [6–13]. These explorations of non-homogeneous, multi-permeability iron cores have shown improvements in electrical machines. However, use of traditional manufacturing methods for fabricating such iron cores is challenging. Compared to traditional manufacturing techniques, including powder metallurgy and subtractive manufacturing, additive manufacturing (AM) can require less tooling, generate less waste, and can recycle unused raw materials. AM is capable of fast prototyping complex shapes from a wide range of materials including copper [14, 15], polymers [16], and magnetic materials [17, 18]. AM technologies have also been shown to print composite material, made from multiple materials at a same time [19], and have also been demonstrated to print materials with site specific properties [20]. Thus, AM can potentially become a method in fabricating non-homogeneous, multi-permeability iron cores. Availability of a design approach that exploits the design flexibility of 3D printing technologies for development of iron cores with non-homogeneous magnetic characteristic for electrical machine applications can lead to novel design and more efficient use of the iron cores. However, 3D finite element analysis would be required to fully explore the potential benefit of the layer-based design enabled by 3D printing technologies, which can be computationally expensive. Development of a low cost, yet accurate, modelling technique is needed, in comparison to finite element analysis (FEA).

1.1 Objective and contributions

Exploitation of iron cores with non-homogeneous magnetic characteristic for electrical machine applications can potentially enable novel design and more efficient use of the iron

cores. To adapt the potential of AM in fabricating non-homogeneous iron core, there is a need for an analytical tool that can model these structures and can also be coupled with the design process for an electrical machine, given performance requirements. This requires a modelling technique that is accurate and low cost, in comparison to finite element analysis (FEA). In this work, an analytical technique that utilizes magnetic equivalent circuit to model the non-homogeneous, multi-permeability iron core for electrical machines is proposed.

Soft magnetic iron alloy is used to process iron core. As AM potentially becomes an alternative approach in manufacturing components for electrical machine, it is important to understand its capability in printing soft magnetic iron alloys. A successful adoption of AM for the iron cores depends on the establishments of the relationships between the AM parameters and the magnetic properties of the printed parts. Given a desired magnetic characteristic such as maximum relative permeability, the ability to map back to the required printing parameters can allow machine design engineers flexibility in the material selection process. In this work, variable levels of maximum relative permeability is demonstrated with additively manufactured iron cores.

AM is a layer-based manufacturing technique. Contrast to subtractive and powder metallurgy manufacturing, AM fabricates individual layer on top of another. Thus, printed iron cores can be subjected to magnetic anisotropy, especially in the build direction or the direction of layer deposition. The selection of AM printing parameters, as well as the AM fabrication method can lead to different levels of magnetic anisotropy of the printed iron cores. Certain electrical machine topologies including axial flux machines, tubular linear machines, and claw pole machines, however, benefit from iron cores that allow easy three-dimensional flux paths, or low level of magnetic anisotropy. Magnetic anisotropy characterization of additively manufactured iron cores is thus important, since it helps AM practitioners in re-

lating printing parameters to magnetic anisotropy levels. In this work, a simplified magnetic anisotropy characterization test bed that is capable of extracting the $B - H$ magnetization curve of soft magnetic materials is developed.

In order to achieve the stated objective, the contributions of this work are:

- A demonstration that variable levels of maximum relative permeability, and low hysteresis loss can be achieved with additively manufactured soft magnetic materials
- A simplified experimental test bed that is capable of providing magnetic anisotropy characterization of soft magnetic materials, and a demonstration that additively manufactured soft magnetic materials can have a low level of magnetic anisotropy
- A technique that models a non-homogeneous, multi-permeability iron core in electrical machines via magnetic equivalent circuit
- A numerical demonstration that airgap flux density harmonic contents can be manipulated using non-homogeneous magnetic core

1.2 Organization

Investigations on non-homogeneous and multi-permeability iron cores are reviewed in chapter 2. Typical magnetic circuit design in electrical machine is then discussed to highlight the relationship between relative permeability in the iron core and the airgap flux density. Effect of non-homogeneous permeability is then demonstrated via the use of a customized finite element model. Analytical methods in estimating the airgap flux density in the machine are then discussed, following by background on traditional magnetic equivalent

circuit which is typically used to calculate the airgap flux density. In chapter 3, the development of the multi-permeability modelling technique for the iron core in electrical machine is described. The modelling technique is then applied on a simple synchronous reluctance machine (SynRM) and is verified using finite elements. The chapter concludes with the numerical demonstration on the manipulation of the airgap flux density via non-homogeneous, multi-permeability magnetic core. Background on soft magnetic materials and the standard magnetic characterization methods are given in chapter 4. Also highlighted is the current status on additively manufactured soft magnetic materials. Chapter 5 introduces the AM techniques used in this work, following by experimental results on variable levels of maximum relative permeability and low hysteresis loss of additively manufactured soft magnetic materials. Chapter 6 discusses magnetic anisotropy of soft magnetic materials. Current techniques in magnetic anisotropy testing in literature are first reviewed. The development of the simplified magnetic anisotropy characterization method is then shown and validated in 3D FEA. Experimental results show that printed iron core can achieve low level of magnetic anisotropy. Finally, chapter 7 provides potential future works and the conclusions.

Chapter 2

Background

Non-homogeneous iron cores have been used to improve performance of magnetic devices and electrical machines [6–13]. In [8], the stator yoke of an axial flux switched reluctance machine is made from non-oriented steel and the stator teeth are made from oriented steel to take advantage of higher relative permeability in the rolling direction. In [9], the stator core for the interior permanent magnet machine is made by stacking teeth and yoke segments together, where they are made from oriented steel. This non-homogeneous stator core has a different relative permeability distribution in the radial direction in comparison to the circumferential direction. For this stator the flux, thus, flows easier along the teeth and the yoke in comparison to the stator where it is made of non-oriented steel. A dual phase soft magnetic material, with bi-level of relative permeability is employed for the rotor core of interior permanent magnet machine to improve its mechanical integrity [10]. The dual phase magnetic material is also used for the stator to reduce the machine mechanical loss due to potential windage in the airgap [11]. In [12], the rotor lamination for the synchronous reluctance machine is made of a dual phase material, an illustration is shown in Figure 2.1. Here, the regions highlighted in red have a relative permeability near unity; the relative permeability in rest of the rotor lamination is near 1100. The fabrication of the non-magnetic regions is described as application of local heat treatment in a nitrogen-rich environment in pre-defined regions with certain material composition. The non-magnetic regions in the rotor

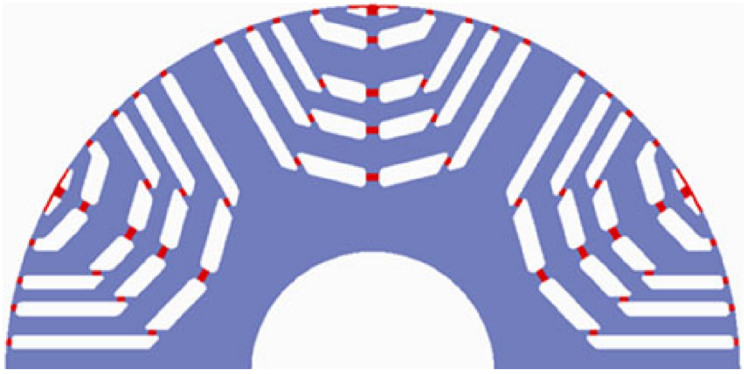

Figure 2.1: Portion of the rotor lamination for a synchronous reluctance machine. Non-magnetic regions are highlighted in red. Illustration is adapted from [12].

lamination has double the yield strength compared to the magnetic regions. The testing results show that the machine made from dual phase material has better performance than the machine made of traditional, homogeneous steel.

Application of AM for multi-material printing has shown possibilities with what can be applied toward electrical machines. According to [13], a potential advantage of non-homogeneous magnetic structures is lower manufacturing cost, with a small trade-off in magnetic performance. As a proof of concept, a material extrusion based technique is used to fabricate the stator from iron alloys, copper, and ceramic in one printing process, [21]. In [19], a 3D-printed iron core, where different material is deposited in each layer, is designed to reduce eddy current loss at high frequency. The use of aluminum alloy in the iron core structure aims at limiting and constraining the flow of eddy currents, as shown in Figure 2.2.

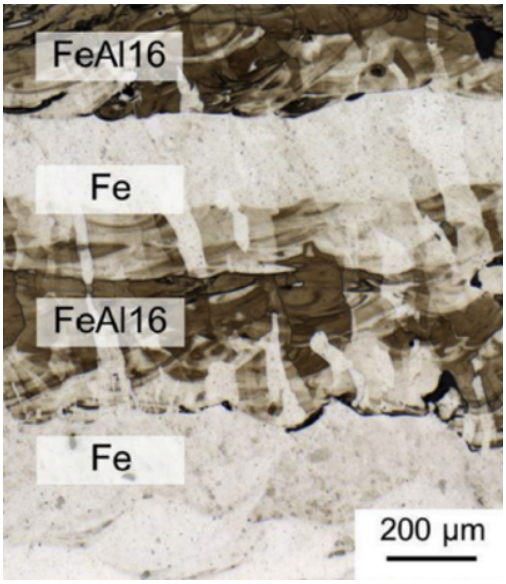

Figure 2.2: Non-homogeneous iron core processed with SLM printing technique [19].

The unique capability of AM to selectively deposit energy or material in a specific location makes it more feasible than subtractive or powder metallurgy manufacturing methods for creating non-homogeneous, multi-permeability cores. The development of non-homogeneous, multi-permeability magnetic structures can lead to new interesting design choices. In [22], AM is used to print the rotor core of a synchronous reluctance machine with non-homogeneous magnetic properties. The support struts in the rotor core, shown in Figure 2.3, are printed with low energy laser density and the rest of the rotor core is printed with higher energy laser density.

As a result, the magnetization curve of the support struts have very low relative permeability compared to rest of the rotor core. The addition of support struts with low relative permeability in the rotor can help improve its mechanical integrity under high speed application and reduce potential flux leakage at the same time. This investigation demonstrates the capability of AM for controlling the magnetic properties of the iron core in electrical machine, via site specific tuning of the printing parameters.

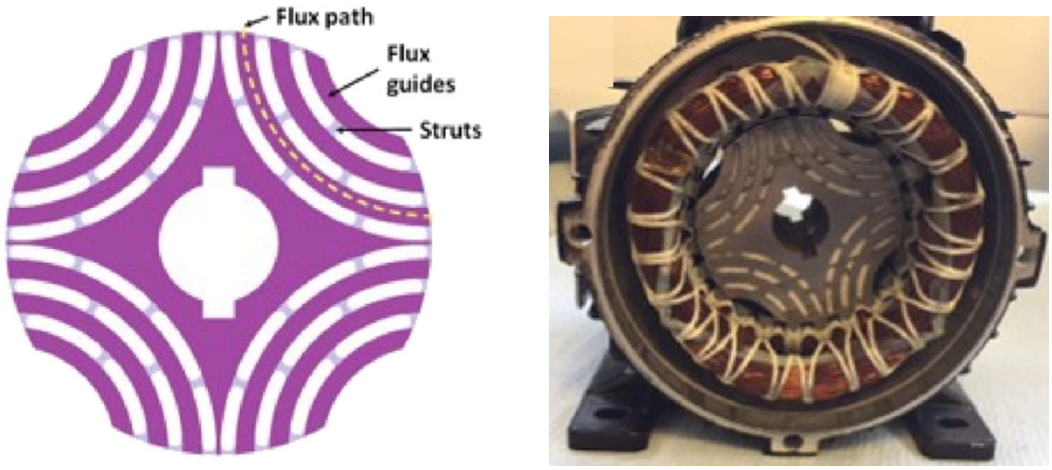

(a) (b)

Figure 2.3: a) Non-homogeneous magnetic design of the rotor core, b) Non-homogeneous 3D-printed rotor core [22].

In [20], a multi-permeability magnetic core is additively manufactured to achieve high density of inductance per DC current. This 3D printed inductor is made of three layers, with each layer having a different relative permeability, as shown in Figure 2.4. Although this multi-permeability magnetic core is proposed for power electronics application, this can be expanded to the iron cores in electrical machines.

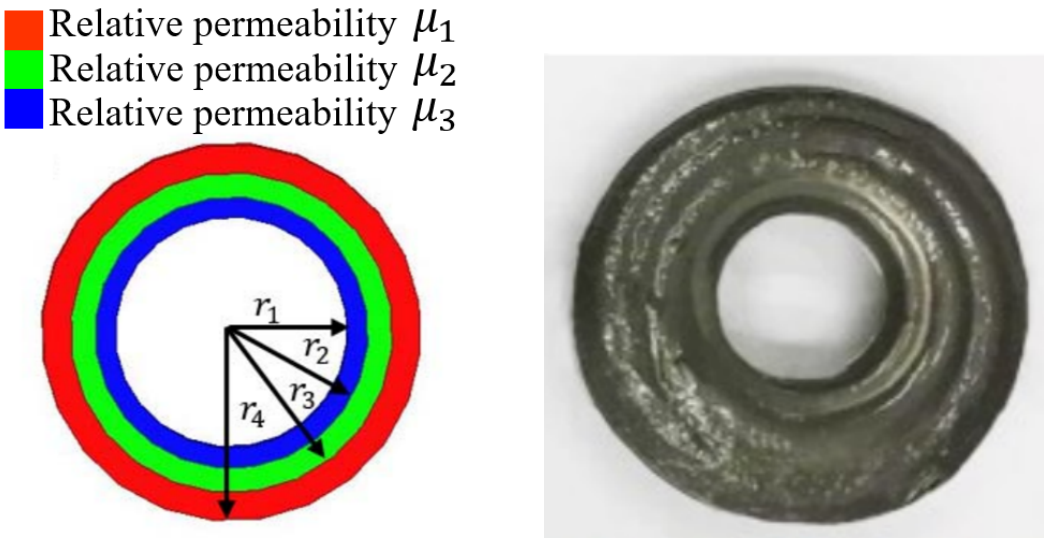

(a) Design of multi-permeability iron core. (b) Printed multi-permeability iron core.

Figure 2.4: Additively manufactured iron core for high density of inductance per DC current [20].

2.1 Magnetic circuit design

In general, the design process of an electrical machine is about applying Maxwell's equations in sizing the components making up the magnetic circuit in the machine [3]. The magnetic circuit typically includes the iron cores, the airgap, and the windings which provide magnetizing currents or current linkages. For permanent magnet machines, the magnets also contribute to the source of the current linkages, and should be included in the magnetic circuit and its sizing process.

The sizing process includes the calculation of the dimensions of the iron cores as well as the calculation of the magnetizing current. The iron core is characterized by the relationship between the magnetic flux density B and the magnetization field strength H, or the $B-H$ magnetization curve. To obtain efficient use of the iron core, machine designers base their calculations around the knee of the magnetization curve, where the material starts to saturate

[23]. A metric that represents the region around the knee point is the maximum relative permeability $\mu_{r,max}$, which is calculated from the ratio between $B/(\mu_0 H)$, where μ_0 is the vacuum relative permeability.

The sizing process depends on the magnetic field strength H and the magnetic flux density B in different sections of the electrical machine, and the associated magnetic voltage for each section. Given the magnetic circuit of the electrical machine, the current linkages Φ is equal to the sum of the magnetic voltages around the circuit. The sum $\sum_{i=1}^{k} U_{m,i}$ is equal to the line integral of the magnetic field strength H in section i along the path that makes the circuit, as shown in (2.1). Calculation of the sum $\sum_{i=1}^{k} U_{m,i}$ can be separately implemented from calculation of magnetic voltage in individual sector within the the airgap, the rotor core, the stator core.

$$\sum_{i=1}^{k} U_{m,i} = \oint_l H \cdot dl = \Phi \tag{2.1}$$

For half of the magnetic circuit of a simple electrical machine, the sum is shown as in (2.2). Here, $U_{m,\delta}$ is the magnetic voltage in one airgap, $U_{m,ry}$ and $U_{m,sy}$ are the magnetic voltages in the rotor yokes and the stator yokes, respectively, $U_{m,st}$ and $U_{m,rt}$ are the magnetic voltages in the stator and rotor teeth, respectively. The airgap magnetic voltage is related to the airgap length δ and the shape of the slots in the magnetic core, which is characterized by the Carter coefficient k_c, as shown in (2.3). Here, the fundamental and harmonics of the airgap flux density B_δ are related to the airgap slotting effect, as shown in Figure 2.5. When the open slot is inserted with magnetic wedge, the main flux can enter the teeth via the magnetic wedge, changing the harmonic contents of the airgap flux density.

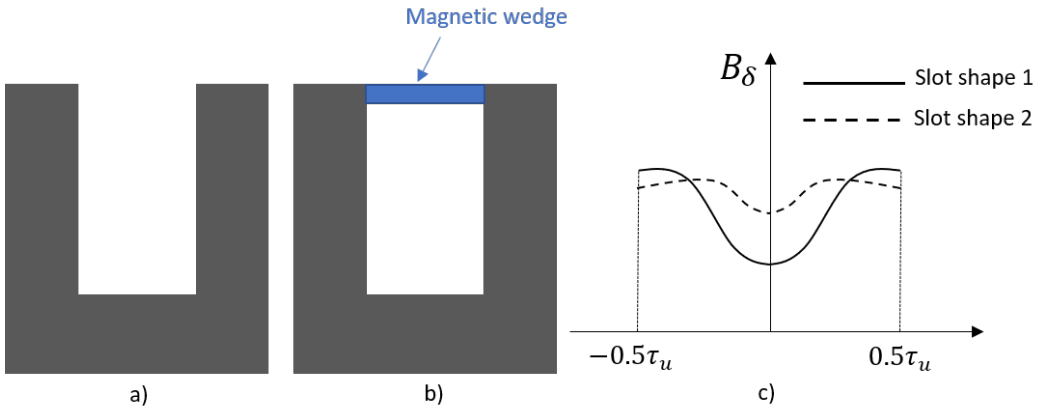

Figure 2.5: Illustration of impact of slotting effect on airgap flux density. a) Open slot shape. b) Open slot with magnetic wedge inserted. c) Airgap flux density waveforms coressponding to different slotting effects.

$$\frac{1}{2}\sum_{i=1}^{k} U_{m,i} = U_{m,\delta} + U_{m,ry} + U_{m,sy} + U_{m,st} + U_{m,rt} \tag{2.2}$$

$$U_{m,\delta} = H_\delta \cdot k_c \cdot \delta = \frac{B_\delta}{\mu_0} k_c \cdot \delta \tag{2.3}$$

Magnetic voltages in the stator and the rotor cores are related to the slot/ pole combination, the shape of the tooth or pole, and the relative permeability of the soft magnetic materials making up the magnetic cores. Magnetic voltage in the tooth is first shown to be directly related to the relative permeability of the tooth material. Assuming that the tooth is not saturated and 100% of the main flux ϕ flows through the tooth, where the tooth height is h_d, the magnetic voltage in the tooth $U_{m,t}$ can be calculated as shown in (2.4). Here, the magnetic field strength in the tooth H_t is calculated from the corresponding magnetic flux density B_t in the tooth and the relative permeability of the soft magnetic material, (2.5). Calculation of B_t is shown in (2.6) where S_t is the cross sectional area of the tooth where the flux passes through, τ_u is the slot pitch, b_d is the tooth width, L is the stack length, and

L' is the effective stack length of the magnetic core. The illustration of the process is shown in Figure 2.6.

$$U_{m,t} = \int_0^{h_d} H_t \cdot dl \tag{2.4}$$

$$H_t = \frac{B_t}{\mu_r \mu_0} \tag{2.5}$$

$$B_t = \frac{\phi}{S_t} = \frac{L' \cdot \tau_u}{L \cdot b_d} B_\delta \tag{2.6}$$

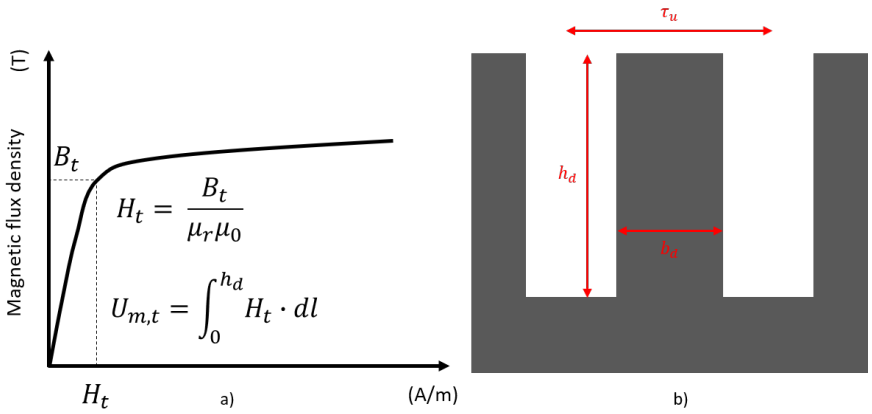

Figure 2.6: a) Calculation of the magnetic voltage in the tooth based on the magnetic characteristics of the soft magnetic material. b) Here, the tooth has an open slot structure and 100% of the flux ϕ is assumed to flow from the airgap through the tooth.

Similar to magnetic voltage in the tooth, the magnetic voltages in the stator and rotor yokes are also dependent on the relative permeability of the materials used in the magnetic cores. General estimation of the magnetic voltages in the yokes depends on the line integration of the magnetic field strengths in the yokes, as shown in (2.7). Here, H_{sy} and H_{ry} are the magnetic field strength in the stator and rotor yokes, B_{sy} and B_{ry} are the magnetic flux

densities in the yokes, and τ_{sy} and τ_{ry} represent the pole pitch of the yokes.

$$\begin{cases} U_{m,sy} = H_{sy}(\mu_r, B_{sy}) \cdot \tau_{sy} \\ U_{m,ry} = H_{ry}(\mu_r, B_{ry}) \cdot \tau_{ry} \end{cases} \tag{2.7}$$

2.2 Effect of non-homogeneous permeability

In order to demonstrate the effect between relative permeability and the airgap flux density, a customized static FEA tool is used and applied on a simple machine model as shown in Figure 2.7. Here, the model mimics four regions within an electrical machine: (1) rotor, (2) windings, (3) air gap, and (4) stator. The windings are the copper region with a defined current density, given in Table 2.1. The stator is set as electrical steel with two regions. One stator region is set with homogeneous magnetic properties. In the hatched stator region, the magnetic relative permeability can vary; however, the other magnetic properties are fixed. The y-component of the magnetic flux density, B_y, in the air gap at the red dotted line is used to evaluate the effect of non-homogeneous relative permeability. The customized FEA tool here is developed based on Galerkin approach, a special scenario of the method of weighted residuals, only models and evaluates half of a pole. Detail of the customized FEA is shown in the Appendix A.

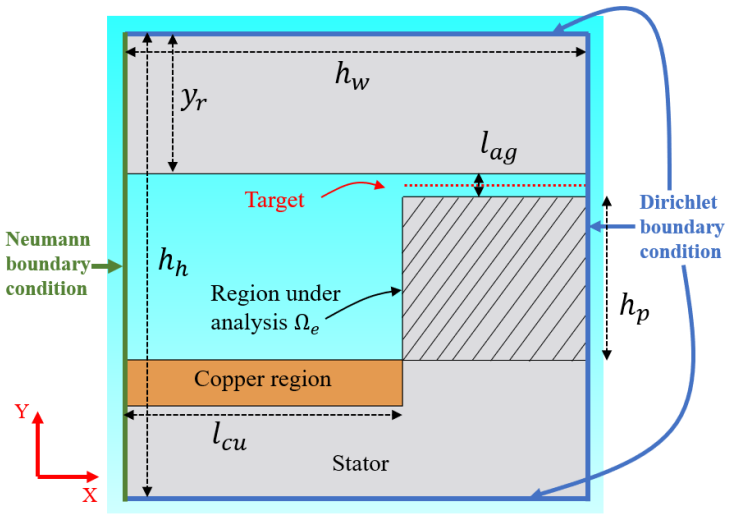

Figure 2.7: Illustration of model used for evaluation. A symmetry boundary conditions applied at the right edge. Dimensions here are drawn to scale.

Table 2.1: Parameters used in the finite element model.

Parameter	**Value**
Model width (h_w)	100 mm
Pole height (h_p)	20 mm
Coil width (l_{cu})	60 mm
Air gap length (l_{ag})	20 mm
Current density	8 A/mm^2
Fixed relative permeability	2000
Relative permeability range	1 - 4000

A case study is presented to demonstrate that air gap flux density in an electrical machine can be changed by varying relative permeability within the magnetic core, identified by the shaded region in Figure 2.7. Here, the relative permeability of the hatched region can vary between 1 to 4000. As expected, the flux lines are diverted where μ_r is low, as shown in

Figure 2.9. This leads to B_y with higher harmonic content in the air-gap region above the stator pole, as shown in Figure 2.10.

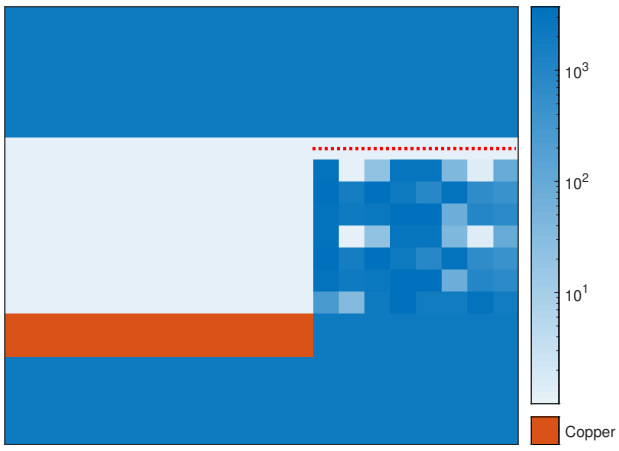

Figure 2.8: Random relative permeability distribution in the hatched region. B_y is evaluated in the air gap at the red dotted line.

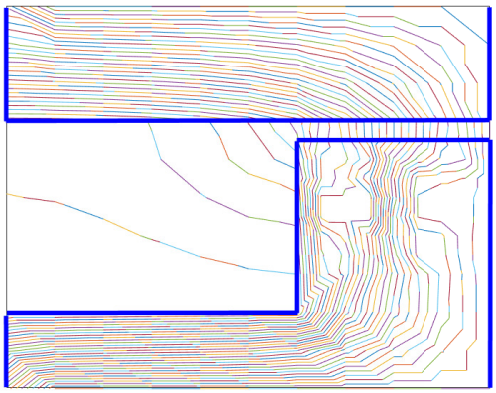

Figure 2.9: Flux line contour plot under magnetostatics analysis.

Although this case study is simple, it highlights the possibility of manipulating the airgap flux density waveform by manipulating the relative permeability distribution in the iron core. This method can be implemented using a commercial FE software or a customized FE software. The use of a FE software, however, requires high computational effort. A different modelling technique that can cut down the computational effort while maintaining

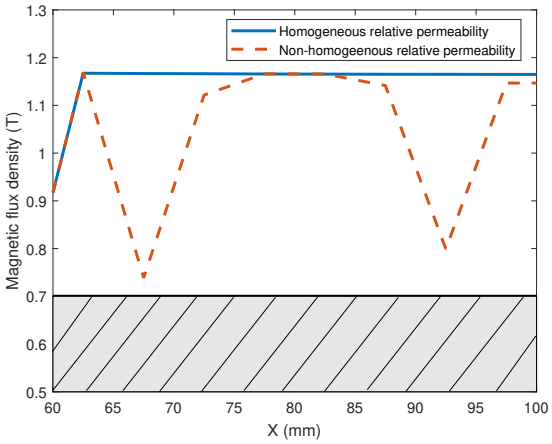

Figure 2.10: B_y at the dotted target line in the air gap with non-homogeneous magnetic relative permeability in the stator pole.

the accuracy in estimating the airgap flux density is important.

2.3 Airgap flux density estimation

The airgap flux density can be estimated using two approaches: (1) Combined airgap/ permeance and (2) Superposition & magnetic circuit. For illustration, the airgap flux density is estimated for the simple synchronous reluctance machine shown in Figure 2.11.

2.3.1 Combined airgap/ permeance

The airgap flux density is the product of the stator MMF and the permeance of the machine at the airgap. The permeance of the machine accounts for both the stator and rotor saliency.

2.3.1.1 Stator MMF

The stator MMF is a function of space and time, and is dependent on the stator current and the winding function for each phase. For a stator windings with n phases, the total

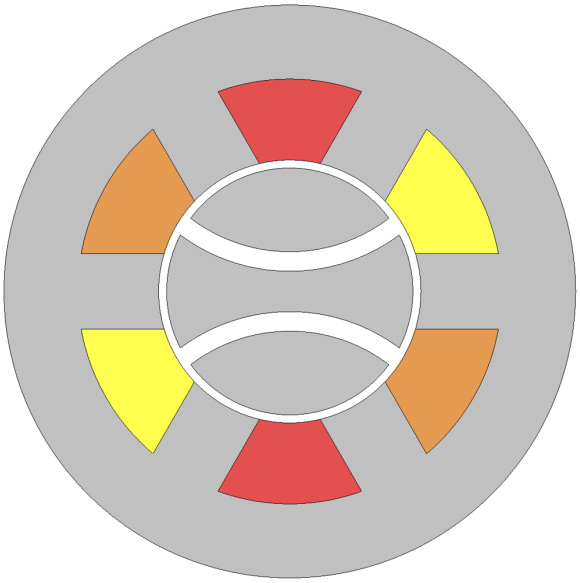

Figure 2.11: Illustration of a simple synchronous reluctance machine.

stator MMF $F_s(\theta, t)$ in stator reference frame is the sum of individual phase MMF, as shown in Equation (2.8). Here, $N_i(\theta)$ is the winding function of phase i, θ is the angle displacement with respect to the stator reference axis, and $I_i(t)$ is the instantaneous current flown in phase i. The winding function for each phase can be expressed as a step function, representing the discrete distribution of winding in each slots. Given the distribution of the winding of phase a as shown in Figure 2.12, the corresponding phase MMF $F_a(\theta, t)$ is the product between the winding function for phase a and the current flown in phase a, as shown in Figure 2.13.

$$F_s(\theta, t) = \sum_{i=1}^{n} N_i(\theta) \cdot I_i(t) \tag{2.8}$$

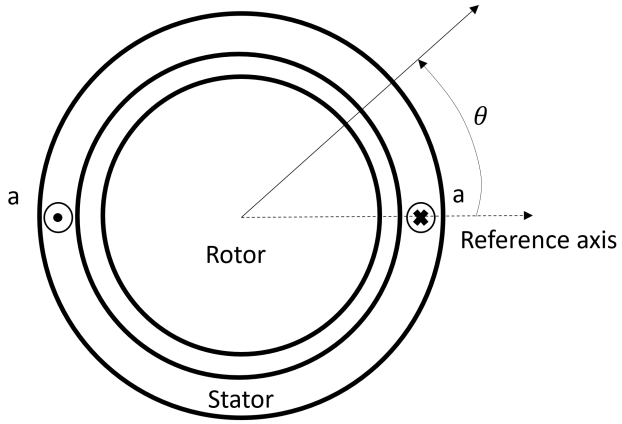

Figure 2.12: Simplified stator winding distribution in a machine and the reference axis.

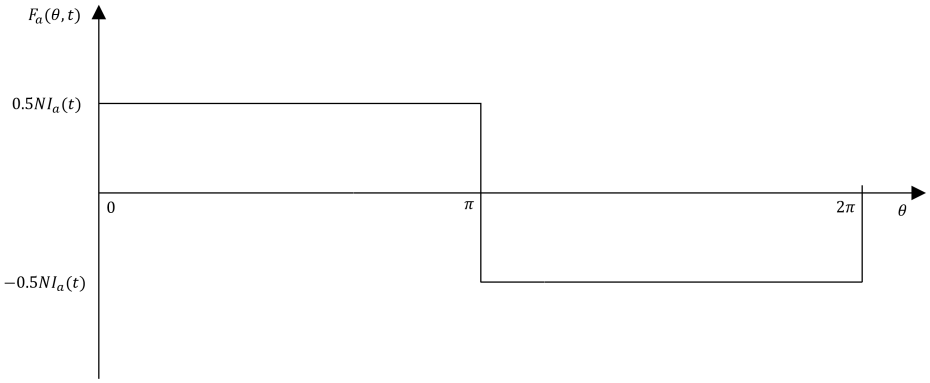

Figure 2.13: The stator MMF of phase a with respect to the reference axis.

Fourier series can then be used to approximate the step function phase MMF shown in Figure 2.13. Assuming a machine with three phase currents, each phase is displaced by 120^o as shown in (2.9), the corresponding Fourier series for each phase MMF is shown in (2.10). Here, I_m is the maximum current in each phase, w is the fundamental frequency for the rotor, δ is the current displacement angle that can provide maximum torque, and ϕ is the function of angle displacement θ with respect to the stator reference axis. The number of effective turns for each phase is N, where $N = k_w N_{ph}$ with k_w as the winding factor and N_{ph} as the number of turns per phase. The total stator MMF is then the summation of the individual phase MMF, as shown in (2.11). Figure 2.14 shows the Fourier series approximation for the

square wave MMF in Figure 2.13.

$$\begin{aligned} I_u(t) &= I_m \sin(wt + \delta) \\ I_v(t) &= I_m \sin(wt + \delta - \frac{2\pi}{3}) \\ I_w(t) &= I_m \sin(wt + \delta + \frac{2\pi}{3}) \end{aligned} \tag{2.9}$$

$$\begin{aligned} F_u(\theta, t) &= \sum_{n=1,3,5...}^{\infty} \frac{4NI_u(t)}{2\pi n} \sin(n(\theta + \phi)) \\ F_v(\theta, t) &= \sum_{n=1,3,5...}^{\infty} \frac{4NI_v(t)}{2\pi n} \sin(n(\theta + \phi - \frac{2\pi}{3})) \\ F_w(\theta, t) &= \sum_{n=1,3,5...}^{\infty} \frac{4NI_w(t)}{2\pi n} \sin(n(\theta + \phi + \frac{2\pi}{3})) \end{aligned} \tag{2.10}$$

$$F_s(\theta, t) = F_u(\theta, t) + F_v(\theta, t) + F_w(\theta, t) \tag{2.11}$$

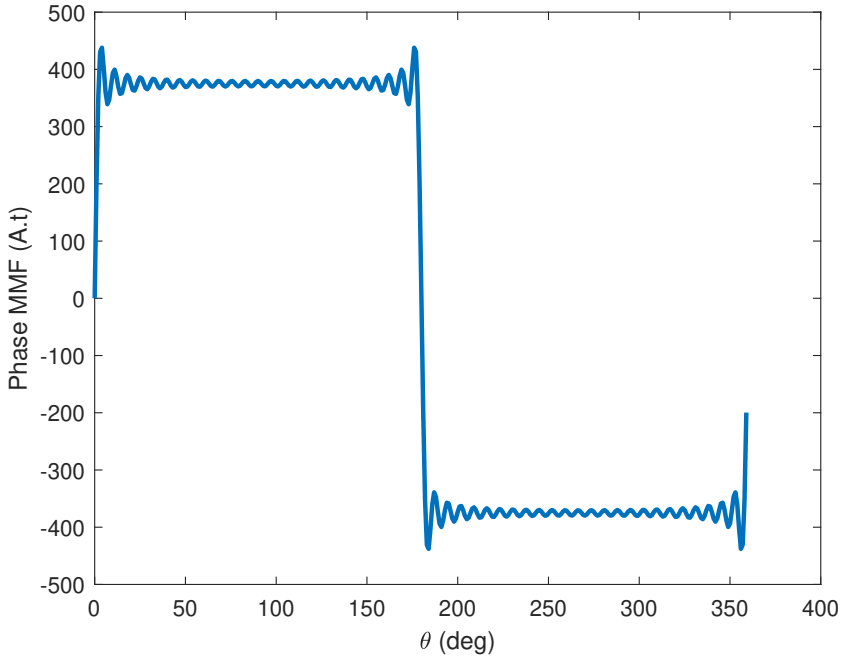

Figure 2.14: Fourier series approximation of stator MMF of phase a with respect to the reference axis.

2.3.1.2 Stator saliency

The stator slotting effect contributes to the stator saliency of electrical machines. Pure sinusoidal function can be used to approximate the stator slotting effect, given the information of the slots and the airgap length. Figure 2.15 shows the inverse airgap function $g^{-1}(\theta)$ of the electrical machine, assuming that the rotor is smooth and exhibiting zero saliency. The inverse airgap function varies between minimum value g_{min}^{-1} and maximum value g_{max}^{-1}, and are calculated as shown in (2.12). Here, g is the machine airgap length, where β is a coefficient defined as in (2.13). The mechanical angle α_s is defined as the ratio between the slot opening width τ_s and the airgap radius R.

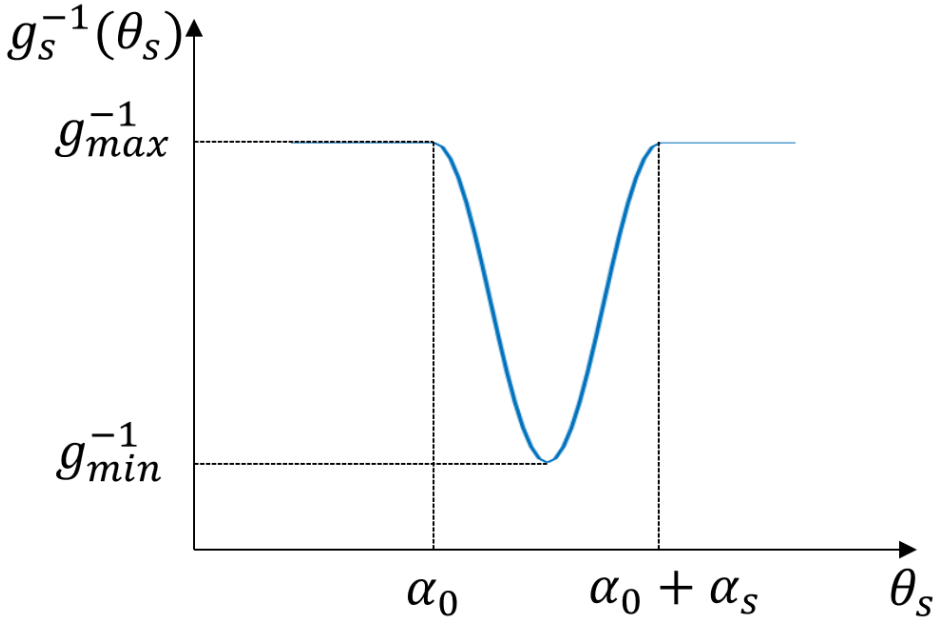

Figure 2.15: Inverse airgap function of an electrical machine accounting for the slot. Here the assumption is that the rotor is smooth with zero saliency.

$$\begin{aligned} g_{max}^{-1} &= \frac{1}{g} \\ g_{min}^{-1} &= \frac{1-2\beta}{g} \end{aligned} \tag{2.12}$$

$$\begin{aligned} u &= \frac{\tau_s}{2g} + \sqrt{1 + \left(\frac{\tau_s}{2g}\right)^2} \\ \beta &= \frac{1 + u^2 - 2u}{2(1+u^2)} \end{aligned} \tag{2.13}$$

The inverse airgap function over a slot pitch can then be calculated as shown in (2.14), with the mechanical angle α_t is the ratio between the tooth span and the airgap radius. The coefficients A and B are calculated as $A = (g_{min}^{-1} + g_{max}^{-1})/2$ and $B = (g_{max}^{-1} - g_{min}^{-1})/2$. The inverse airgap function over the entire machine circumference with respect to the stator

reference axis is illustrated in Figure 2.16, assuming there are six slots in the stator.

$$g_s^{-1}(\theta_s) = \begin{cases} g_{max}^{-1} \text{ if } \theta_s \leq \alpha_0 \text{ or } \alpha_0 + \alpha_s \leq \theta_s \\ A + B\cos\left[\frac{2\pi}{\alpha_s}\left(\theta_s - \frac{\alpha_t}{2}\right)\right] \text{ if } \frac{\alpha_t}{2} \leq \theta_s < \frac{\alpha_t}{2} + \alpha_s \end{cases} \tag{2.14}$$

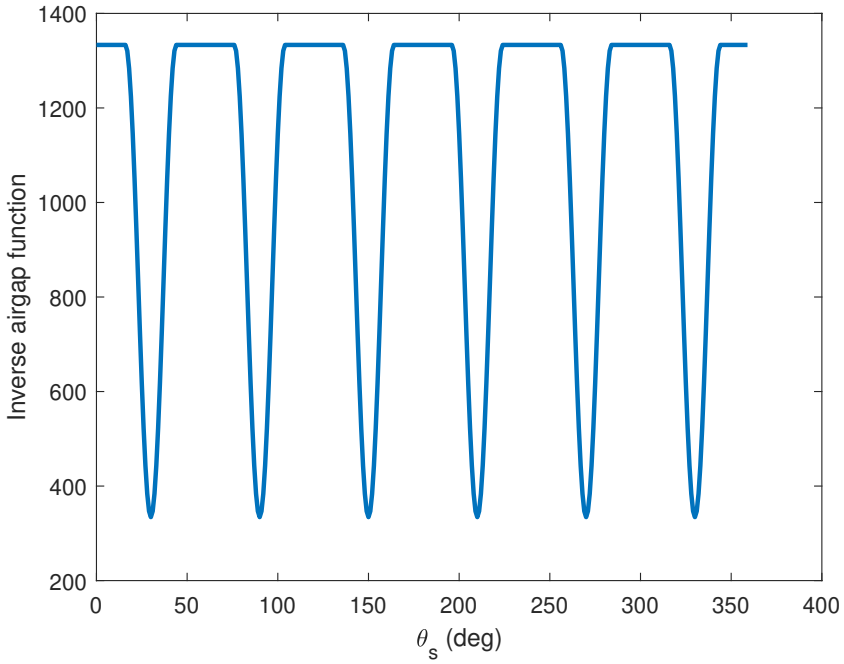

Figure 2.16: Inverse airgap function of an electrical machine accounting for the stator slots over the circumference of the airgap. Here the assumption is that the rotor is smooth with zero saliency. The inverse airgap function is referenced to the stator frame.

2.3.1.3 Rotor saliency

In SynRM, the rotor typically employs flux barriers to generate saliency. The reluctance torque is the result between the interaction of the stator MMF and the combined saliency between the stator and the rotor. Assuming a smooth stator with zero saliency, the inverse airgap function for the simple rotor with a single flux barrier per pole in Figure 2.17 is shown in Figure 2.18. Formulation of the inverse airgap function on the stator reference frame is

shown in (2.15). The conversion to the rotor reference frame requires θ_r, which is the angle displacement on the rotor circumference with respect to the d-axis of the rotor. The angle θ_r is related to the stator reference frame via $\theta_r = \theta_s - \theta_m$ with θ_m as the rotor position with respect to the stator reference frame.

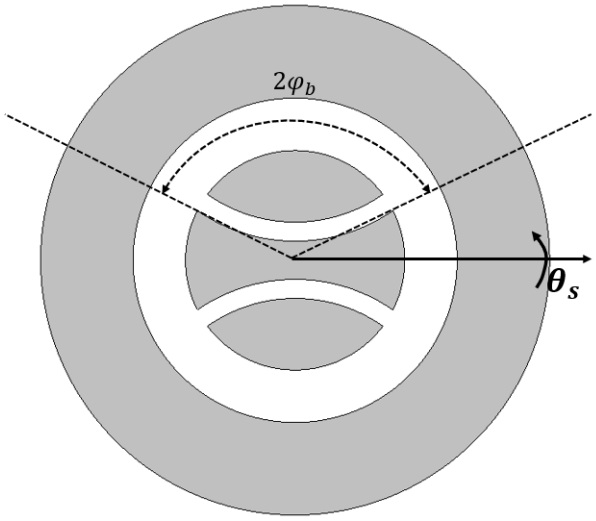

Figure 2.17: Simple SynRM rotor with a single flux barrier per pole. Here, the stator is assumed to be smooth with zero saliency. Airgap is not drawn to scale.

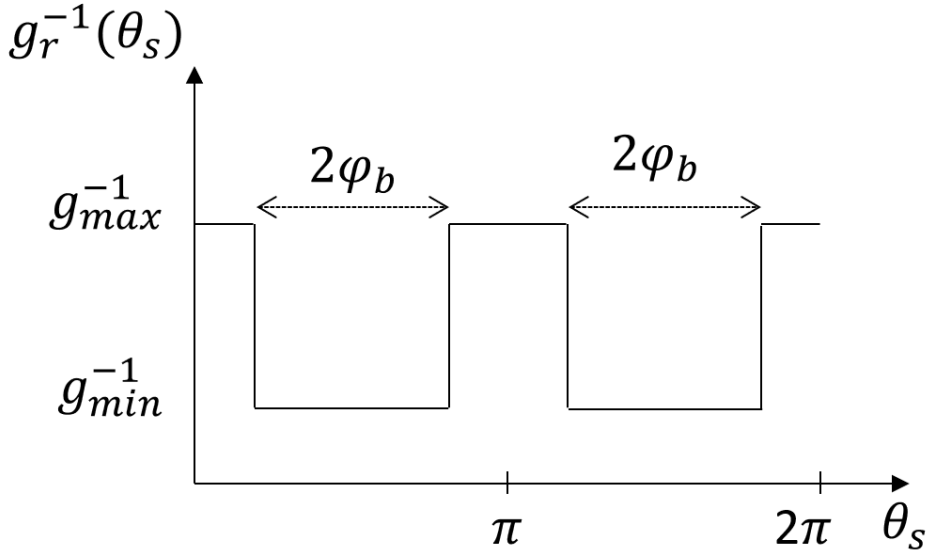

Figure 2.18: Inverse airgap function assuming a smooth stator with zero saliency.

The variation between the minimum and the maximum inverse airgap flux values are

defined as in (2.15), where $2\varphi_b$ is the mechanical spanning angle of each flux barrier. Here, T_b is the additional airgap length due to the flux barrier effect. Exact calculation of T_b is dependent on the rotor geometry and the barrier thickness, and can be found via [24]. Fourier series can be used to approximate the inverse airgap function in Figure 2.18, as shown in (2.16). Figure 2.19 shows the Fourier series expansion of the simple rotor in Figure 2.17, assuming $2\varphi_p = 130^o$ is the arc accounting for the barrier span in one pole.

$$g_r^{-1}(\theta_s) = \begin{cases} g_{min}^{-1} = \frac{1}{g+T_b} \text{ if } \{\pi/2 - \varphi_b \leq \theta_s \leq \pi/2 + \varphi_b\} \text{ or } \{3\pi/2 - \varphi_b \leq \theta_s \leq 3\pi/2 + \varphi_b\} \\ g_{max}^{-1} = \frac{1}{g} \text{ elsewhere} \end{cases} \tag{2.15}$$

$$\begin{aligned} g_r^{-1}(\theta_s) &= \frac{\pi - 2\varphi_b}{\pi} g_{max}^{-1} + \frac{2\varphi_b}{\pi} g_{min}^{-1} + \sum_{k}^{2,4,6,\ldots} a_n \cos(n\theta_s) \\ a_n &= \frac{4\pi}{n} \cos(\frac{n\pi}{2}) \Big\{ g_{min}^{-1} \sin(n\varphi) - g_{max}^{-1} \sin(n\varphi) \Big\} \end{aligned} \tag{2.16}$$

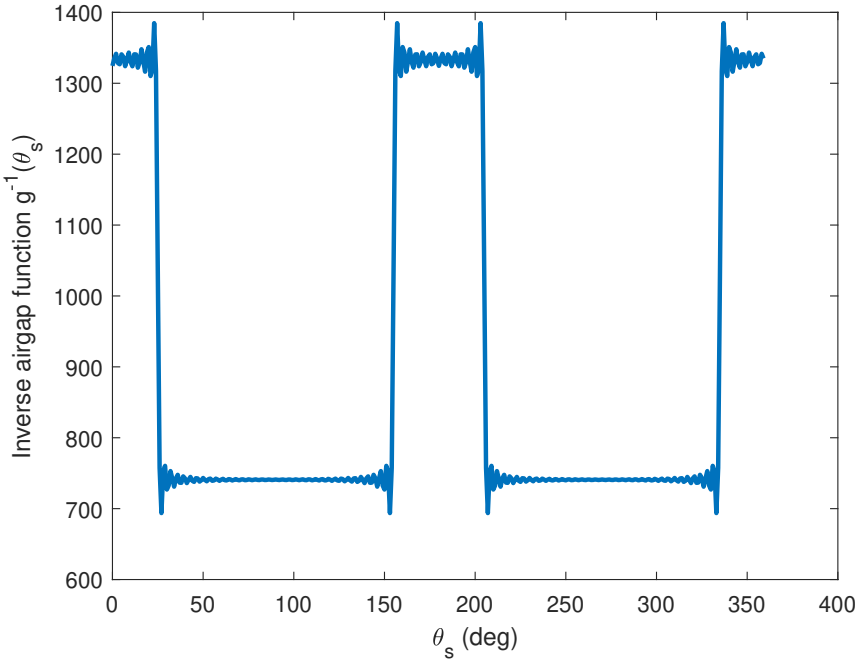

Figure 2.19: Fourier series expansion of the inverse airgap function due to rotor saliency.

2.3.1.4 Airgap flux density

The airgap flux density is the product between the stator MMF and the combined permeance of the machine. At time instant t_0, the airgap flux density calculation is shown in (2.17). The combined permeance of the machine in the stator reference frame at time t_0 is shown in (2.18), recalling that $g_s(\theta)$ is the airgap function assuming zero saliency in the rotor, and $g_r(\theta - \theta_m)$ is the airgap function assuming zero saliency in the stator. Here, L is the machine stack length and W is the width of the flux path.

$$B_g(\theta, t_0) = F_s(\theta, t_0) \cdot P(\theta, t_0) \tag{2.17}$$

$$P(\theta, t_0) = \frac{1}{R_{tot}(\theta, t_0)} = \frac{\mu_0 \cdot W \cdot L}{g_s(\theta) + g_r(\theta - \theta_m(t_0)) - g} \tag{2.18}$$

2.3.2 Superposition & magnetic circuit

According to (2.15), the exact calculation of the rotor inverse airgap function depends on the exact calculation of T_b following [24]. This is a complex process that requires tuning and details understanding of the rotor geometry. The approach of superposition & magnetic circuit can simplify the calculation of the airgap flux density, in (2.17). The process can be described as following:

1. Calculation of the airgap flux density not accounting for the stator and rotor saliency
2. Modify the airgap flux density accounting only for the stator saliency or slotting effect
3. Subtracting the airgap flux density in the previous step with the airgap flux density due to the MMF drop in the rotor barrier

The airgap flux density in step 1/ can be calculated via $B_g(\theta_s) = \mu_0 F_s(\theta_s)/g$ and is shown in Figure 2.21, assuming unit stack length and width. Here, the stator MMF can be calculated following section 2.3.1.1, and is shown in Figure 2.20. The airgap flux density in step 2/ can then be calculated, following $B_g(\theta_s) = \mu_0 F_s(\theta_s)/g_s(\theta_s)$. The airgap function $g_s(\theta_s)$ can be calculated following section 2.3.1.2. Comparison with commercial FEA software shows a close match, as illustrated in Figure 2.22.

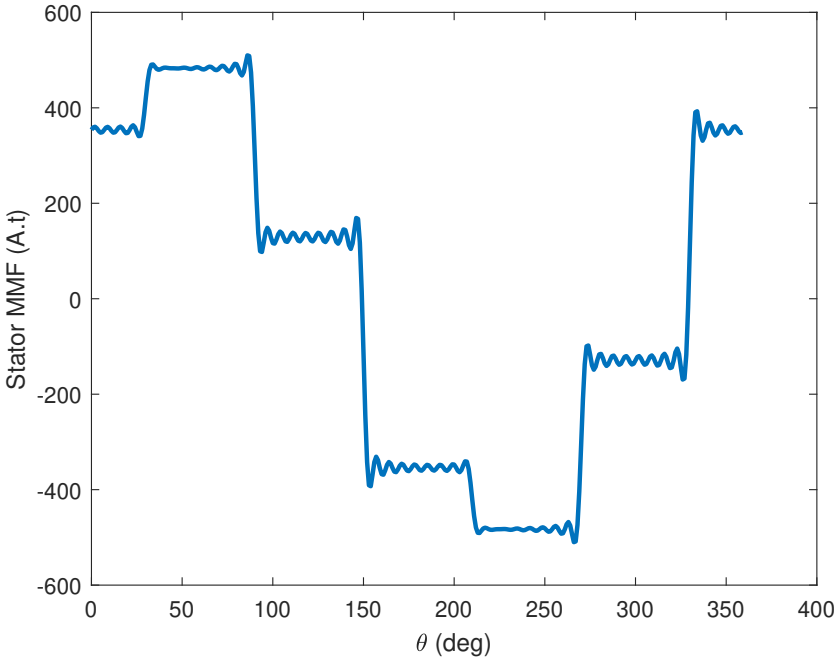

Figure 2.20: Stator MMF at time t_0 with $I_u = -0.26\hat{I}$, $I_v = -0.71\hat{I}$, $I_w = 0.97\hat{I}$.

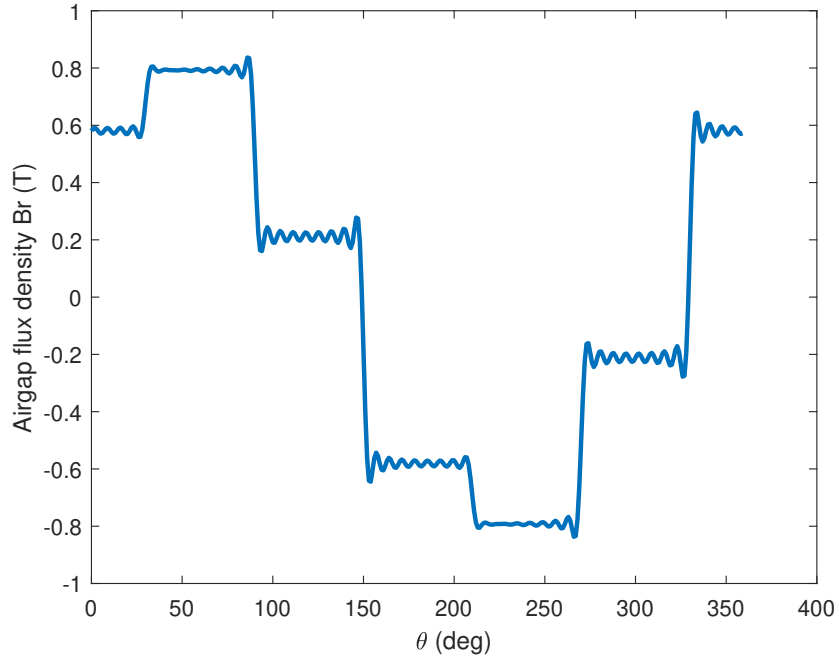

Figure 2.21: Airgap flux density neglecting saliency.

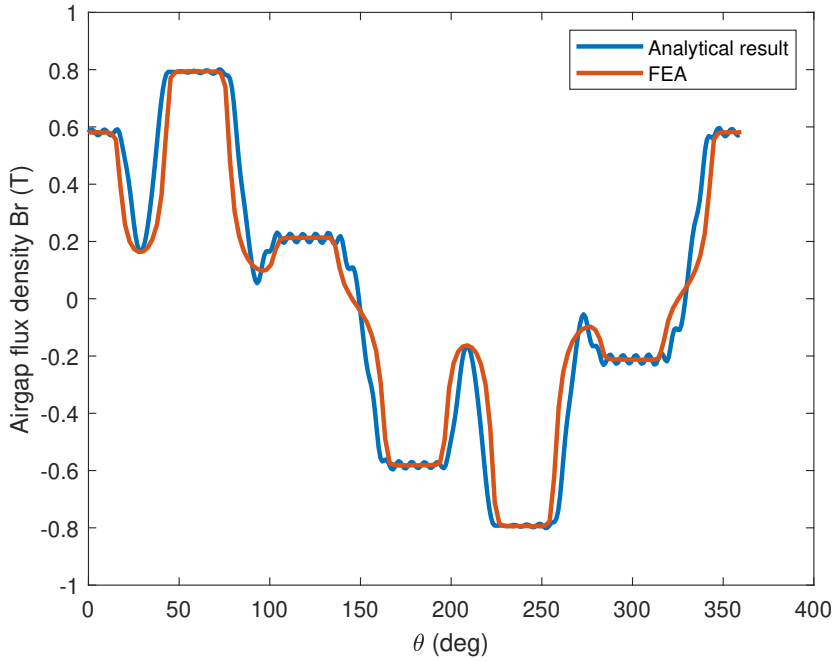

Figure 2.22: Airgap flux density accounting for stator saliency only, at time t_0 with $I_u = -0.26\hat{I}$, $I_v = -0.71\hat{I}$, $I_w = 0.97\hat{I}$.

To account for the MMF drop due to the rotor flux barrier, a magnetic equivalent circuit representing a simple SynRM in Figure 2.23 is utilized. Here, the circuit assumes infinite relative permeability in the iron cores, with $R_g = g/\mu_0$ as the airgap reluctance accounting for no saliency, F_b is the stator MMF when it sees the flux barrier, and F_a is the stator MMF when it does not see the flux barrier. The reluctance over the flux barrier can be calculated as $R_b = t_b/\mu_0$, with t_b as the barrier thickness. The corresponding magnetic equivalent circuit for Figure 2.23 is shown in Figure 2.24.

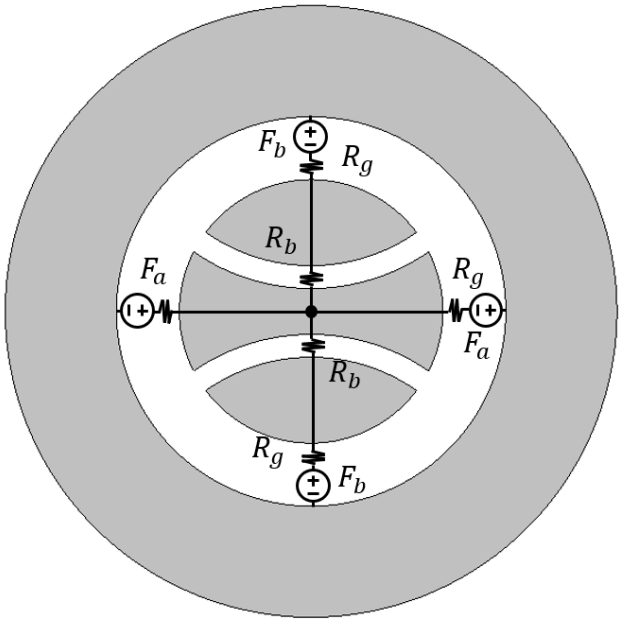

Figure 2.23: Simplified SynRM and magnetic equivalent circuit. Here, the iron cores are assumed with infinite relative permeability. Airgap is not drawn to scale.

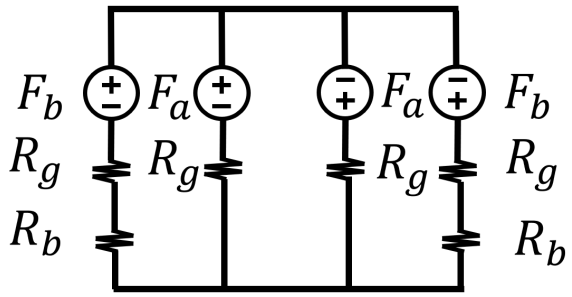

Figure 2.24: Simpified magnetic equivalent circuit. Here, the iron cores are assumed with infinite relative permeability.

$$\Delta F = \frac{|F_b| \cdot R_b}{R_g + R_b} \tag{2.19}$$

$$F_b(t) = \frac{1}{2\varphi_b} \int_{\frac{\pi}{2}-\varphi_b}^{\frac{\pi}{2}+\varphi_b} F_s(\theta, t) \cdot g \cdot g_s^{-1}(\theta) \cdot d\theta \tag{2.20}$$

The MMF drop due to the flux barrier is calculated as in (2.19), where the scalar value F_b

is calculated as shown in (2.20). The airgap flux density, in stator reference frame, accounting for MMF drop in the rotor is calculated as in (2.21). Comparison between analytical solution and FEA shows a close match, as illustrated in Figure 2.25

$$B_g(\theta,t) = \begin{cases} (F_s(\theta,t) - \Delta F(t)) \cdot \mu_0 \cdot g_s^{-1}(\theta) \text{ if } \{\pi/2 - \varphi_b \leq \theta \leq \pi/2 + \varphi_b\} \\ (F_s(\theta,t) - \Delta F(t)) \cdot \mu_0 \cdot g_s^{-1}(\theta) \text{ if } \{3\pi/2 - \varphi_b \leq \theta \leq 3\pi/2 + \varphi_b\} \\ F_s(\theta,t) \cdot \mu_0 \cdot g_s^{-1}(\theta) \text{ elsewhere} \end{cases} \tag{2.21}$$

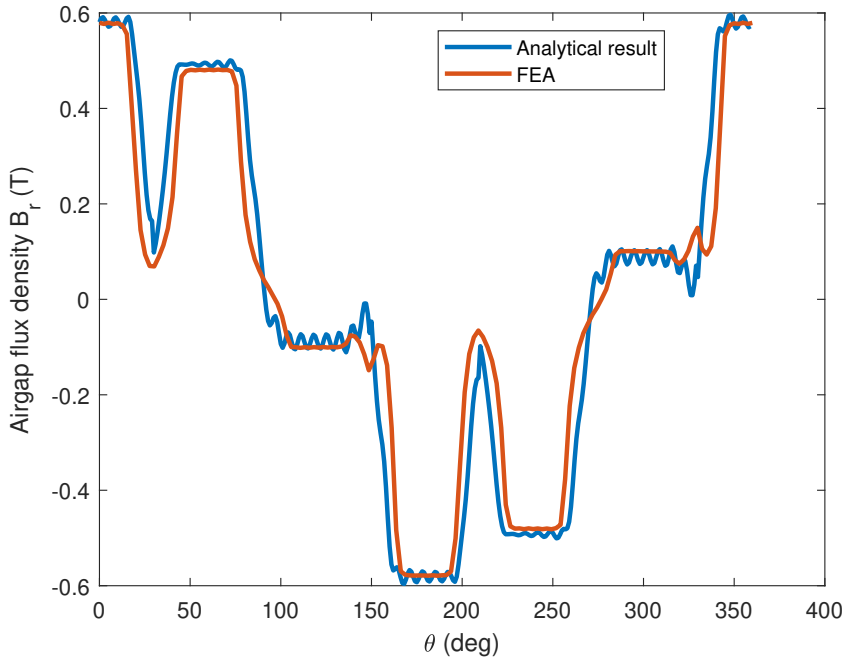

Figure 2.25: Analytical calculation of airgap flux density accounting for both stator and rotor saliency at time t_0 with $I_u = -0.26\hat{I}$, $I_v = -0.71\hat{I}$, $I_w = 0.97\hat{I}$.

2.4 Magnetic equivalent circuit

The previous approach in developing a customized FEA program to model the non-homogeneous, multi-permeability iron core for the electrical machine is cumbersome. It amplifies the need for a simpler analytical method that can provide high accuracy in analyzing and modelling non-homogeneous, multi-permeability iron core.

Prior to the use of FEA in designing electrical machines, the magnetic equivalent circuit (MEC) has been used as a design tool to represent the main flux path in the machine, [25]. The MEC uses electric components such as resistance and voltage source to represent magnetic components such as reluctance and the magnetomotive force (MMF). In MEC, the reluctance components hold the information on the geometry of the main components for the electrical machine, including but not restricted to the stack length, the iron core back iron thickness, tooth width, magnet height and width, etc. Figure 2.26 in [25] shows the MEC representing the main flux path for an interior permanent synchronous machine. Here, the reluctances for the rotor and stator iron cores can be represented with saturating elements. Reluctance elements in the airgap and the magnets are represented with non-saturating elements. The MEC here assumes homogeneous iron cores and magnets.

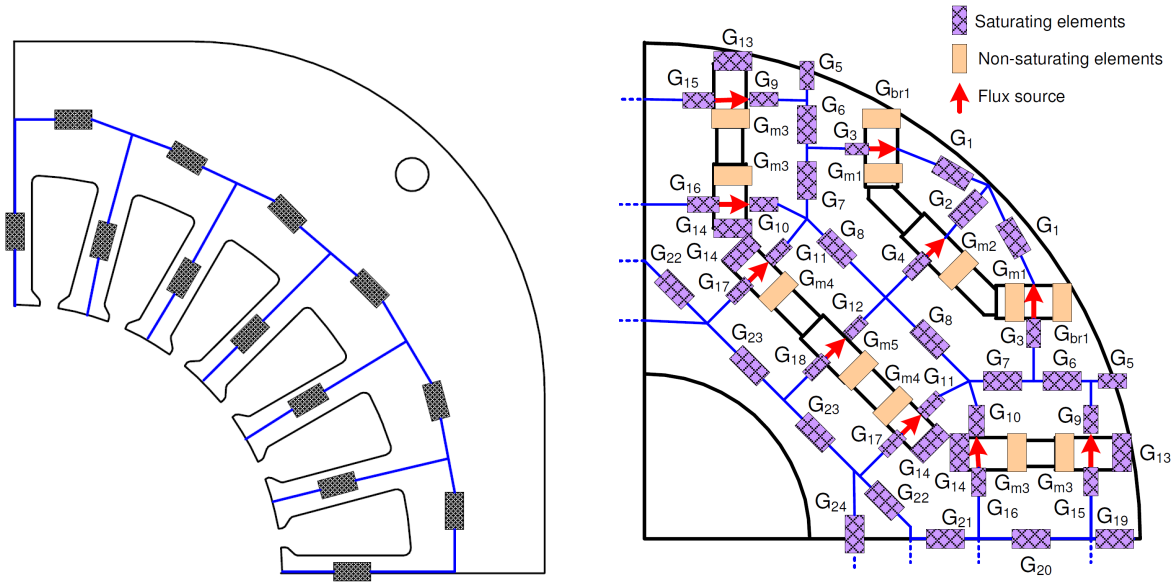

(a) A typical magnetic equivalent circuit for a stator.

(b) A typical magnetic equivalent circuit for a rotor with magnets.

Figure 2.26: Magnetic equivalent circuit for a permanent magnet electrical machine [25].

The building blocks for the MEC in an electrical machine include the MMF, the reluctance elements in the stator back iron, the stator teeth, the rotor structure, the slots, and the airgap. Figure 2.27 shows the main building blocks for a simple electrical machine topology. Here, each region of the machine, except for the stator back iron, is represented by the networks of four reluctance elements, the circumferential component R_θ and the radial component R_r. The concept of representing a region in the machine as a network of four reluctance elements have been discussed in induction machine [26], as well as in permanent magnet machine [27]. The use of four elements instead of a single element in traditional MEC model helps improve the accuracy of the MEC. The stator back iron is represented by a single reluctance element R_{sy} for simplification purpose. The airgap here is represented as a single layer, with multiple nodes (two nodes were shown in Figure 2.27). Each node is also represented by the network of four reluctance elements. Each node in the airgap is

connected to the corresponding node in the rotor region.

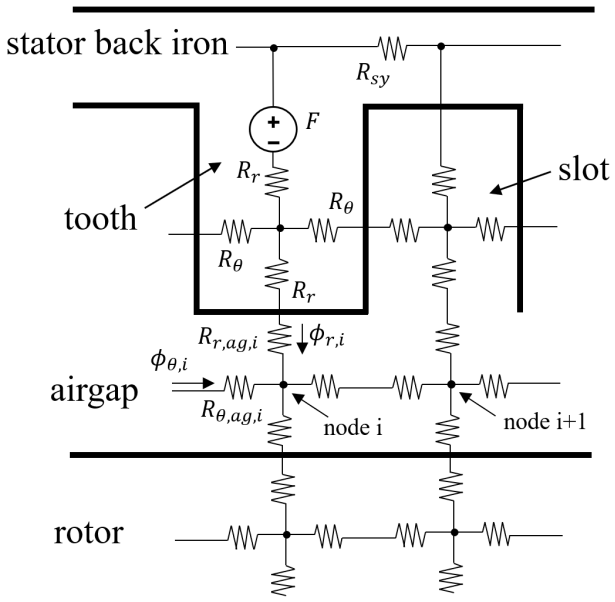

Figure 2.27: MEC representation of the main flux from the stator to the rotor. Only a section of the electrical machine is shown here. This MEC model can be used to represent the main flux of the entire machine

As with traditional MEC techniques, the MEC models in [26, 27] assume that the stator core and the rotor core are homogeneous with the same magnetic properties. The accuracy of estimating the airgap flux density in the MEC in Figure 2.27 can be improved by having multiple layers of reluctance elements in the airgap region as well as more nodes in the circumferential direction.

Chapter 3

Multi-permeability Modelling

Non-uniform magnetic behavior within the iron cores indicates the possibility of improving the machine performance by deploying magnetic materials with non-homogeneous, multi-permeability property. The potential use of multi-permeability iron cores requires a modelling technique that can aid the design process.

This chapter provides a modelling technique for a non-homogeneous, multi-permeability iron core in an electrical machine. The technique is developed based on the concept of MEC and verified on a simple SynRM. Using the multi-permeability modelling technique in conjunction with an optimization technique, the manipulation of the harmonic contents of the airgap flux density of a simple SynRM can be achieved. The chapter ends with a numerical demonstration on the manipulation of the airgap flux density.

3.1 Multi-permeability modelling

Traditional MEC models assume that the iron cores are homogeneous with the same magnetic properties. Occasionally, reluctance elements within the iron cores are omitted, assuming infinite relative permeability. To exploit the capabilities of additive manufacturing technologies to develop iron cores with multi-permeability, the typical MEC model is modified to include the reluctance network in the iron core. There are a number of present day challenges for additive manufacturing technologies to overcome with multi-material AM due

to the dissimilarities in the materials properties. However, at the current rapid pace of technological breakthroughs in AM, these challenges may soon be a thing of the past. The multi-permeability model is developed assuming:

1. The AM technology can deposit soft magnetic material with a specific $\mu_{r,max}$ at the desired sub-regions/ cells in the iron core
2. The deposited materials have the same specific loss density curve
3. There are no gaps or pores between the adjacent cells
4. The deposited materials have linear magnetization curves

There are two steps required for development of the multi-permeability model: discretization and stator MMF estimation.

3.1.1 Discretization

Discretization is the process of dividing the electrical machine geometry into discrete cells sub-regions/ cells. With discretization, non-homogeneous multi-permeability iron cores can be represented by assigning different relative permeability for each cell. A simple illustration of non-homogeneous magnetic core with varying relative permeability is shown in Figure 3.1.

Each cell, either in the slots, teeth, airgap, and the rotor core, can be then represented by the four-element reluctance from a single node as shown in Figure 3.2. Here, $R_{r,i}$ represents the radial reluctance component while $R_{\theta,i}$ represents the circumferential reluctance component of cell i^{th}. The reluctance elements are calculated using (3.1), where w_i is the

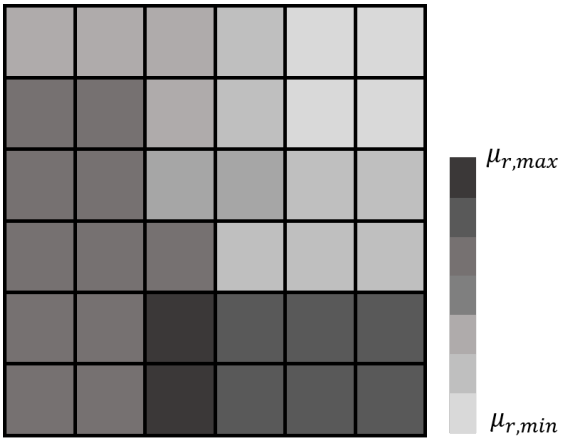

Figure 3.1: Illustration of non-homogeneous magnetic core with varying relative permeability.

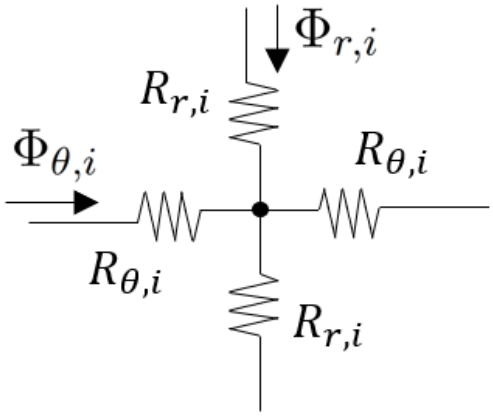

Figure 3.2: Reluctance elements representative for each cell.

width of cell i^{th}, l_i is the length of cell i^{th}, and L is the machine stack length.

$$R_{r,i} = \frac{0.5 l_i}{\mu_{r,i} \cdot \mu_0 \cdot w_i \cdot L}, \qquad R_{\theta,i} = \frac{0.5 w_i}{\mu_{r,i} \cdot \mu_0 \cdot l_i \cdot L} \tag{3.1}$$

The concept of representing a region in the machine as a network of four reluctance elements have been used for both induction and permanent magnet machines [26, 27]. The use of four elements instead of a single element in traditional MEC model helps improve the accuracy of the MEC in estimating both radial and circumferential airgap flux density. The multi-permeability structure in Figure 3.1 has a single level relative permeability variation since

all four reluctance elements within a single cell have the same relative permeability $\mu_{r,i}$. Bi-level relative permeability variations have different values for radial and circumferential reluctance elements in each cell. The analysis in this work only accounts for single level variation.

Increasing the number of cells in the machine geometry helps improve the estimation of the airgap flux density in the machine, at the expense of higher calculation effort. The discretization process for the electrical machine starts at the airgap region. By uniformly dividing the airgap region in the circumferential direction into $2n$ cells, up to the n^{th} spatial harmonic order of the airgap flux density can be identified. Additionally, a mechanical displacement of the rotor $\Delta\theta_r$ by π/n can be modelled. In the radial direction, the airgap region can be represented with k_{ag} layers. Thus, for a complete discretized airgap region in the electrical machine, there are a total of $2n \cdot k_{ag}$ cells. The rotor and stator cores are also divided into $2n$ cells in the circumferential direction. This ensures that each cell in the airgap is connected to corresponding cells in the stator and rotor. The stator teeth and rotor can be further discretized into layers radially, k_t and k_r, respectively. Figure 3.3 illustrates the discretized airgap region and the corresponding discretized rotor region. A

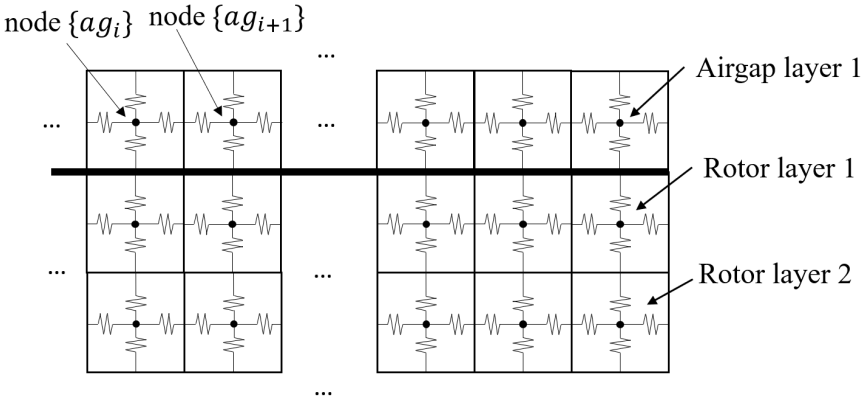

Figure 3.3: Illustration of the interconnections of reluctance elements in the rotor and the airgap. The reluctance network is shifted and reconnected to the reluctance network from the stator as the rotor rotate.

relative permeability of 1 is used for the cells that represent a void or non-magnetic material.

The airgap flux density can then be calculated by solving the combined reluctance network for the machine. The radial and circumferential airgap flux density at node ag_i from cell i can be estimated via (3.2). Here, $A_{r,ag,i}$ and $A_{\theta,ag,i}$ are the area of cell i in the airgap in the radial and circumferential directions, respectively. While $\Phi_{r,i}$ and $\Phi_{\theta,i}$ are the values of flux in the radial branch and the circumferential branch, respectively.

$$B_{r,i} = \frac{\Phi_{r,i}}{A_{r,ag,i}}, \qquad B_{\theta,i} = \frac{\Phi_{\theta,i}}{A_{\theta,ag,i}} \tag{3.2}$$

3.1.2 Stator MMF estimation

The Fourier series representation of the stator MMF is used to provide the values F_x, shown in Figure 3.4. At time instant t_1, the values of F_x are given by (3.3), where θ_x is the

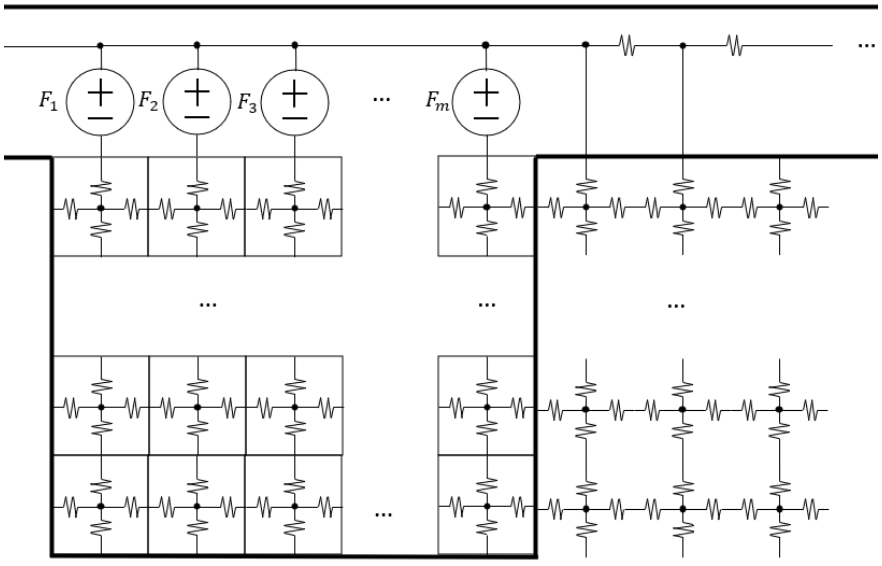

Figure 3.4: Illustration of the interconnections of reluctance elements in the stator and the slot regions.

angular position in the stator reference frame.

$$F_x = \begin{cases} F_(t_1, \theta_x), & \theta_x \text{ is above a tooth} \\ 0, & \theta_x \text{ is above a slot} \\ & \text{where } x = 1, \cdots, 2n \end{cases} \tag{3.3}$$

Kirchoff's laws are used to calculate the flux in all of the branches of the combined reluctance network. Transient estimation of the airgap flux density can be found by repeating the static estimation at different time instants, considering the AC currents in the windings. As the rotor rotates, the reluctance network in Figure 3.3 can be shifted to represent the change in rotor position.

3.1.3 Finite element verification

A simple, 6-slot, 2-pole SynRM, shown in Figure 3.5, was used to verify the performance of the multi-permeability modelling technique. The stator poles within the machine are subjected to the multi-permeability distribution pattern, as shown by the hatched region in Figure 3.6. The machine parameters are given in Table 3.1.

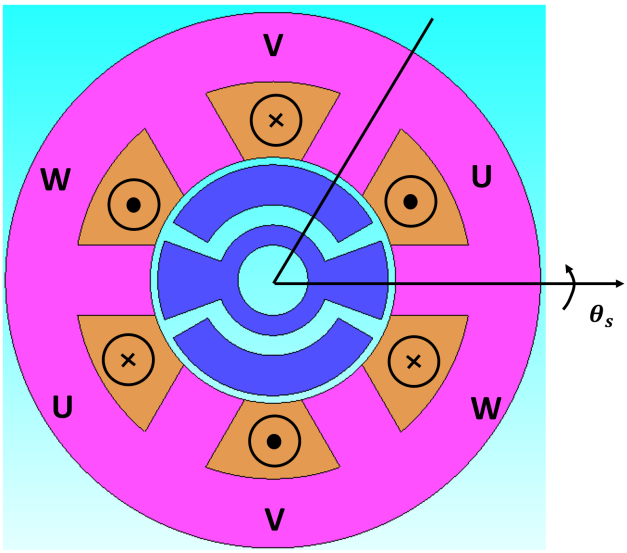

Figure 3.5: A finite element model of the simple 6-slot/2-pole synchronous reluctance machine.

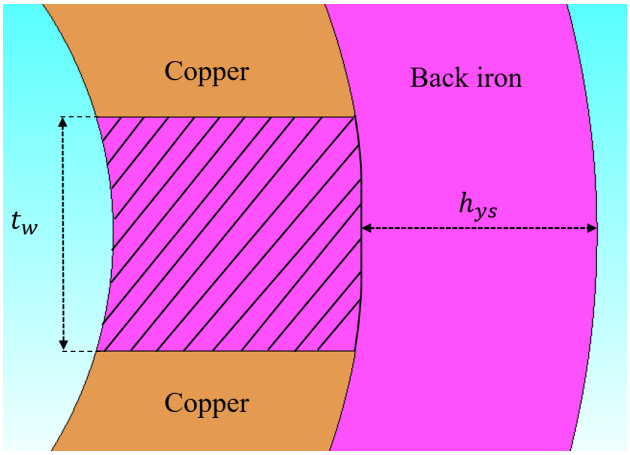

Figure 3.6: The stator poles in the SynRM are subjected to non-homogeneous, multi-permeability distribution.

The MEC model was discretized where $n = 36$ and $k_{ag} = 1$ such that the airgap flux density could be calculated at 5° increments. Both the stator and rotor included 8 layers in the radial direction, with $k_t = k_r = 8$. The cells in the rotor corresponding to the flux barriers are assigned a relative permeability of 1. The stator back iron includes 12 sub-regions circumferentially. The discretized SynRM is shown in Figure 3.7.

Accuracy of the MEC model of the SynRM was evaluated with homogeneous distribution

Table 3.1: Parameters of the simple synchronous reluctance machine.

Parameters	Values	Parameters	Values
Slot/ pole	6/ 2	Stack length	37.5 mm
Turns per phase	100	Stator OD	53.4 mm
Excitation current	5 A	Rotor OD	23 mm
Rated speed	3600 rpm	Airgap length	0.75 mm
Back iron thickness h_{ys}	6.9 mm	Tooth width t_w	7 mm
Barrier thickness t_b	2 mm	Barrier span angle	135 deg

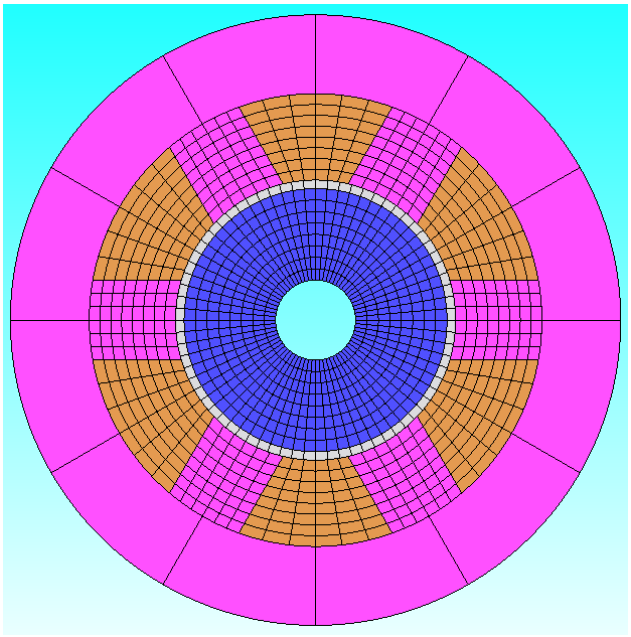

Figure 3.7: Illustration of the discretized synchronous reluctance machine modeled using MEC.

of the permeability. The radial and circumferential component of the air gap flux density was compared to the FEA model. Here the permeability is set to 3000. As shown in Figure 3.8, the MEC model estimation of the airgap flux density in the radial and the circumferential direction closely approximates FEA results. It is worth noting that the multi-permeability

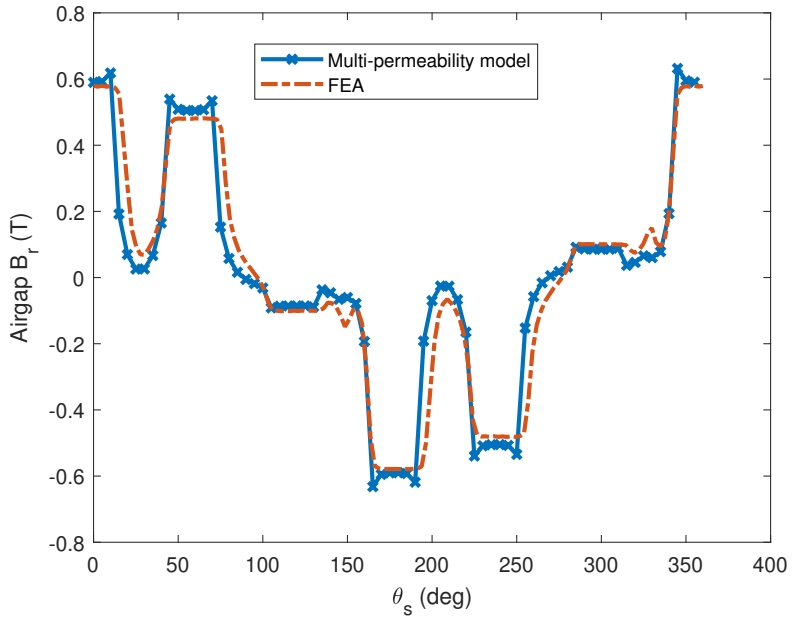

(a) Radial B_{ag}.

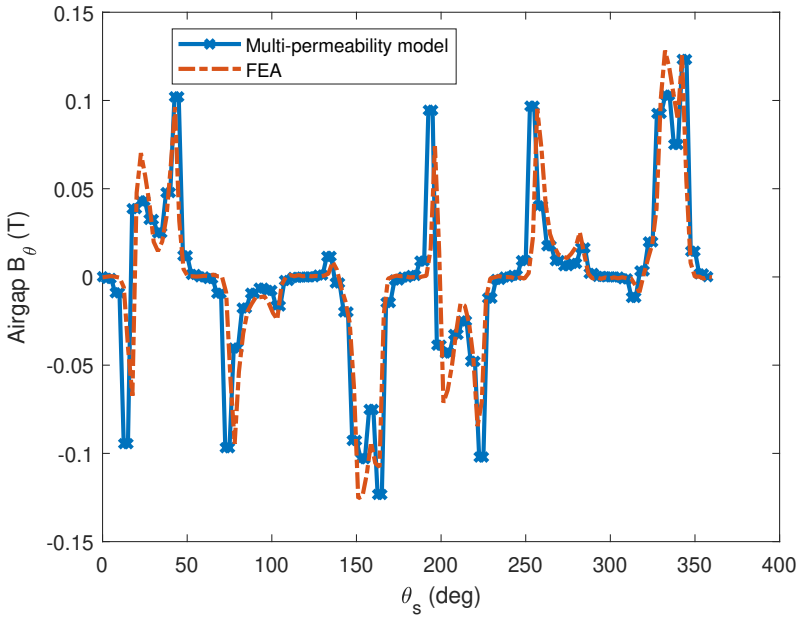

(b) Circumferential B_{ag}.

Figure 3.8: Air gap flux density comparison between magnetic equivalent reluctance network and FEA, for homogeneous stator. Here, $I_u = -0.26\hat{I}, I_v = -0.71\hat{I}, I_w = 0.97\hat{I}$.

MEC model can estimate the static airgap flux density in both radial and circumferential direction more than 5 times faster in comparison to FEA.

Accuracy of the MEC model of the SynRM was also evaluated with random distribution of the permeability in the teeth, as shown in Figure 3.9. Here, the relative permeability of

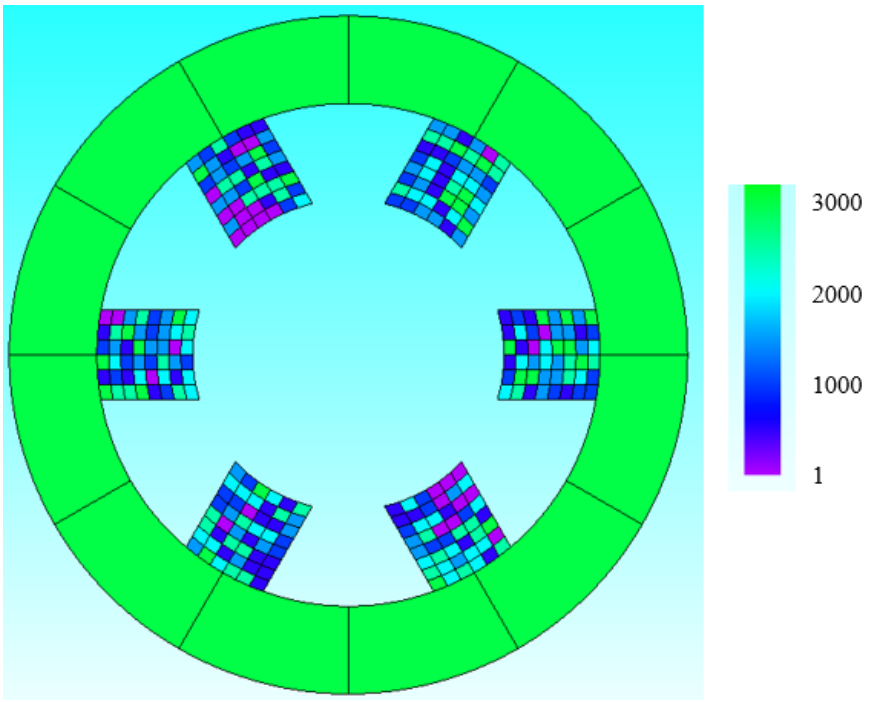

Figure 3.9: FEA model of stator with randomly distributed relative permeability in the teeth.

each cell in the tooth is randomly selected within the range $[\mu_{r,MIN}, \mu_{r,MAX}] = [1, 3000]$. As shown in Figure 3.10, the multi-permeability MEC estimates the airgap flux density fairly accurately when compared to FEA results.

3.2 Airgap flux density manipulation

In this section, the radial airgap flux density of the simple SynRM is manipulated using the stator core with a non-homogeneous, multi-permeability distribution pattern $\boldsymbol{\mu}$. The patterns of the multi-permeability stator core are generated by coupling an evolutionary multi-objective optimization algorithm with the multi-permeability modelling technique,

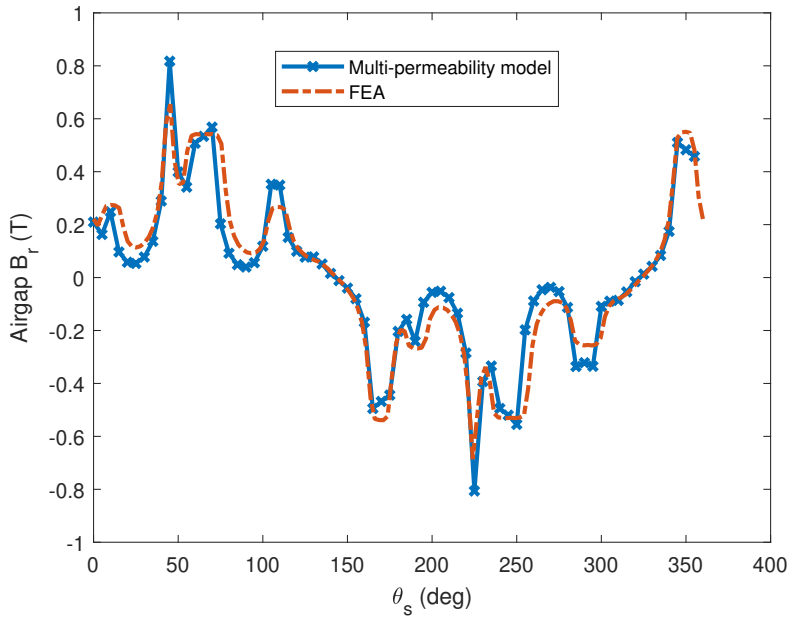

(a) Radial B_{ag}.

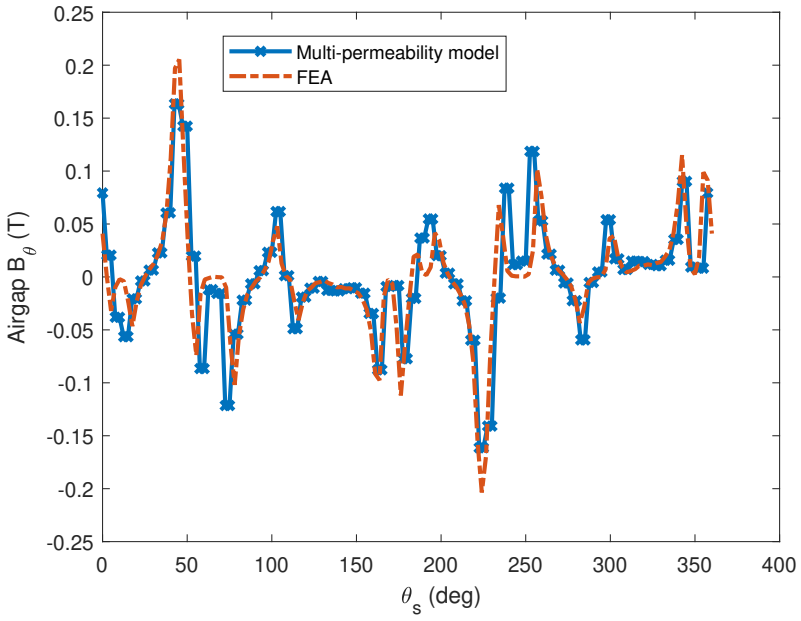

(b) Circumferential B_{ag}.

Figure 3.10: Air gap flux density comparison between magnetic equivalent reluctance network and FEA, for a randomly distributed non-homogeneous, multi-permeability stator. Here, $I_u = -0.65\hat{I}, I_v = -0.33\hat{I}, I_w = 0.98\hat{I}$.

given defined objectives.

The objective space is defined such that certain harmonics in the airgap flux density at

time t_0 are maximized or minimized. The selection of the harmonic orders is related to the torque characteristics. Here, $B_{1(ag,r)}$ and $B_{5(ag,r)}$ are the spatial fundamental and fifth order harmonic of the radial airgap flux density, respectively. The spatial fundamental harmonic order is related to the average torque in the machine while the fifth order is related to the slot effect of the machine. The multi-objective optimization problem is represented by (3.4). A total of seven permeability options was used, with the range of the relative permeability values is between 1 and 3000, step size of 500. The distribution pattern $\boldsymbol{\mu}$ is repeated for each stator pole. The evaluation of the airgap flux density harmonics is implemented via the multi-permeability modelling technique in lieu of FEA.

$$\begin{aligned} &\text{Maximize: } B_{1(ag,r)}(\boldsymbol{\mu}) \\ &\text{Minimize: } B_{5(ag,r)}(\boldsymbol{\mu}) \\ &\text{Subject to: } \mu_{r,min} \leq \mu_{r,i} \leq \mu_{r,max}, \quad i = 1, \cdots, mk_t \end{aligned} \tag{3.4}$$

The Pareto-front for the optimization problem, as shown in Figure 3.11, shows the trade-off between the 5^{th} harmonic order of the radial airgap flux density with respect to the fundamental harmonic order. The solutions along the Pareto front show that the 5^{th} order amplitude can be reduced up to 33% at the trade-off of up to 21% for the fundamental amplitude, as shown in Figure 3.12. Seven solutions, A to G, are selected from the front as representatives; they are selected such that they represent the amplitude of the fundamental order from 0.27 T to 0.33 T. The permeability distribution patterns $\boldsymbol{\mu}$ for solutions A to G are illustrated in Figures 3.13 to 3.19, respectively.

The comparison with the homogeneous stator shows that for each solution from A to

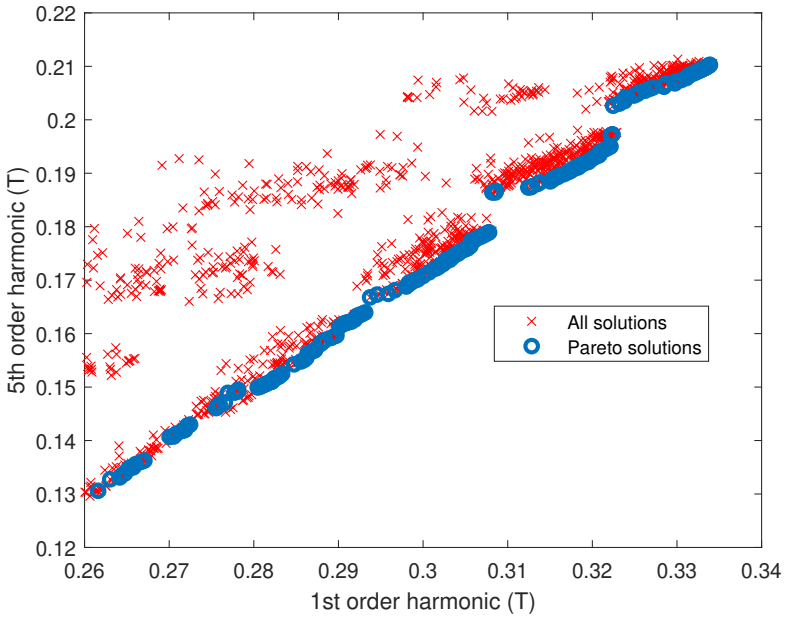

Figure 3.11: Objective space from optimization problem (3.4).

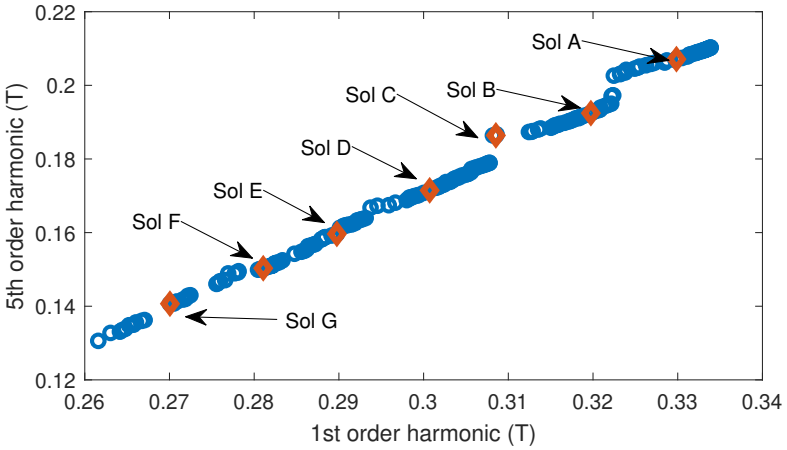

Figure 3.12: Pareto front of $\boldsymbol{\mu}$ distributions from optimization problem (3.4).

G, the spatial fundamental and the fifth order harmonics are manipulated, as shown in Figure 3.20. As the seventh, eleventh, and thirteenth harmonic orders are not included in the optimization problem definition, they vary differently in comparison to the homogeneous stator harmonic orders. This suggests that these harmonic orders can be further manipulated if they are included in the process of generating the $\boldsymbol{\mu}$ patterns.

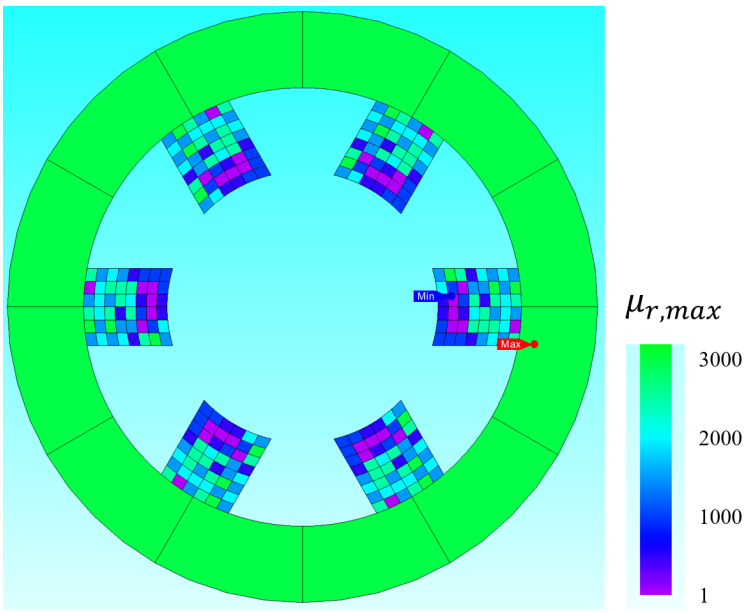

Figure 3.13: Non-homogeneous, multi-permeability distribution for the stator core - Sol A.

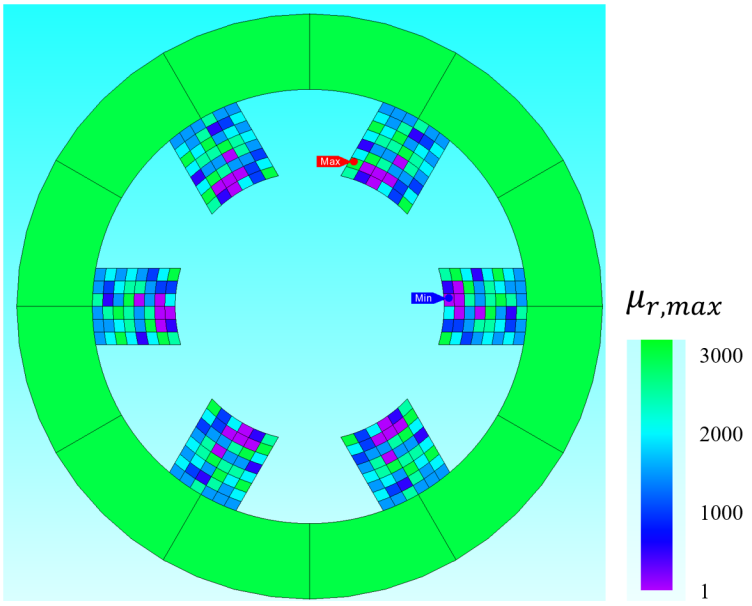

Figure 3.14: Non-homogeneous, multi-permeability distribution for the stator core - Sol B.

3.3 Numerical demonstration

FEA is used to demonstrate the change in the waveform of the radial airgap flux density due to different $\boldsymbol{\mu}$ patterns. In comparison to the homogeneous stator, the spatial fifth order harmonic of stator with $\boldsymbol{\mu}$ pattern (Sol C) reduces by 10.6% at a trade off of 6.4% in spatial

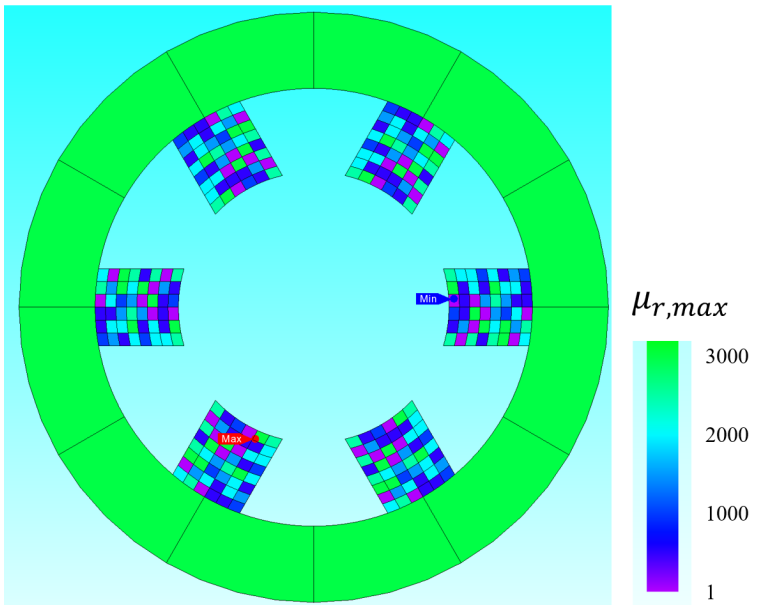

Figure 3.15: Non-homogeneous, multi-permeability distribution for the stator core - Sol C.

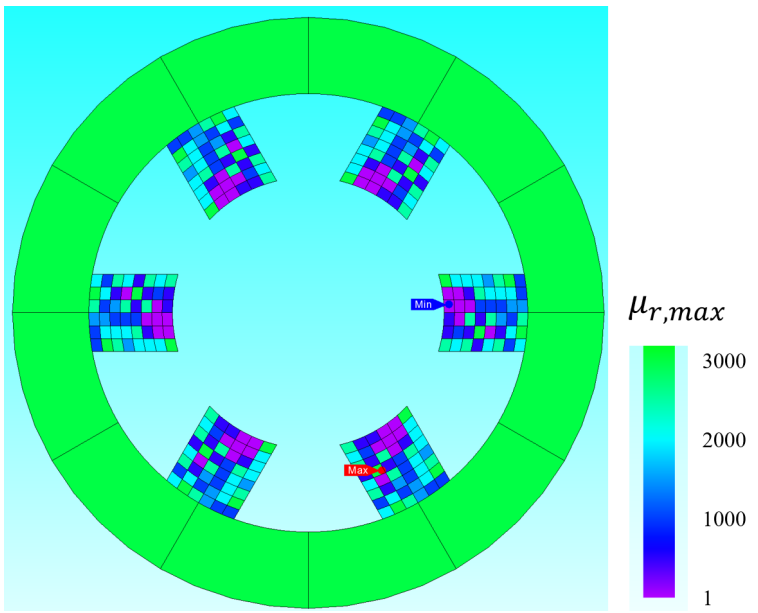

Figure 3.16: Non-homogeneous, multi-permeability distribution for the stator core - Sol D.

fundamental order, as shown in Figure 3.21a. Correspondingly, the peak to peak torque ripple (in amplitude) for the stator with $\boldsymbol{\mu}$ pattern (Sol C) reduces by 8.8% at a trade off of 8.6% in torque average, as shown in Figure 3.21b. Torque ripple as a percentage remains relatively unchanged.

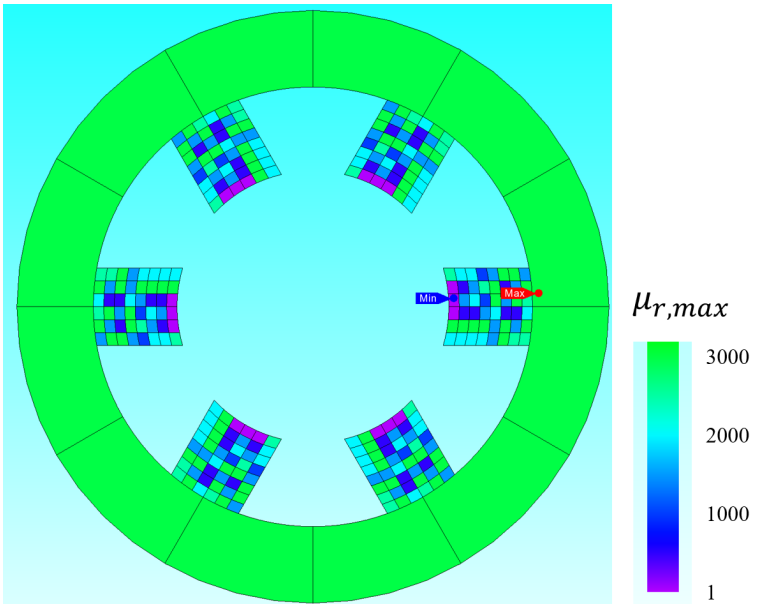

Figure 3.17: Non-homogeneous, multi-permeability distribution for the stator core - Sol E.

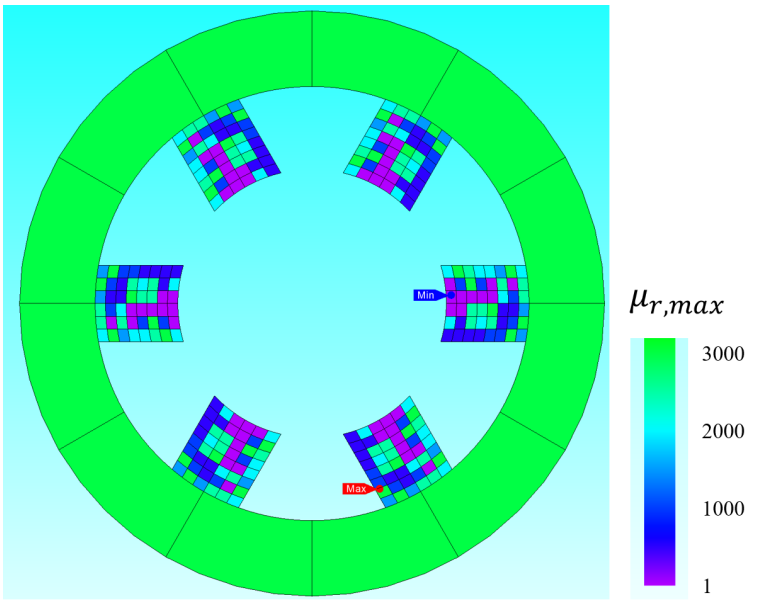

Figure 3.18: Non-homogeneous, multi-permeability distribution for the stator core - Sol F.

FEA is used again to analyze stator with $\boldsymbol{\mu}$ pattern (Sol E) distribution. In comparison to the homogeneous stator, the spatial fifth order harmonic of stator with $\boldsymbol{\mu}$ pattern (Sol E) reduces by 31.7% at a trade off of 16% in spatial fundamental order, as shown in Figure 3.22a. Correspondingly, the peak to peak torque ripple (in amplitude) for the stator with $\boldsymbol{\mu}$ pattern

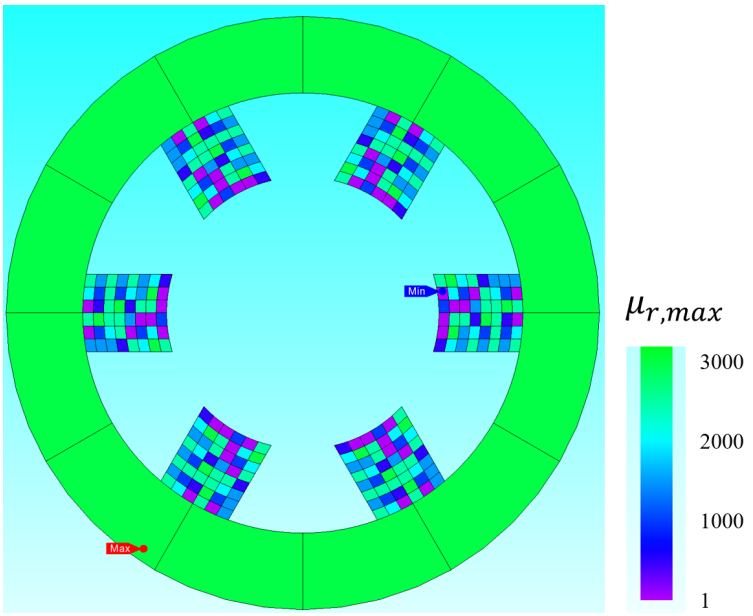

Figure 3.19: Non-homogeneous, multi-permeability distribution for the stator core - Sol G.

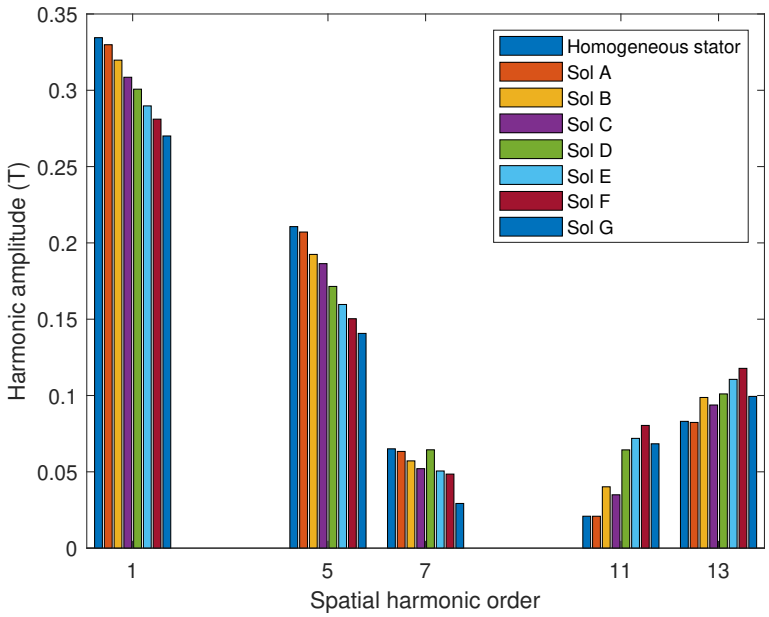

Figure 3.20: Changes of amplitudes of radial airgap flux density harmonic orders of selected solutions on the Pareto front from optimization problem (3.4). The multi-permeability modelling is used to evaluate the harmonics amplitudes.

(Sol E) reduces by 20% at a trade off of 21.9% in torque average, as shown in Figure 3.22b.

Thus, the torque ripple as a percentage slightly increases by 2%. Table 3.2 summarizes the

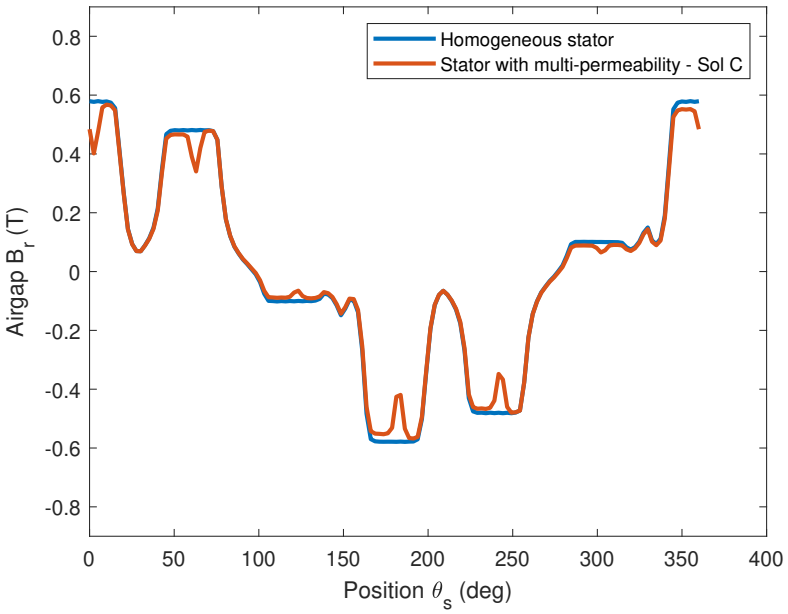

(a) Radial B_{ag}. Here, $I_u = -0.26\hat{I}, I_v = -0.71\hat{I}, I_w = 0.97\hat{I}$.

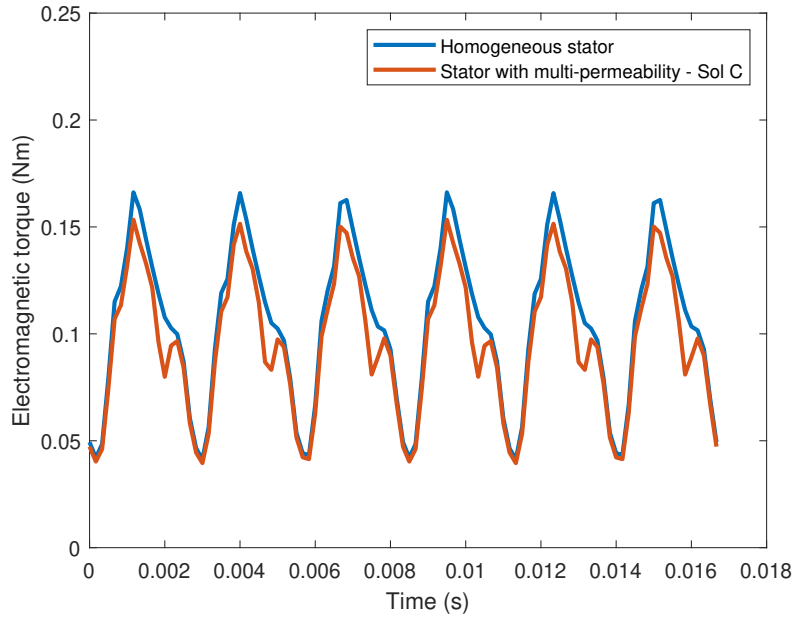

(b) Electromagnetic torque.

Figure 3.21: Finite element comparison between homogeneous stator and stator with multi-permeability $\boldsymbol{\mu}$ (Sol C).

torque performance metrics between homogeneous stator and non-homogeneous stator, for solutions A to G.

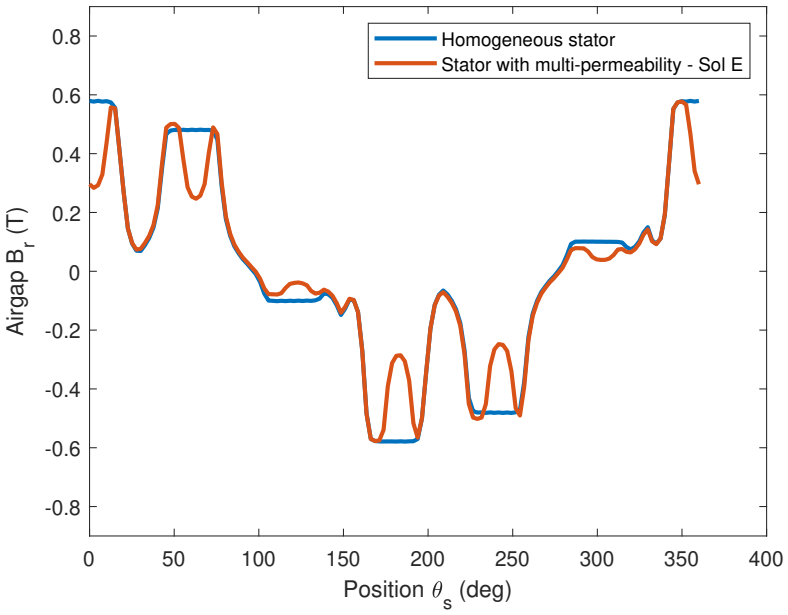

(a) Radial B_{ag}. Here, $I_u = -0.26\hat{I}, I_v = -0.71\hat{I}, I_w = 0.97\hat{I}$.

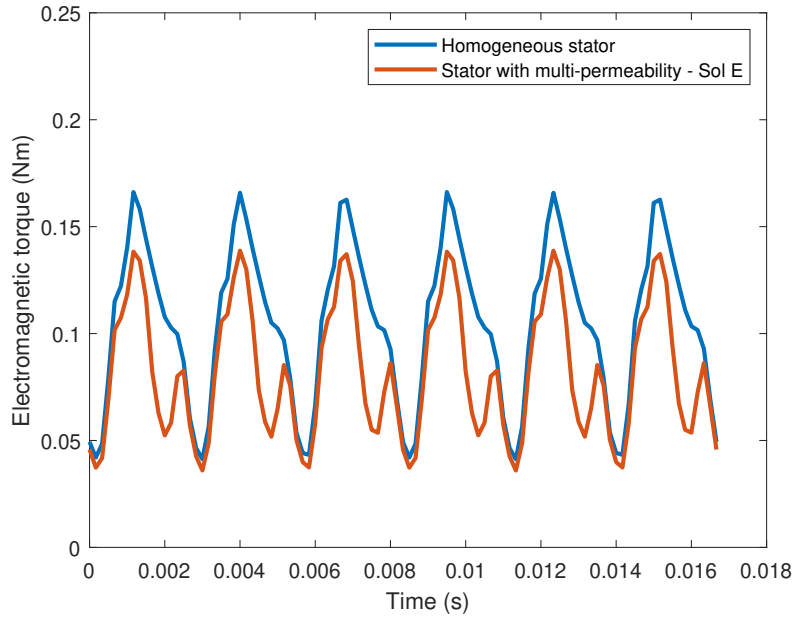

(b) Electromagnetic torque.

Figure 3.22: Finite element comparison between homogeneous stator and stator with multi-permeability $\boldsymbol{\mu}$ (Sol E).

Table 3.2: Comparison on torque metrics between homogeneous stator and stator with non-homogeneous, multi-permeability distributions.

Torque metrics	Homogeneous	Sol A	Sol B	Sol C	Sol D	Sol E	Sol F	Sol G
Average (mNm)	105	103	100	96	90	82	79	76
Ripple (mNm)	125	121	120	114	113	100	100	98
Ripple (%)	119	117.5	120	119	125.6	121	126.6	128.9

Chapter 4

Soft Magnetic Materials

In electrical machines, soft magnetic materials are used to form the stator and rotor cores. They are responsible for the guidance and improvement of the main flux created by the continuously moving magnetic field. These materials are characterized with low intrinsic coercivity, typically below 1000 A/m, and can be easily magnetized or demagnetized [2]. High relative permeability, high magnetic saturation, low hysteresis and eddy current loss are desirable characteristics in soft magnetic materials for electrical machines. These magnetic properties are highly related to the airgap flux density and its harmonic contents, which in turn are related to the torque/ force production and the efficiency of the electrical machine. Leveraging the magnetic properties of the soft magnetic material as well as novel design of the magnetic cores can theoretically improve the airgap flux density, and subsequently the performance of the electrical machine.

This chapter provides the overview of soft magnetic materials. Information regarding the magnetization curve and specific loss density are discussed, following by the standard magnetic characterization methods. Also included in the chapter is the review on current status of additively manufactured soft magnetic materials.

4.1 Characteristics of soft magnetic materials

Characteristics of soft magnetic material are described via the $B-H$ curve as well as the iron loss curve of the material. These characteristics are heavily dependent on the magnetic texture of the material.

4.1.1 Magnetization curve and hysteresis loop

Soft magnetic materials express no net magnetization under no external magnetic field. This is due to the materials being divided into multiple separate magnetic domains called Weiss domains. Within each Weiss domain, all the magnetic moments point in the same direction, resulting in each magnetic domain having a uniform magnetization direction. The magnetization direction of each Weiss domain differs from each other and varies throughout the material as shown in Figure 4.1. The transition boundaries or regions between the Weiss domains are called Bloch walls. At rest position or under no external excitation, within the Bloch wall between two Weiss domains, the direction of the magnetic moments gradually changes from one domain to the next as shown in Figure 4.2.

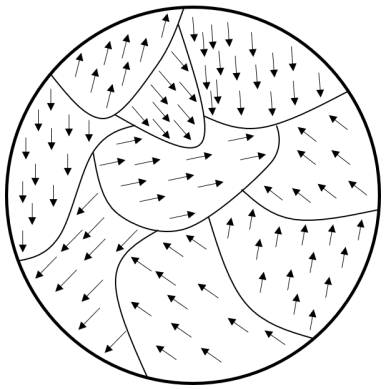

Figure 4.1: Description of Weiss domains of soft magnetic materials under no external excitation.

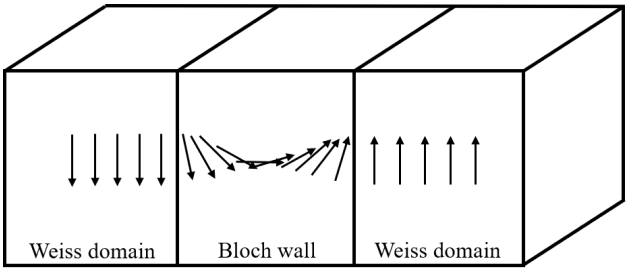

Figure 4.2: Description of the Bloch wall and the transition of magnetic moments between two adjacent Weiss domains.

When the soft magnetic materials are subjected to a weak external magnetic field strength, H, the Weiss domains that are already in the direction of the external field strength will increase and align with the field, while the domains in the opposite direction or other directions will try to align with the direction of the external field, Figure 4.3. Additionally, the Bloch walls slightly move away from the rest position. As the external field strength increases, the Weiss domains further increases and aligns with the external field strength. If the external field strength is high enough, the Bloch walls displace and do not return to the original position. This is called Barkhausen jump.

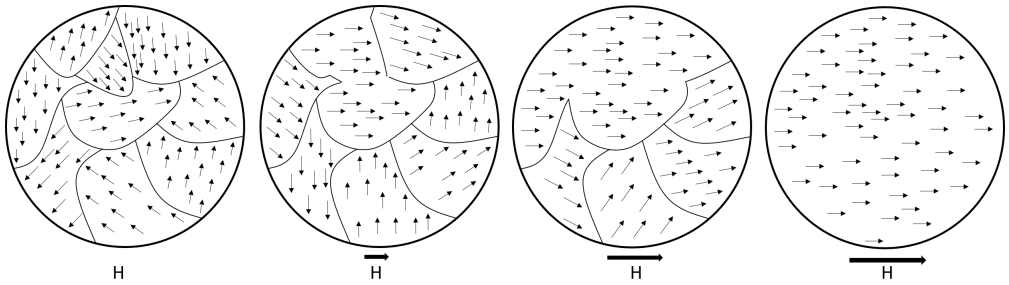

Figure 4.3: Description of the changes in the magnetization direction of the Weiss domains. The external magnetic field strength H increases, shown from left to right.

In general, the magnetization curve, which represents the $B - H$ relationship of the soft magnetic materials, can be described with three distinctive stages, Figure 4.4. In the first stage, when the external field strength is low, the Bloch walls displace from the rest

position, but this process is reversible. In the second stage, when the external field strength increases, the Barkhausen jumps occur, the Bloch walls displace and cannot reverse to the original position. In the final stage, all the Weiss domains are aligned with the direction of the external magnetic field strength. The materials are said to be saturated. The $B - H$ relationship does not saturate at a single value in the third stage but still continues to increase as the external field strength increases. The rate of this increase is defined by the permeability in vacuum μ_0 and described in (4.1). Here, M is the magnetization of the soft magnetic materials created by the magnetic field strength H, while μ_r is the relative permeability of the soft magnetic materials. As the material approaches saturation, the magnetic polarization, J, reaches the saturation polarization value, J_s.

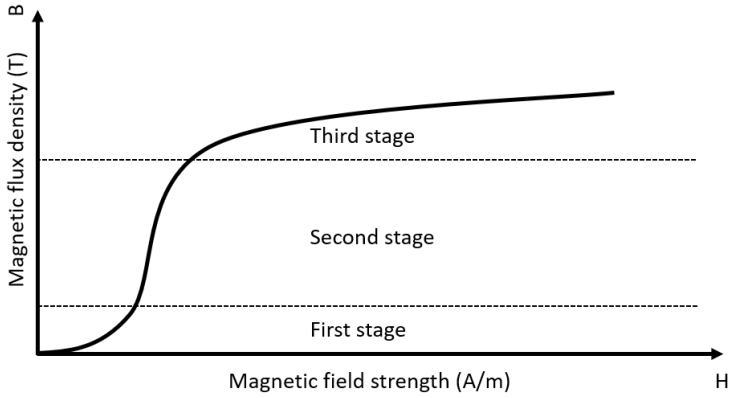

Figure 4.4: Description of magnetization curve of a general soft magnetic material.

$$B = J + \mu_0 H = \mu_0(H + M) = \mu_0 \mu_r H \tag{4.1}$$

Characteristics of a fully demagnetized soft magnetic sample under external magnetization is shown in Figure 4.5. Initially, the magnetization starts at the origin. As the external field increases in strength, the Bloch walls start to irreversibly displace and the Weiss domains start to align with the direction of the external field. The resulted magnetization

curve, shown as solid line in Figure 4.5, is called the initial magnetization curve. When the external magnetic field strength reduces and approaches zero, the magnetic moments within the Weiss domains turn toward the axes of easy magnetization. When the applied external field is zero, the soft magnetic sample has a non-zero net magnetization. The sample is then said to have a remanent flux density B_r. By further reducing the external magnetic field to $-H_c$, the remanence flux within the sample is returned to zero. H_c, usually called the coercivity or the coercive force, is the force required to bring the residual flux of the soft magnetic materials to zero. When the applied field is further reduced, the magnetization of the sample approaches negative saturation. By increasing the applied field again to zero, the magnetization does not approach the origin but instead crosses the vertical axis at a point with that provides the same level of remanent flux. The magnetization of the sample reaches the positive saturation again as the applied field is strengthened, creating the hysteresis loop.

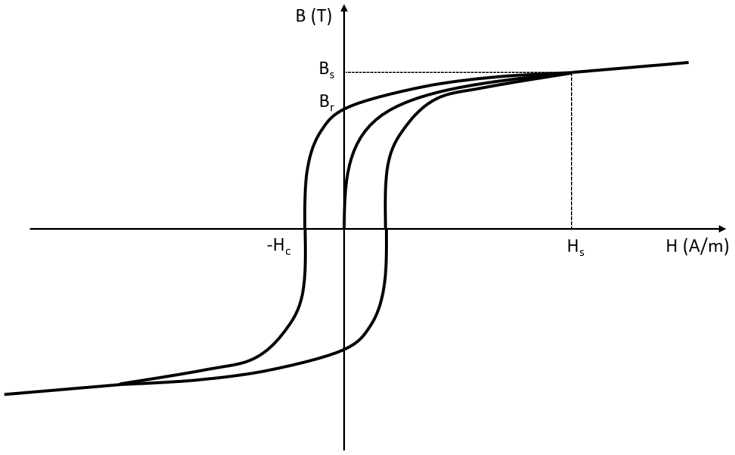

Figure 4.5: Hysteresis loop and important magnetic characteristics of a general soft magnetic material.

4.1.2 Specific loss density

The discussion of iron loss here is based on common iron loss knowledge seen in iron silicon lamination steels. Although this discussion may not be fully transferred to AM iron silicon, it can help provide meaningful insights during iron loss analysis of AM parts.

The iron loss in soft magnetic materials is due to the difference in the phase shift between the magnetization field H and the magnetic flux density B, and is calculated over one electrical cycle T, [28]. There are two main components contributing to the iron loss, hysteresis loss, p_h, and eddy loss, p_e. The hysteresis loss is directly related to the intrinsic coercivity H_c of the materials and is estimated as in (4.2), where γ is the density of the materials.

$$p_h = \frac{4 \cdot f \cdot H_c \cdot \hat{B}}{\gamma} \tag{4.2}$$

For a pure sinusoidal magnetic flux density waveform, the eddy loss can be approximated as in (4.3). Here, d represents the thickness of the lamination sheet and ρ is the electrical resistivity of the materials.

$$p_e = \frac{\pi^2 \cdot f^2 \cdot \hat{B}^2 \cdot d^2}{6 \cdot \gamma \cdot \rho} \tag{4.3}$$

From (4.2) and (4.3), it is possible to separate the hysteresis loss from eddy loss by extrapolating the iron loss per cycle, p_{fe}/f, when the excitation frequency approaches 0.

For medium excitation frequency, from 20 to 100 kHz, the specific loss can no longer be estimated as the sum of the relationships in (4.2) and (4.3). It is instead estimated using the Steinmetz equation as shown in (4.4). The values of x, y, z, f_0, $\hat{B}_0$, and F_0 are usually found experimentally.

It is important to note that the eddy current loss calculated as in (4.3) assumes that the permeability is uniform and homogeneous within the materials, [28]. In cases where the change of magnetization dB/dt is much higher in a local area where the moving domain wall is located, then there exists an additional losses. This anomalous eddy loss contributes to the eddy loss, and is usually referred to as excess loss, p_{excess}. The specific loss density is now the sum of the hysteresis loss, the classical eddy loss, and the excess loss as shown in (4.5).

$$p_{fe} = p_0 \cdot \left(\frac{F}{F_0}\right)^x \cdot \left(\frac{f}{f_0}\right)^y \cdot \left(\frac{\hat{B}}{\hat{B}_0}\right)^z \tag{4.4}$$

$$p_{fe} = p_h + p_{e,classical} + p_{excess} \tag{4.5}$$

As shown in [29], the excess eddy loss of the materials can be estimated as in (4.6). Here c represents the scaling factor of the specific domain wall energy, [29]. From (4.5), the hysteresis dominates total iron loss at low excitation frequency. As the excitation frequency increases, the classical eddy loss and the excess loss become the dominant factors.

$$p_{excess} = \frac{c \cdot (\hat{B} \cdot f)^{1.5}}{\gamma} \tag{4.6}$$

4.2 Current status on printed soft magnetic materials

Additive manufacturing (AM), also known as 3D printing, provides many advantages over traditional manufacturing methods, including its capability of fabricating complex shapes with minimal tooling effort. Recent technology advancements in AM also allow for the tuning

of magnetic properties of fabricated parts by varying printing parameters. The feasibility of 3D printing soft magnetic materials with desired properties can open up opportunities for new electrical machine design concepts.

In electrical machines, the three commonly seen soft magnetic materials are iron-cobalt (FeCo), iron-nickel (FeNi), and iron-silicon (FeSi) alloys. A large part of research in AM of soft magnetic materials focuses on laying foundations for printing these iron alloys. These foundations include magnetic, mechanical, and microstructural characterization of the printed iron alloys, as well as their relationships to the printing parameters.

4.2.1 Iron-Cobalt (FeCo)

One of the most attractive properties of FeCo is that it has the highest magnetic saturation compared to other soft magnetic iron alloys, with J_s value settling around 2.4 T. However, the conventional production of FeCo iron cores is subjected to the high material cost of cobalt, the low workability of the iron-cobalt alloy, and the additional requirement of heat treatment of the stacked iron core. This limits the use of FeCo iron cores, especially for cost-sensitive applications. As a result, reducing the challenges associated with the production of FeCo iron cores via additive manufacturing is of high interest among AM research groups. Efforts in printing FeCo iron cores have been shown via the applications of 3D screen printing and laser engineered net shaping technologies (LENS). It is reported in [18] that FeCo fabricated with 3D screen printing achieves magnetic induction comparable with commercial FeCo alloy with 15–20% cobalt content. Higher magnetic induction and saturation can be achieved if the porosity level in 3D screen-printed FeCo cores is reduced. Further comparison between screen-printed FeCo and commercial laminated FeCo shows that printed cores have higher iron loss, making its magnetic performance less appealing.

FeCo parts printed with LENS technology, [30], show good potential, with achieved magnetic saturation settling around 2.2 to 2.3 T, within 10% in comparison to commercial FeCo alloyed with vanadium. When as-built FeCo core is heat-treated, its maximum relative permeability increases approximately three-fold, while its intrinsic coercivity drops by two thirds. Here, the annealing process leads to the development of a bimodal grain size characteristic, where coarse grains with average grain size around 200 to 600 µm are surrounded by finer grains (around 2 µm in size). By tuning the printing parameters or mixing additives into the iron alloy starting powder, it is possible to 3D print FeCo cores with even further attractive properties [31, 32]. These explorations in AM of FeCo alloys show promise in overcoming the workability issues associated with the conventional mechanical processing of FeCo cores, while achieving DC magnetic characteristics close to commercial products.

4.2.2 Iron-Nickel (FeNi)

Iron-nickel alloys, in comparison to iron-cobalt alloys, have a much higher maximum relative permeability, more than 100,000, while saturates at a much lower J_s value, usually between 0.7 and 1.6 T, depending on the nickel wt.% content. Two laser-based AM processes, SLM and LENS, are typically seen in 3D printing of iron-nickel alloys. Reported results on fabricated Fe−30%Ni and Fe−80%Ni showed great potential in achieving magnetic saturation M_s comparable to commercial FeNi at the same nickel wt.%, [33]. Analysis on the relationship between magnetic characteristics and 3D printing parameters found that for printed FeNi alloys, magnetic saturation is significantly influenced by the laser power and the laser scan speed [34, 35]. These printing parameters directly impact the grain size and the density of the fabricated parts, which in turn impacts the magnetic saturation. Optimization of the laser parameters, however, is required for FeNi with different percentages

of Ni content to improve the magnetic saturation J_s value. As shown in [36], for Fe−30%Ni, SLM printed iron alloys show an increase of more than 20% in magnetic saturation when laser speed is increased, while for Fe−80%Ni, the magnetic saturation is slightly decreased as the laser scan speed increases, [35]. Other printing parameters such as laser scan width or the number of scan passes have been found to have a low impact on magnetic saturation J_s, thus optimization of these parameters may not be necessary, [37].

One of the major issues with the FeNi processed with either SLM or LENS is the high intrinsic coercivity H_c. The measured coercivities of the fabricated FeNi alloys range between 80 A/m to 3000 A/m [38, 39], which are much higher than typical values of intrinsic coercivity found in commercial FeNi alloys. High intrinsic coercivity indicates a high hysteresis loss associated with printed FeNi alloys. Additionally, high intrinsic coercivity can have a negative impact toward maximum relative permeability, which is one of the main features of iron-nickel electrical steel. Reduction of intrinsic coercivity in printed iron-nickel is thus important. Analysis has shown that reduction in intrinsic coercivity can be achieved by reducing the porosity level as well as microstructural defects in the printed parts. This can be done by optimization of the laser power and laser scan speed as these parameters have direct influence on the cooling rate and exposure time of the molten pool. These, in turn, impact the defects, porosity, and density levels of printed parts [40]. Alternatively, the coercivity may also be reduced by blending FeNi alloys with additives such as vanadium or molybdenum as shown in [34].

4.2.3 Iron-Silicon (FeSi)

Considering performance per cost, iron-silicon electrical steel variants have high magnetic saturation, high maximum relative permeability, low intrinsic coercivity, low hysteresis loss,

and low eddy current loss up to hundreds of Hz in excitation frequency. Variants of iron-silicon electrical steel are thus found in most iron cores used in electrical machines, [2]. In pursuit of additively manufactured iron cores, most research and development activities for 3D printed ferromagnetic materials also focus on iron-silicon.

Similar to the 3D printing of iron-cobalt and iron-nickel, SLM is the most employed AM process for iron-silicon. In [41], SLM is proposed as an alternative method to produce iron-silicon with silicon content at 6.9%wt., which is brittle and challenging to produce with via conventional manufacturing method. Here, the investigation of the SLM printing parameters on the magnetic properties shows that there is a non-linear relationship between laser energy input and the relative permeability, intrinsic coercivity, and the total loss density of the printed iron-silicon. It is thus important to optimize the printing process to obtain optimal magnetic performance of printed iron-silicon. The nature of the SLM method, however, introduces defects and residual stresses on the microstructures of the printed parts, which hinders the magnetic properties of SLM iron-silicon. Compared to commercial iron-silicon lamination steel, the maximum relative permeability of as-built iron-silicon from the SLM process is lower, [41,42]. Applying heat treatment to the as-built parts can help remove residual stresses and significantly improve the relative permeability as well as other magnetic properties of SLM iron-silicon [43]. In [44], the annealing process is shown to improve the maximum relative permeability of as-built parts, from an approximate value of 2000 to more than 24,000, which is on par with high performance iron-silicon steel laminations. Other magnetic properties, including total iron loss density, intrinsic coercivity, and saturation are also positively impacted via the annealing process.

Another interesting characteristic of the SLM process is that it introduces grain elongation in the build direction of the printed parts. As a result, iron-silicon fabricated using SLM

can have high levels of magnetic anisotropy [45]. Additionally, higher laser energy input can even change the crystallographic texture of the printed iron-silicon, leading to the formation of Goss texture also known as cube-on-edge texture, which is seen in grain-oriented electrical steel, [46]. This suggests that SLM can be potentially used as an alternative approach in producing grain-oriented iron-silicon, which in turns can be used for applications such as transformers or large electrical machines.

To avoid the effect of residual stress caused by the local melting due to the laser energy source as in SLM, other AM techniques have also been explored. In [18], FeSi sample is prepared using 3D screen printing and then compared with commercially available FeSi lamination steel. In this AM process where the powder is held together via binder, the printed part is heat-treated uniformly upon printing completion. The magnetic induction and relative permeability at low magnetic field strength are comparable to commercial FeSi steel. However, the magnetic saturation of screen-printed iron-silicon is lower than commercial lamination equivalent, owing to the low density and high porosity level of printed parts.

Binder jet printing (BJP) is another AM technique that does not use laser as an energy source. As a laser is not used to melt the powder particles together, there is no grain elongation associated with the BJP process. Thus, an advantage of the BJP process is that it can produce iron-silicon with low level of magnetic anisotropy.

4.2.4 Performance summary of printed soft magnetic materials

There are promising results at this early stage of AM for soft magnetic materials for electrical machines. AM allows freedom in design of magnetic cores, which can increase the performance of electrical machines. Additionally, magnetic properties of 3D printed materials, especially iron-silicon, are improving and reaching the levels of many commercial

electrical steel laminations as well as SMCs, as shown in Figure 4.6. Maximum relative permeability of printed iron-silicon is high and comparable to iron-silicon steel lamination, especially when the printed sample is heat-treated, Table 4.1, [19, 41, 44, 47]. As the AM iron-silicon samples undergo post-processing heat treatment steps, their grain size can significantly improve, which in turn leads to higher magnetic induction and permeability.

Table 4.1: Comparison of grain size and maximum relative permeability between as-built and heat-treated printed soft magnetic materials.

	Grain Size (µm)	**Max Relative Permeability μ_{max}**
As-built	10–200	1200–5500
Heat-treated	400–1000	10,500–31,000

4.3 Magnetic characterization techniques

Magnetic characterization techniques that are suitable for soft magnetic materials are outlined here. The DC magnetic characterization is used to extract the initial magnetization curve and the hysteresis loop of the soft magnetic materials. The AC magnetic characterization extracts the frequency dependent $B - H$ curves and specific loss density curves. The magnetic anisotropy characterization extracts the BH characteristics of the soft magnetic materials under different excitation directions. Magnetic characterization of these quantities provide insight on the performance of the materials of interest.

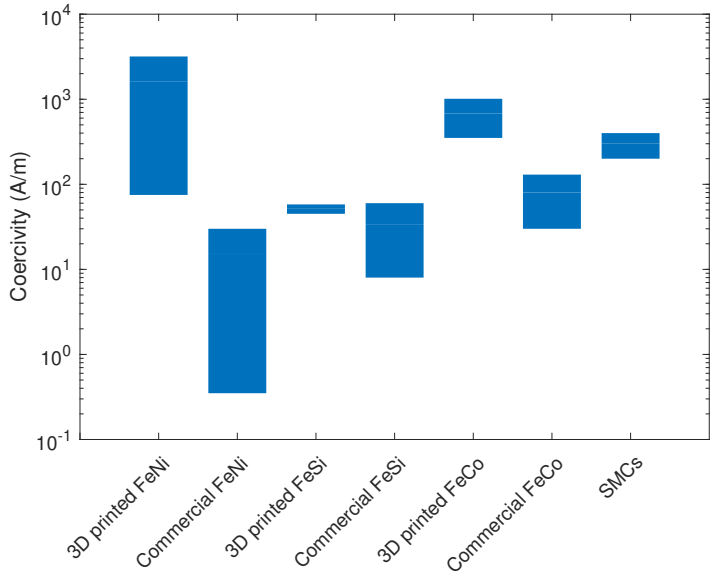

(a) Comparison between reported coercivity of 3D printed electrical steels, commercial electrical steels, and SMCs.

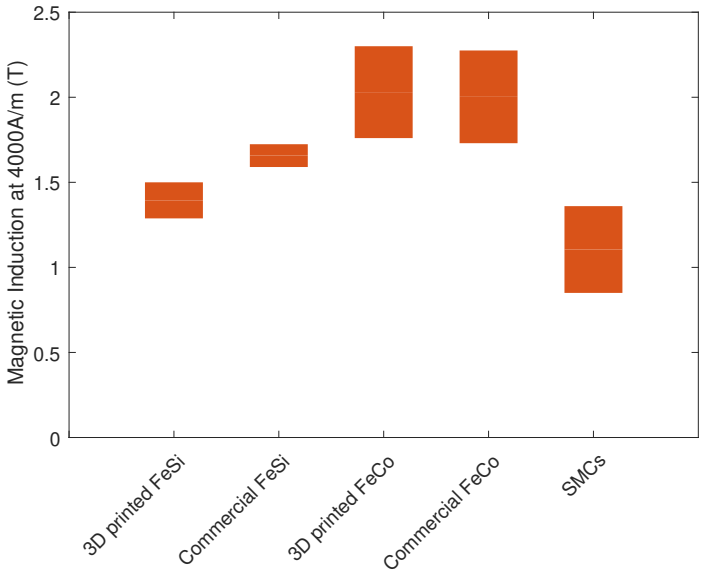

(b) Comparison between reported magnetic induction at 4 kA/m, B_{40}, of 3D printed electrical steels, commercial electrical steels, and SMCs.

Figure 4.6: Comparison between additively manufactured and commercial electrical steel.

4.3.1 DC characterization

The DC magnetic characterization provides important magnetic properties of soft magnetic materials under DC excitation condition. In other words, the extracted characteristics

are time independent. In general, the extracted characteristics are in the form of the initial magnetization curve and the hysteresis loop, as shown in Figure 4.7. From this information, remanent flux density, B_r, saturation polarization, J_s, and coercive force, H_c, can be readily extracted.

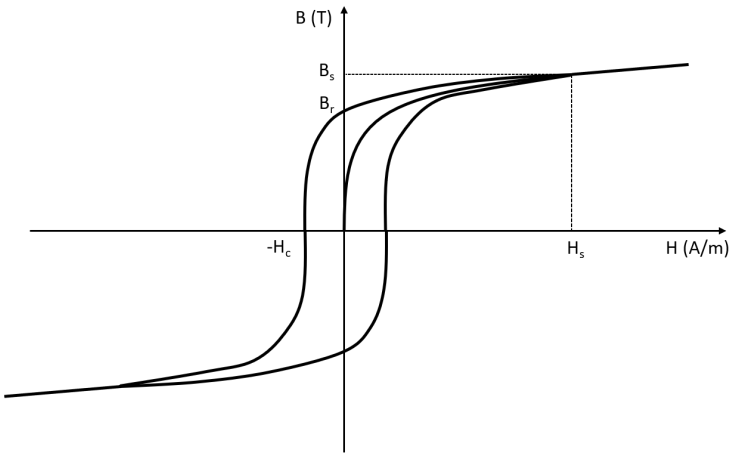

Figure 4.7: Illustration on initial magnetization curve, static hysteresis loop, and important magnetic characteristics of a general soft magnetic material.

The extraction of DC characteristics depends on the shape of the soft magnetic specimen. For a ring specimen, the method for extraction can be generally described as in Figure 4.8. Here, the ring specimen forms the closed magnetic circuit and is wound with secondary windings (inner layer) and primary windings (outer layer). The static $B-H$ characteristics of the ring specimen can be calculated using Ampere's circutal law and Faraday's magnetic induction law as shown in (4.7) and (4.8). Using a fluxmeter employing integration techniques [48], the induced voltage on the B coil (search coils/ secondary coils) is used to estimate the magnetic induction. Here, l_m and A are the length of the magnetic path and cross section area of the ring specimen, N_1 and N_2 are the number of turns in the primary and secondary windings, and I is the current in the primary windings. It is important to note that the ratio between the outer diameter and inner diameter of the ring specimen should be smaller

than 1.4 to ensure uniform magnetic flux distribution in the ring specimen, [28].

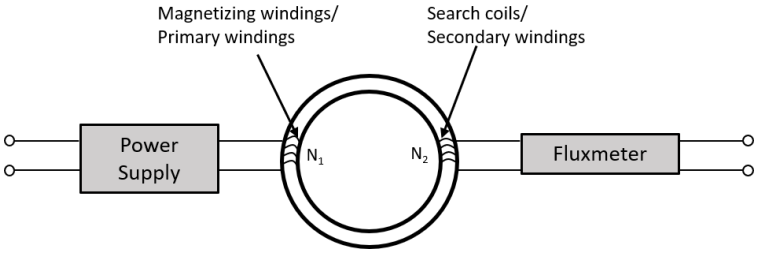

Figure 4.8: General description of the magnetic characterization test bed method using a ring specimen. Additional apparatus are connected to the test bed to extract the desired magnetic properties of the specimen.

$$\oint_{l_m} \vec{H} \cdot \vec{dl} = N_1 \cdot I \tag{4.7}$$

$$\oint_{l_m} \vec{E} \cdot \vec{dl} = -N_2 \cdot \frac{d\phi}{dt} = -N_2 \cdot A \cdot \frac{dB}{dt} \tag{4.8}$$

There are two methods to provide the excitation and obtain the DC characteristics of the test soft magnetic specimen. In the first method or also known as point-by-point method, the magnetization field strength is controlled such that it changes in a step wise manner, as shown in Figure 4.9. Demagnetization is implemented prior to the magnetization of the specimen, by applying the magnetic field strength and changing its polarity. The changes in the magnetization, or ΔH, is then varied so that the change in the magnetic flux density ΔB is constant, Figure 4.10. The magnetization curve is then obtained in a point-by-point fashion.

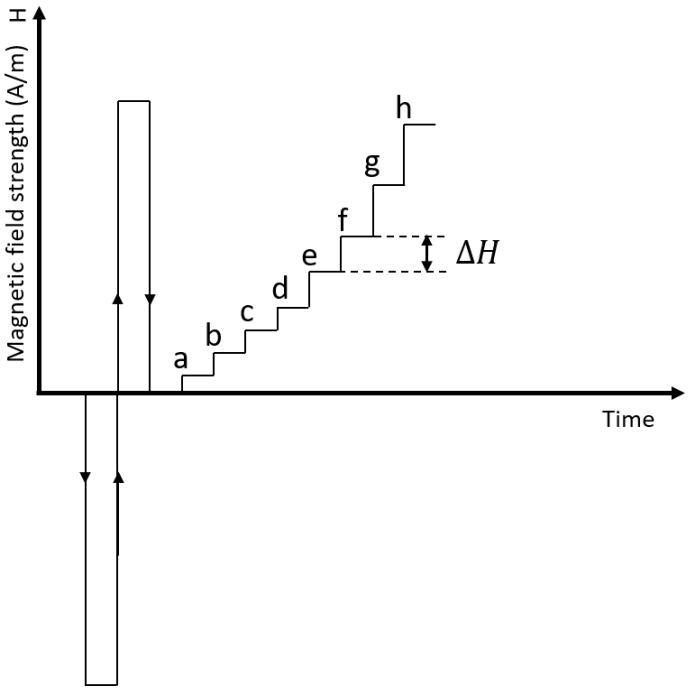

Figure 4.9: Illustration of the point-by-point excitation approach to the primary windings/ magnetization windings.

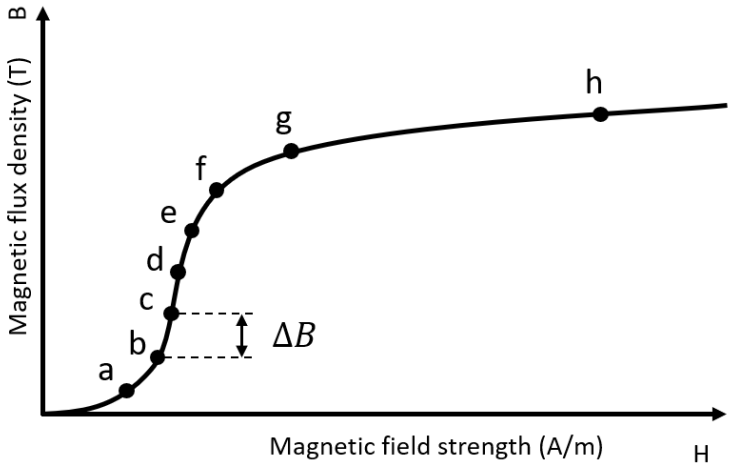

Figure 4.10: Illustration of the point-by-point method of obtaining the magnetization curve.

In practice, DC magnetic characterization is usually achieved with continuous excitation to the primary windings. This process is called quasi-static excitation, where the excitation frequency is very low, typically much lower than the Wolman frequency, f_w. The Wolman

frequency is defined as the cut-off frequency where the permeability of the soft magnetic specimen is reduced when it is excited above f_w, due to eddy current effect. Thus, when the soft magnetic specimen is characterized under quasi-static condition, the eddy current effect is negligible; the extracted initial magnetization curve and hysteresis loop is of little difference compared to the static properties, [49]. It is important to note that the excitation frequency and the obtained rate of change of the magnetic induction, $\frac{dB}{dt}$, must be carefully tuned in the controller so that the eddy current effect is negligible.

Figure 4.11 illustrates the quasi-static excitation input. Upon completion of the demagnetization process, the specimen is excited with continuous application the magnetic field strength, via the primary windings, at a very slow rate. Here, H is applied from zero to the maximum desired field strength, and then gradually reduced to the negative maximum value, then increased again to the maximum field strength one more time. The waveform of magnetic flux density is continuously recorded as a function of time, and has the form similar to the curve shown in Figure 4.7. Here, as the excitation increases from zero to maximum for the first time, the initial magnetization curve is recorded.

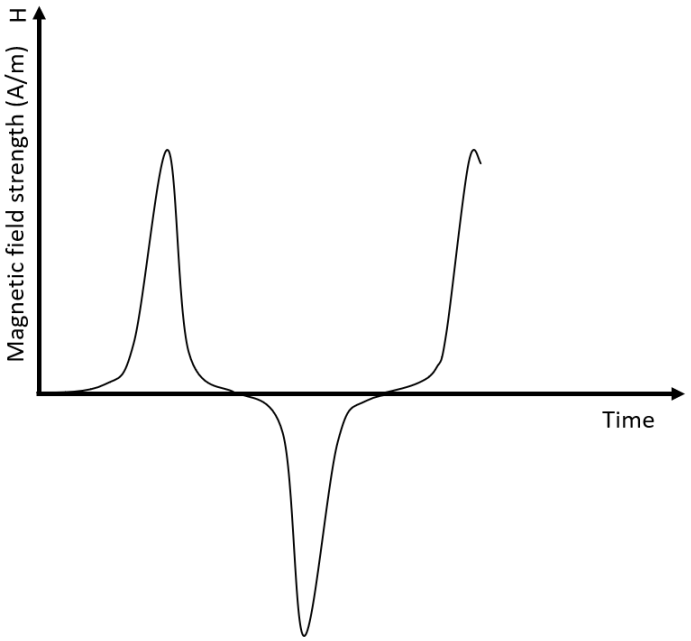

Figure 4.11: Illustration of the continuous excitation of the magnetic field strength under quasi-static condition.

4.3.2 AC characterization

The AC magnetic characterization provides the measurements of the soft magnetic materials under AC excitation condition. The excitation frequency can be varied from the line frequency, 50 Hz up to 20000 Hz, [50]. Similar to the DC magnetic characterization, the AC magnetic characterization employs closed magnetic circuit, and also depends on the shape of the specimen.

For a ring or toroidal shape specimen, the voltmeter-ammeter method [50] can be applied, Figure 4.12. Here, the magnetizing windings are provided with the excitation current $I(t)$ at the test frequency, while the induced voltage on the secondary windings, $U(t)$, is measured using the voltmeter. The excitation current is controlled such that the induced voltage remains within the sinusoidal waveform during the entire magnetization process. The quality of the sinusoidal signal is determined by the use of sinusoidal form factor value of $1.11 \pm 1\%$.

The form factor of a signal is defined as the ratio between the RMS value, U_{rms}, as shown in (4.9), and the average rectified value of the signal, $|\bar{U}|$, as in (4.10). Here, T is the period of the excitation frequency.

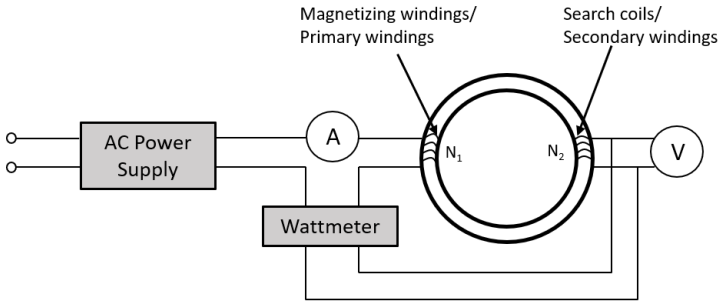

Figure 4.12: Illustration of the test bed of AC magnetic characterization using voltmeter-ammeter method on a ring specimen.

$$U_{rms} = \sqrt{\frac{1}{T}\int_0^T U(t)^2 dt} \tag{4.9}$$

$$|\bar{U}| = \frac{1}{T}\int_0^T |U(t)| dt \tag{4.10}$$

When the form factor of the induced secondary voltage remains within 1.11±1%, the magnetic induction can be calculated as in (4.11), where f is the excitation frequency, A is the cross section area of the ring specimen, and N_2 is the number of turns on the secondary windings. The magnetic field strength associated with the excitation current $I(t)$ is calculated using Ampere's law, as shown in (4.12). Here, N_1 is the number of turns on the magnetizing windings and $\hat{I}$ is the peak value of the excitation current.

The specific loss density, p_c, which includes the hysteresis loss, the eddy current loss, and the excess loss, is calculated as in (4.13). Here P_m can be measured using the wattmeter, where P_m represents the active power of the excitation current $I(t)$ and the secondary voltage

$U(t)$, m is the mass of the ring specimen, and K is the correction factor for the losses due to the wattmeter.

$$B = \frac{\sqrt{2} \cdot U_{rms}}{2 \cdot \pi \cdot N_2 \cdot A \cdot f} \tag{4.11}$$

$$H = \frac{N_1 \cdot \hat{I}}{l_m} \tag{4.12}$$

$$p_c = \frac{1}{m}\left(\frac{N_1}{N_2} P_m - K\right) \tag{4.13}$$

4.3.3 Hysteresis loss characterization

Hysteresis loss can be acquired from the hysteresis loops achieved using quasi-static magnetic characterization. Assuming the model of hysteresis loss of soft magnetic materials in (4.14), for each peak value of magnetic induction $\hat{B}$, the hysteresis loss linearly increases with the excitation frequency f. Here, γ is the measured density of the material. For the quasi-static characterization at 1 Hz, the estimation of the hysteresis loss per cycle (p_h/f) at $\hat{B}$ can then be acquired from the area enclosed by the quasi-static hysteresis loop at that $\hat{B}$. Given different levels of magnetic induction, a model of a hysteresis loss as a function of B can be found.

$$p_h(\hat{B}) \sim \frac{f}{\gamma} \tag{4.14}$$

Chapter 5

Magnetic Properties of Printed Soft Magnetic Materials

The two AM methods that are used to fabricate samples for the magnetic characterization in this chapter are binder jet printing (BJP) and fused filament fabrication (FFF). This chapter provides the general description for the AM methods. The chapter then experimentally demonstrates the ability of AM to achieve variable levels of maximum relative permeability, and low hysteresis loss in comparison to commercially available soft magnetic composites.

5.1 Methods for sample preparation

5.1.1 Binder jet printing

BJP is categorized as a powder bed AM technique that does not utilize a concentrated energy source as in SLM or electron beam melting. The overall printing process is illustrated in Figure 5.1. Here, the starting powder is first prepared by mixing iron alloy, pure iron, and pure silicon spherical powder together prior to printing. A certain amount of boron is also added into the powder mixture to help the sintering step (e) as well as to manipulate loss characteristics. The starting powder is summarized in Table 5.1.

Table 5.1: Material used

Powders		**Particle Size Distribution**	**Shape**
Main powder	Iron alloy	$\leq 106\,\mu m$	Near spherical
	Fe	$\leq 10\,\mu m$	
	Si	$1\,\mu m$	
Sintering additive	B	$1\,\mu m$	N/A

The BJP process produces parts by printing individual layers until completing a part. The X1-Lab, manufactured by ExOne (Huntington, PA, USA), is used in this work. The printer has two powder beds, the supply bed, with the starting powder, and the build bed, where the part is being deposited and printed, as shown in Figure 5.1. For each layer, the printing process can be described in two-steps: (a) powder spreading and (b) binder injection. The roller spread each layer of powder from the supply bed into the build bed and the binder phase is injected selectively based on the computer aided design (CAD) file. Printing a layer is then repeated until the 3D part is completed. At this stage, the formed 3D part consists of the powder held together with the binders. The printed part is still fragile, which requires the binder phase to be cured for 2 hours to provide the strength of the printed part before removing the loose powder, Figure 5.1(d). The cured part is finally placed in an environment-controlled furnace for sintering for an additional 6 hours.

5.1.2 Fused filament fabrication

Fused filament fabrication (FFF) is a material extrusion based AM technique that is suitable for either single material or multi-material printing. Typical FFF systems use one

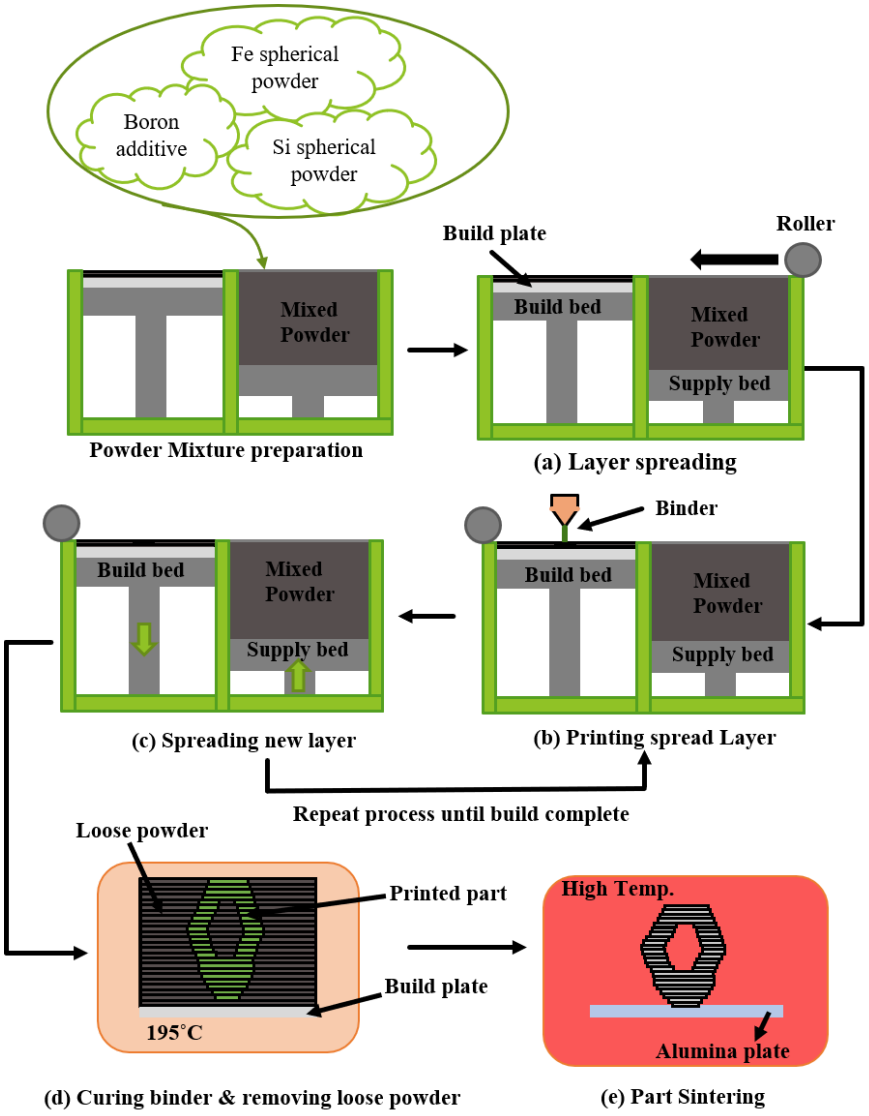

Figure 5.1: Schematic of the binder jet printing process.

or more nozzles to continuously deposit materials layer by layer onto the build platform. Different materials, including polymers, composites, ceramics, or metals, can be used as separate filament for individual nozzle. Thus, FFF and other similar material extrusion based techniques are capable of fabricating multi-material structures.

The preparation of the starting filament used for the FFF method includes mixing iron powder/ iron alloy powder with varied binder polymer compositions, and elastomer. The prepared filament is then wound on a spool and then fed to a FFF printer (Renkforce

1000). The temperature of the building bed is set at 60°C, while the filament in the nozzle is heated at a printing temperature of 160-170°C. Printed ring samples are then sintered in environment-controlled furnace after the debinding process, at a temperature of 900°C. Details of the printing process can be found in [51].

5.1.3 Sample description

To demonstrate the variable relative permeability achievable with BJP or FFF printing methods, 11 samples are characterized. The printing parameters and the measured density of the samples are shown in Table 5.2 and Table 5.3. The OD and ID of the CAD file, which is used to provide the .STL format for printing, are selected such that the OD/ID ratio is less than 1.4, 38 mm and 32 mm, respectively. Upon printing completion, the ring samples are wound with AWG28 for the secondary windings and AWG22 for the primary windings. The number of turns for the primary windings is adjusted so that maximum relative permeability and magnetic induction at 500 A/m are achieved.

For hysteresis loss demonstration, 8 samples are characterized. The BJP method is used to prepare these 8 samples, with descriptions as shown in Table 5.4.

5.2 Results

Maximum relative permeability $\mu_{r,max}$ and the hysteresis loss per cycle p_h/f are the primary focus of the characterization. They are extracted via implementation of the quasi-static characterization. Other magnetic properties extracted via quasi-static characterization include the intrinsic coercivity H_c, the remnant flux density B_r, and the magnetic induction at 500 A/m, B_5. For AC magnetic characterization, the specific loss density curves at

Table 5.2: Summary of parameters for BJP method for fabricating ring samples for variable relative permeability demonstration.

Composition	Starting powder	Sintering Temperature	Sintering Environment	Density (g/cm^3)
$Fe_{97}Si_3$-0.25BN_3	Fe, Si, Boron Nitride	1200°C	Argon	5.61
$Fe_{97}Si_3$-0.25B	Fe, Si, Boron	1200°C	Argon	7.06
$Fe_{95}Si_5$-0.25B	Fe, Si, Boron	1200°C	Argon	7.25
$Fe_{97}Si_3$-0.25B	Fe, Si, Boron	1250°C	Argon	6.69
$Fe_{95}Si_5$-0.25B	Fe, Si, Boron	1250°C	Argon	7.17
$Fe_{95}Si_5$	FeSi alloy, Fe	1200°C	Argon	7.17
$Fe_{95}Si_5$-0.25B	FeSi alloy, Fe, Boron	1200°C	Argon	7.44
$Fe_{95}Si_5$-0.25B	FeSi alloy, Fe, Boron	1200°C	Vacuum	7.40

Table 5.3: Summary of parameters for FFF method for fabricating ring samples for variable relative permeability demonstration.

Filament composition	Iron loading %	Density (g/cm^3)
Fe & Polymer binder	Low	2.96
Fe & Polymer binder	High	3.79
FeSi alloy & Polymer binder	High	4.73

excitation frequencies of 50, 200, and 400 Hz are also extracted. Table 5.5 summarizes the magnetic characteristics that are extracted.

Table 5.4: Summary of parameters for BJP method for fabricating ring samples for hysteresis loss analysis. All the samples here are sintered in Argon environment.

Composition	Starting powder	Sintering Temperature	Density (g/cm^3)
$Fe_{97}Si_3$	Fe, Si	1200°C	7.03
$Fe_{97}Si_3$-0.25B	Fe, Si, Boron	1200°C	7.06
$Fe_{95}Si_5$	Fe, Si	1200°C	7.02
$Fe_{95}Si_5$-0.25B	Fe, Si, Boron	1200°C	7.25
$Fe_{97}Si_3$	Fe, Si	1250°C	7.08
$Fe_{97}Si_3$-0.25B	Fe, Si, Boron	1250°C	6.69
$Fe_{95}Si_5$	Fe, Si	1250°C	7.02
$Fe_{95}Si_5$-0.25B	Fe, Si, Boron	1250°C	7.17

Table 5.5: Overview on extracted magnetic characteristics.

	Characteristics
DC characterization	Maximum relative permeability $\mu_{r,max}$ Intrinsic coercivity (H_c) Magnetic induction @ 500 A/m (B_5) Hysteresis loss per cycle (p_h/f)
AC characterization	Loss curves at 50, 200, and 400 Hz

5.2.1 Experimental setup

The ring core test setup, following two international standards, is used to characterize the additively manufactured iron silicon ring samples. Standard ASTM A773, [52], is used

for the DC magnetic characterization; and standard ASTM A927, [53], is used for the AC magnetic characterization. The measurement scheme of the experimental setup is shown in Figure 5.2. Here, the power amplifier, Model 7224 from Magnetic Instrumentation, is connected to the DAQ module, which is used to send excitation signals to the primary winding of the ring sample. The measured excitation current, via a current shunt, is fed back to the computer to calculate the magnetic field strength (H). The secondary winding of the sample is connected to both the fluxmeter, which is used to calculate magnetic induction (B) within the DC characterization, and the voltage transducer, which is used for the AC characterization.

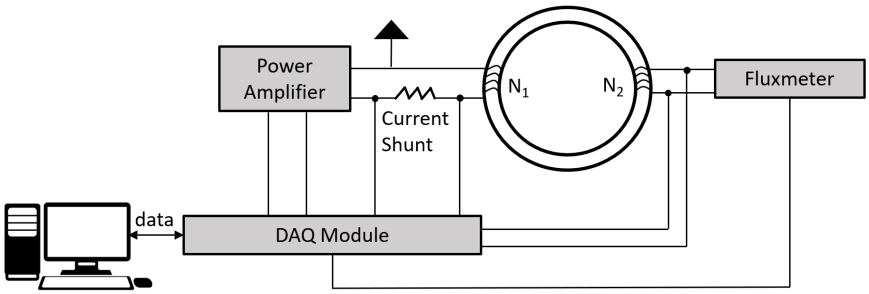

Figure 5.2: Schematic of experimental setup of the ring core DC/ AC magnetic characterization.

For the DC characterization, quasi-static excitation is provided to the primary windings of the samples. The excitation frequency of the quasi-static characterization is kept at approximately 1 Hz. The digital fluxmeter, Model 2130 Magnetic Instrumentation, is used to measure the change in magnetic flux in the secondary winding. For the AC characterization, excitation is provided to the primary windings at frequencies of 50, 200, and 400 Hz. The induced secondary voltage, measured from the voltage transducer, is used to calculate magnetic induction within the ring sample.

Two different soft magnetic samples were used to validate the experimental setup: a

SMC ring, Siron®S280b, and a laminated steel ring, M-27 (24 gauge). The dimensions of the SMC ring were 104 mm outer diameter, 75 mm inner diameter, and 14.2 mm height. The dimensions for the laminated ring were 51 mm outer diameter, 42.5 mm inner diameter, and 6.35 mm height.

As shown in both Figure 5.3 and Figure 5.4, the experimental data at 50 Hz excitation frequency tracks well with the data sheet values provided by the manufacturer. The total iron loss curve at 50 Hz for the SMC sample is slightly higher than the data sheet values. The differences between the extracted iron loss and the data sheet in Figure 5.4b may come from the mechanical cutting and handling of the SMC sample to form the ring. Another contribution to the differences may come from the difference in size between the SMC test ring here and the ring from the manufacturer.

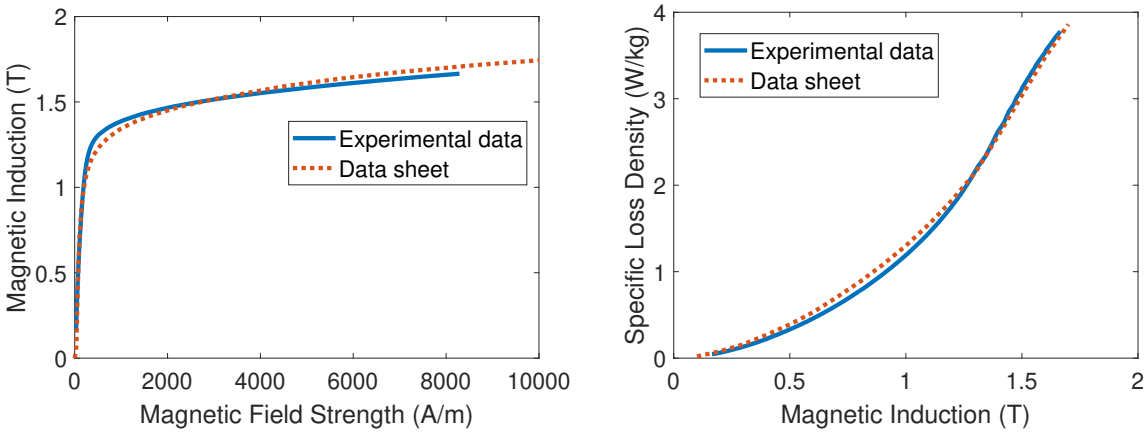

(a) BH curve

(b) Specific loss density

Figure 5.3: Comparison between experimental results of the M-27 (24 gauge) laminated ring and its data sheet values. AC excitation is at 50 Hz.

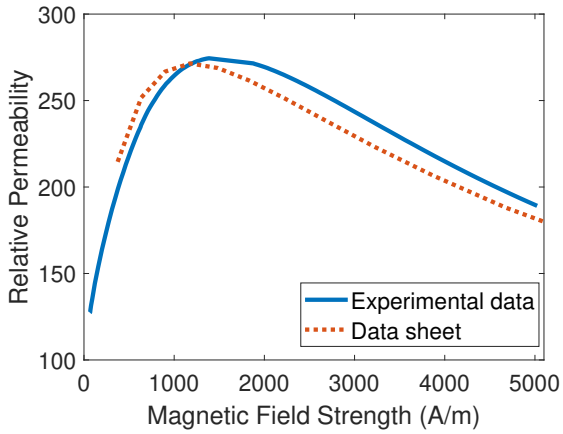

(a) Relative permeability

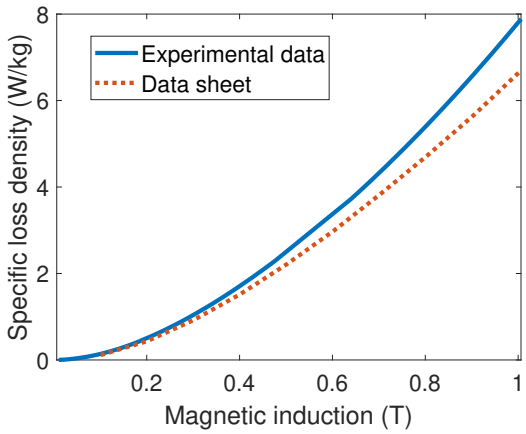

(b) Specific loss density

Figure 5.4: Comparison between experimental results of the Siron®S280b SMC sample and its data sheet values. AC excitation is at 50 Hz.

5.2.2 Variable relative permeability

Variable levels of maximum relative permeability $\mu_{r,max}$ are achieved with both BJP and FFF methods. For the BJP method, if pure iron powder is used in the starting powder, $\mu_{r,max}$ can be varied between 1000 to 3500 depending on the silicon content and the use of boron nitrate or boron, as shown in Figure 5.5.

If iron alloy powder is used instead of pure iron powder, $\mu_{r,max}$ can be varied between 3000 and 6000, depending on the use of boron as well as the sintering environment, as shown in Figure 5.6. Here, when the ring sample is sintered in vacuum environment-controlled furnace, $\mu_{r,max}$ can be higher in comparison to samples sintered in Argon environment.

The FFF printing method can also provide variable levels of $\mu_{r,max}$ as shown in Figure 5.7. Here, $\mu_{r,max}$ can change between 1.2 when the starting filament is created with low iron loading content up to 2700 when the starting filament is created with iron alloy content.

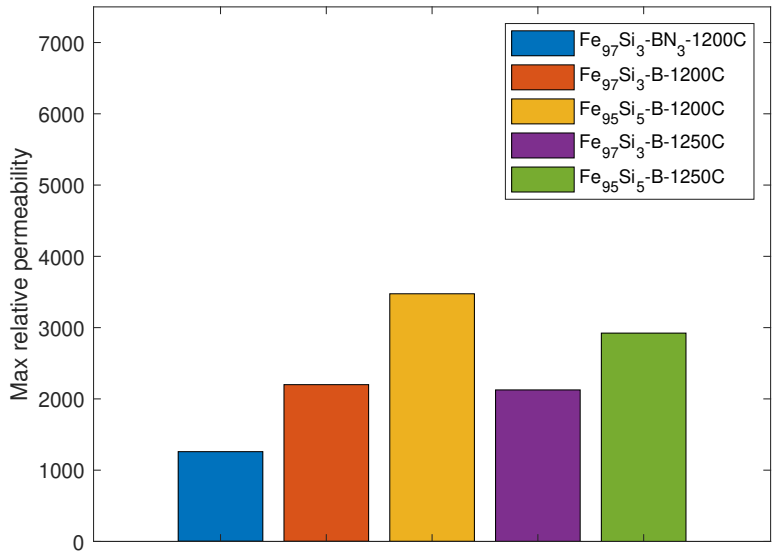

Figure 5.5: Variable levels of maximum relative permeability achieved with BJP method. Here, the starting powder includes mixture of pure iron powder and silicon powder. The results are achieved at quasi-static testing condition.

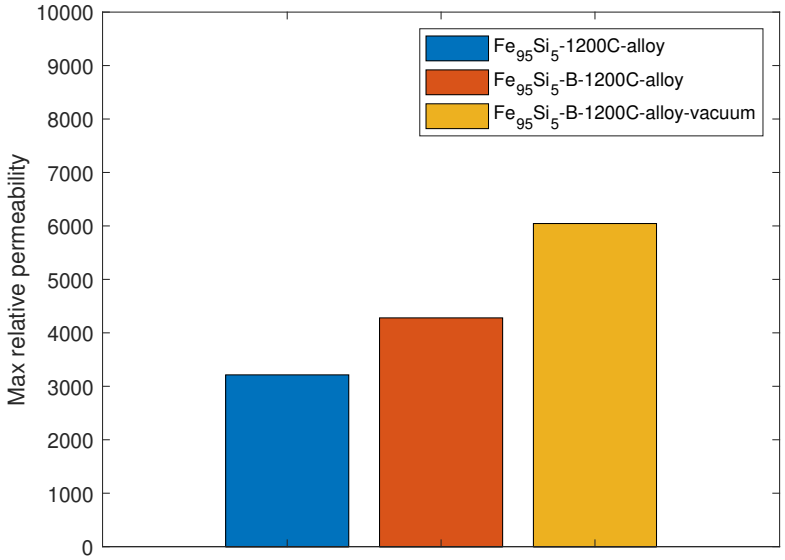

Figure 5.6: Variable levels of maximum relative permeability achieved with BJP method. Here, the starting powder includes mixture of iron alloy powder. The results are achieved at quasi-static testing condition.

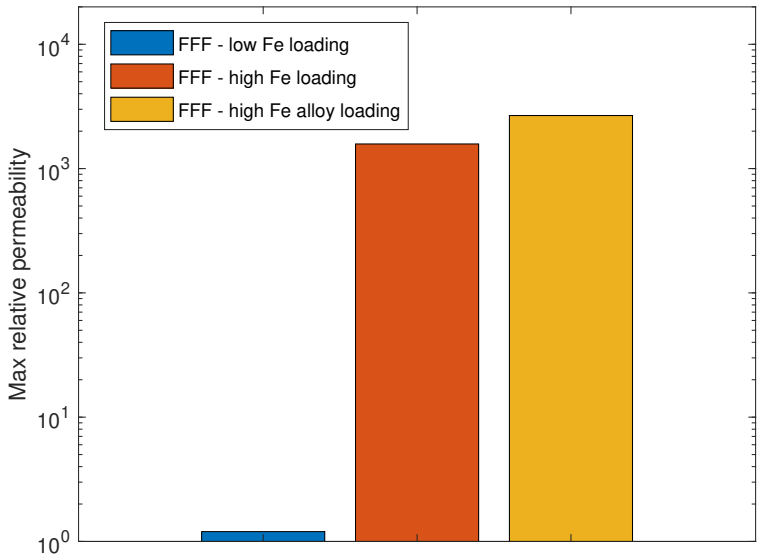

Figure 5.7: Variable levels of maximum relative permeability achieved with FFF method. Here, the starting powder includes mixture of iron or iron alloy powder. The results are achieved at quasi-static testing condition.

5.2.3 Hysteresis loss

The hysteresis loss for printed iron samples, prepared with BJP method, is low in comparison to SMC. At 1 T, the hysteresis loss per cycle varies between 0.04 Ws/kg to 0.06 Ws/kg as shown in Figure 5.8. Among these eight BJP samples, the sample with $Fe_{95}Si_5$ with boron, sintered at 1200 °C exhibited the lowest intrinsic coercivity and the lowest p_h/f. A direct comparison of this sample with a commercial SMC sample showed that the hysteresis loss density per cycle of BJP iron silicon can be up to 70% lower than SMC, as shown in Figures 5.9 and 5.10. However, it is clear that commercially available steel laminations exhibit the lowest hysteresis loss.

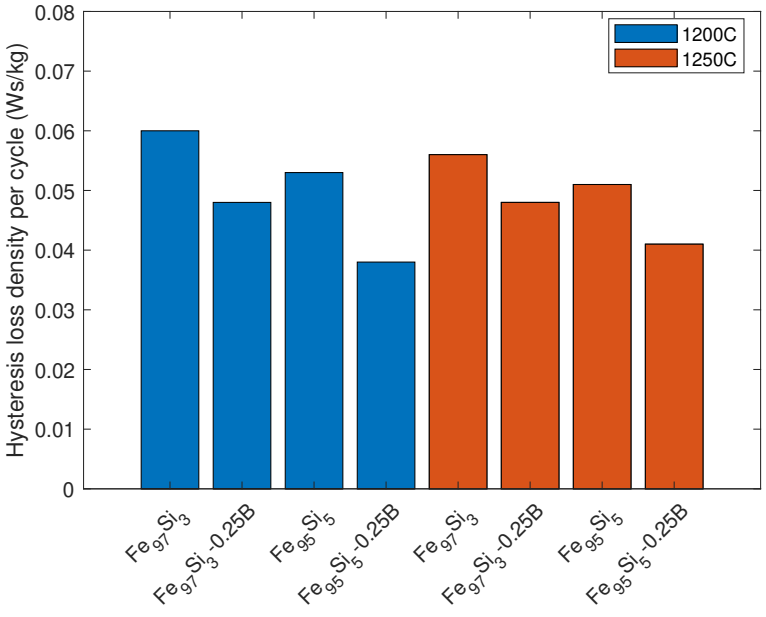

Figure 5.8: Variation in hysteresis loss density per cycle at 1 T of BJP iron silicon.

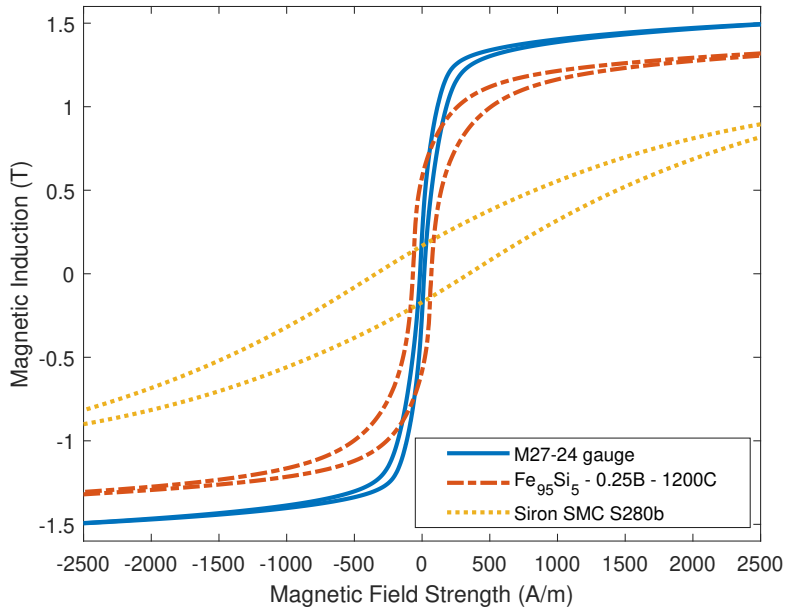

Figure 5.9: Experimental quasi-static hysteresis loops between laminated iron silicon, binder jet printed sample, and SMC sample.

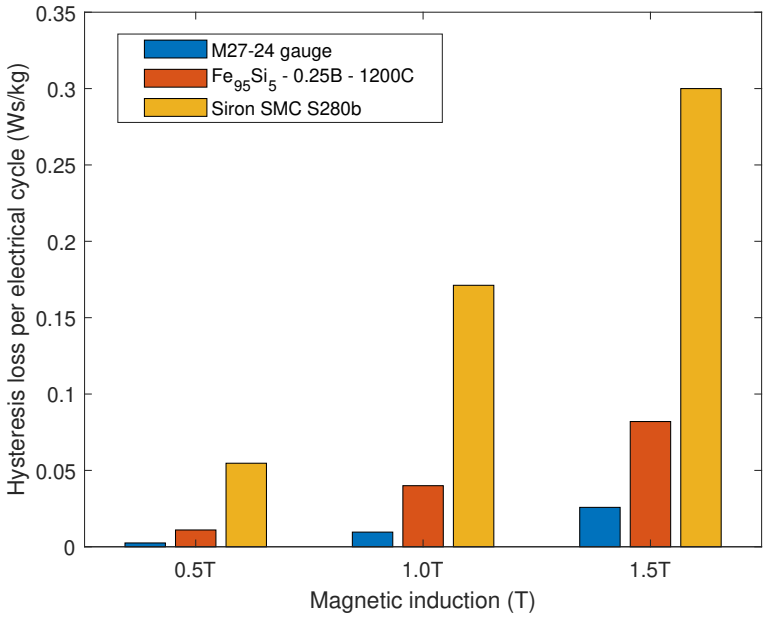

Figure 5.10: Comparison of hysteresis loss per electrical cycle between laminated iron silicon, binder jet printed sample, and SMC sample. The printed sample here has the best performance among the 8 printed samples.

Chapter 6

Magnetic Anisotropy

Different type of soft magnetic materials has different magnetic anisotropic behaviors. Non-oriented steels have similar magnetic properties in the in-plane directions. Thus, they are typically used in small and medium radial rotating electrical machines. Oriented steels have better $B - H$ and specific loss density performance in the easy axis direction. As a result, they have been proposed to used to build segments for segmented electrical machines to leverage their preferred magnetization direction. For machine topologies that require 3D flux paths including axial flux, claw pole, and transversal flux machines, soft magnetic composites (SMCs) are typically used, due to their low magnetic anisotropy.

Each AM method has different set of printing parameters and ways to bond the particles/ filament together. Magnetic anisotropic behaviors of additively manufactured iron cores thus depend on the AM method as well as its printing parameters and the tuning of the parameters. Magnetic anisotropy characterization is thus important in the development and understanding of additively manufactured iron cores.

This chapter discusses a simplified magnetic anisotropy characterization technique. The chapter starts with literature review on methods to analyze magnetic anisotropy of soft magnetic materials. Development and verification for the magnetic anisotropy characterization are then shown, following by the experimental results.

6.1 Magnetic anisotropy characterization methods

For steel laminations, standard Epstein frame testing can provide the magnetic anisotropy behaviors in the in-plane directions. In the stacking direction, the correction of the permeability can follow (6.1). Here, $\mu_{r,z}$ is the relative permeability of the steel in the stacking direction, μ_r is the relative permeability of the steel in the in-plane directions, μ_{air} is the relative permeability in vacuum which is 1, and k is the lamination factor.

$$\frac{1}{\mu_{r,z}} = \frac{k}{100} \cdot \frac{1}{\mu_r} + (1 - \frac{k}{100}) \cdot \frac{1}{\mu_{air}} \tag{6.1}$$

For SMCs, they are made by compressing water atomized, insulated iron alloy powders to desired geometries. Ring core test is the preferred method to characterize SMCs to provide their magnetic behaviors. For three dimensional-magnetic characterization, different techniques have been proposed. In [54], a quasi-three dimenisional magnetic characterization technique is developed, as shown in Figure 6.1. Here, a 2D single sheet tester, as shown in Figure 6.1a is used to extract the magnetic properties in three dimensions of Somaloy 500 SMC material. Three different square slices of 50x50 mm with 2 mm thickness are cut from an SMC disk at three different orientations, as shown in Figure 6.1b. The square samples are then inserted into the single sheet tester in order to extract the three dimensional magnetic properties of the SMC material. This method required cutting of the sample, which can inadvertently lead to degradation of the material properties, [55], which can mask the magnetic anistropy characterization.

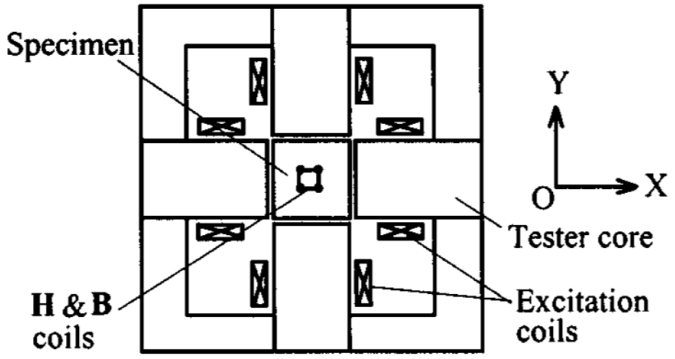

(a) Quasi-magnetic anisotropy characterization test bed

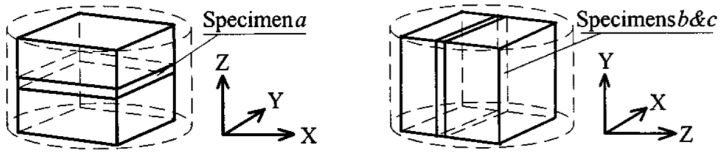

(b) Sample preparation

Figure 6.1: Quasi-magnetic anisotropy characterization setup [54].

Improved methods for magnetic anisotropy of soft magnetic materials are demonstrated in [56, 57]. However, the methods require the development of multiple search coils as well as a complex spider system to mount the sample for the anisotropy characterization process, as shown in Figure 6.2. Here, six different search coils are required; they are then wound on printed circuit boards and mounted on all sides of a cubic SMC sample, as shown in Figure 6.3. This characterization technique can be complex. A simpler magnetic anisotropy test bed can thus be developed to remove the requirements of the spider system and the use of multiple search coils.

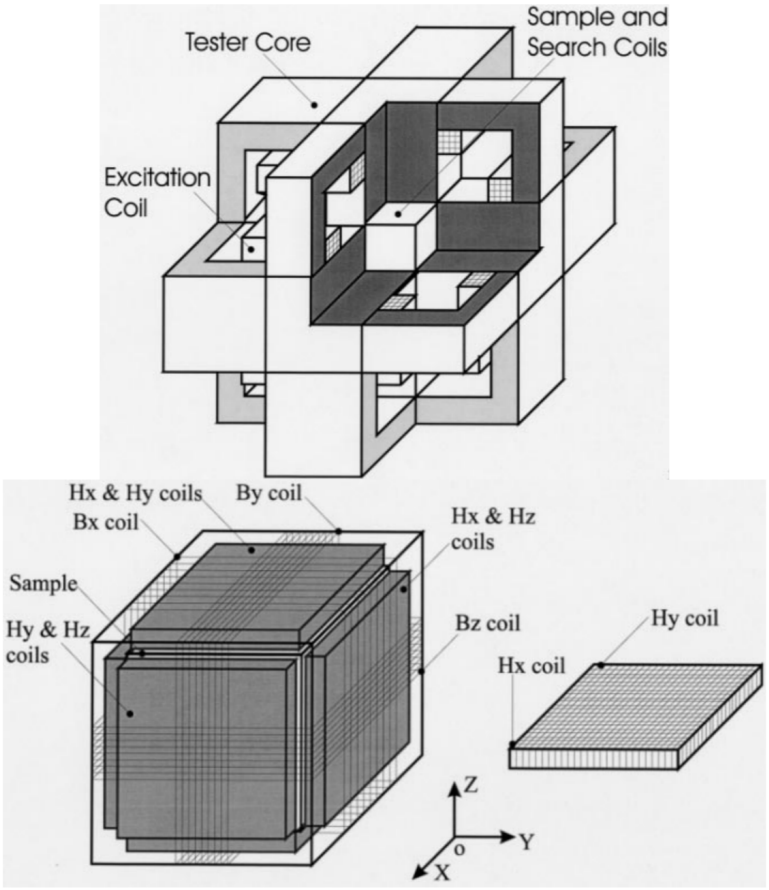

Figure 6.2: Complex magnetic anisotropy characterization test bed for soft magnetic materials [56].

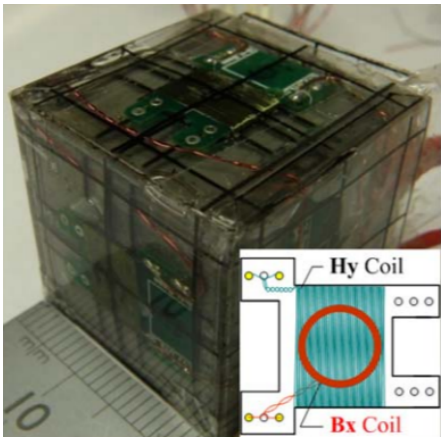

Figure 6.3: Sample preparation for the complex magnetic anisotropy characterization test bed [57].

6.2 Simplified test bed development

The simplified magnetic anisotropy characterization test bed is used to provide magnetic anisotropy behaviors of electrical steel, produced via AM or powder mettalurgy with less components. The main objective of the magnetic anisotropy characterization is to obtain the magnetization curves under excitation in the X-, Y-, and Z- directions. This characterization provides the coupled relationship between the magnetic field intensity H_x, H_y, and H_z and the magnetic induction B_x, B_y, and B_z.

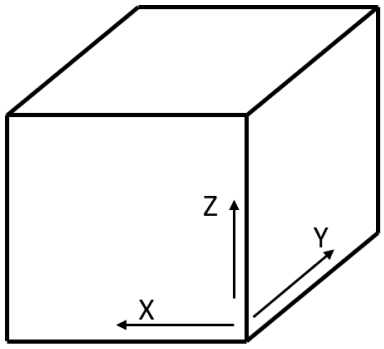

Figure 6.4: Illustration of the cube sample and the designated X-, Y-, and Z- directions.

A cubic sample with equal cross sectional area on each face, as shown in Figure 6.4, will allow independent excitation in each direction. The magnetization curve for each direction can be obtained when excitation is applied perpendicular to the cube face of interest. Particularly, the $B_x - H_x$ relationship can be acquired when the excitation is applied to the YZ-plane of the cube. For other directional $B - H$ relationships, they can be acquired when the excitation is applied to different cube faces.

The simplified magnetic anisotropy characterization technique proposed in this work requires a magnetic core made of steel laminations wound with primary windings to excite the cube. A general description is shown in Figure 6.5. The cube can be inserted into a sleeve, which is wound with secondary windings and placed together in the opening of the

magnetic core. There is an airgap on each side between the cubic sample and the magnetic core. As a result, an open magnetic circuit is used for characterization.

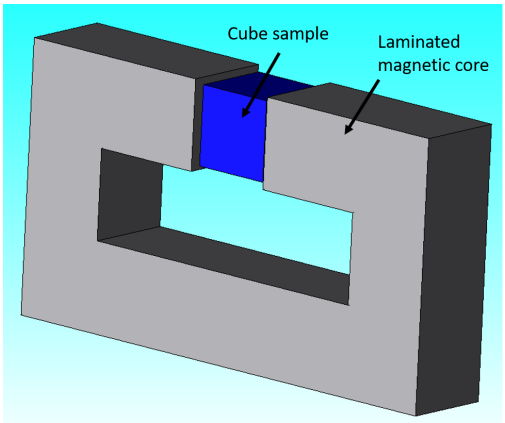

Figure 6.5: Illustration of the magnetic core used in the magnetic anisotropy characterization. The cube sample is placed in the center of the opening of the magnetic core.

The primary windings provide excitation to the test specimen. The excitation, under open loop control, is used to ensure sinusoidal voltage on the secondary windings is achieved through out the majority of the experiment. Similar to the standard AC characterization, form factor of the secondary voltage, which is the ratio between the RMS value and the average rectified value, should remain within the recommended band of 1.111±1% during the magnetic characterization.

For each direction in Figure 6.4, the corresponding magnetic induction, B, is calculated as in (6.2). Here, A is the surface area of the face of interest, N_2 is the number of turns in the secondary windings wound on the cube, f is the excitation frequency, and $|\bar{V_2}|$ is the average rectified value of the voltage picked up by the secondary windings.

$$B = \frac{|\bar{V_2}|}{4 \cdot N_2 \cdot A \cdot f} \tag{6.2}$$

The magnetic field intensity, H, of the cubic sample is calculated as in (6.3), following

the magnetic circuit model in Figure 6.6. Here, H_{ag} is the magnetic field strength in the airgap, H_{core} is the magnetic field strength in the magnetic core, l'_{ag} is the modified airgap length, l_{core} is the average length of the flux path within the magnetic core, and l_{cube} is the length of the cube sample. The calculation of l'_{ag} is the average integral of the length of the flux lines l_x between the laminated core and the cubic sample, as shown in (6.4), following the flux line model as shown in Figure 6.7. The length of the flux lines l_x accounting for the fringing flux effect follows (6.5). Additionally, N_1 is the total number of the primary windings on the magnetic core, and I is the amplitude of the excitation current.

$$H = \frac{N_1 I - 2H_{ag} l'_{ag} - H_{core} l_{core}}{l_{cube}} \tag{6.3}$$

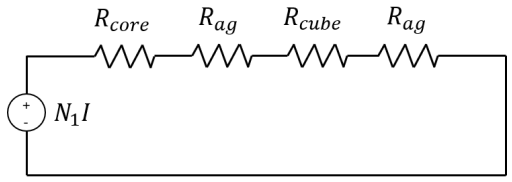

Figure 6.6: Magnetic circuit model of the anisotropy characterization. The reluctance of the magnetic core, airgap, and the cube sample are R_{core}, R_{ag}, and R_{cube}, respectively.

$$l'_{ag} = \frac{1}{l_{cube} + l_{ag}} \int_0^{l_{cube}+l_{ag}} l_x dl_x \tag{6.4}$$

$$l_x = \begin{cases} l_{ag}, \text{ min length of the flux line, between the cube and the core} \\ 0.5 l_{ag} + \frac{0.5\pi l_{ag}}{2}, \text{ max length of the flux line, accounting fringing flux} \end{cases} \tag{6.5}$$

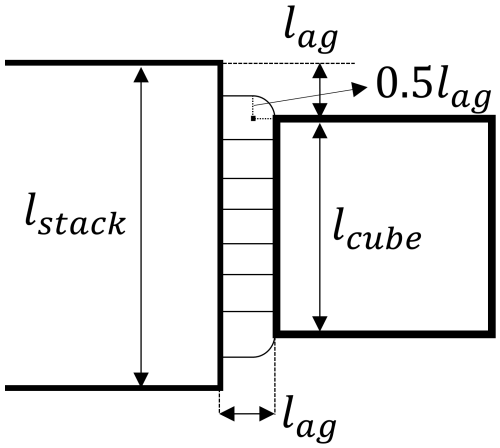

Figure 6.7: Model of the flux lines between the laminated core and the cubic sample. The cross section of the laminated core is larger than the cubic sample. The fringing flux here is modelled as a quarter of a circle.

The calculation of the magnetic field intensity, H_{ag}, in the airgap can be implemented by using a Hall effect sensor. Additionally, the calculation of magnetic field intensity, H_{core}, can be obtained by measuring the magnetic induction on the core, near the airgap. This can be implemented by applying a sense coil on the magnetic core near the opening, and then measuring the picked up voltage of the sense coil. The calculation of H_{core} is shown in (6.6).

$$H_{core} = \frac{B_{core}}{\mu_0 \mu_{core}} \tag{6.6}$$

Here, μ_0 is the vacuum permeability, B_{core} is the magnetic induction of the laminated core, μ_{core} is the relative permeability of the steel laminations used in the core, which is known. The calculation process is summarized in the flowchart shown in Figure 6.8. To measure the magnetic induction of the cubic sample in different directions, the cube is removed from the magnetic core opening, rotated and then re-inserted.

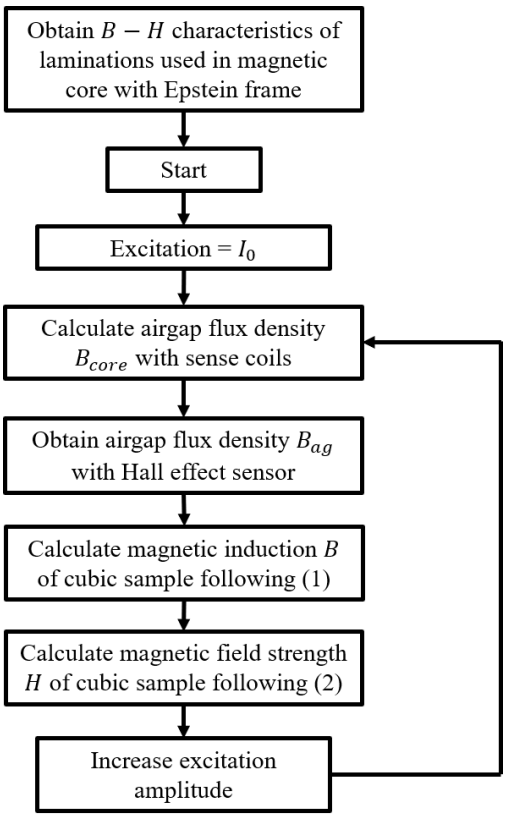

Figure 6.8: Flowchart calculation for the magnetic anisotropy characterization in each direction.

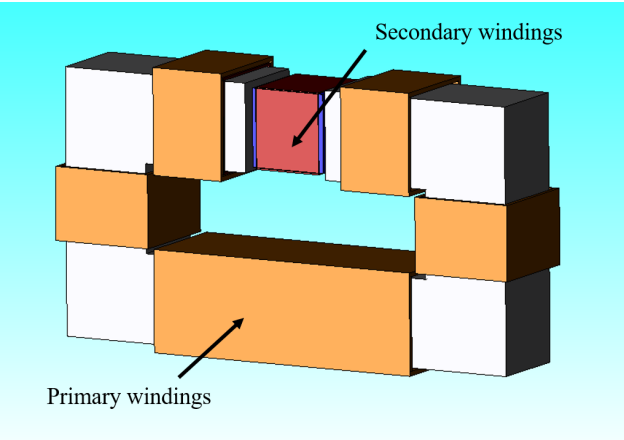

Figure 6.9: Three-dimensional finite element setup for the magnetic anisotropy characterization.

Three-dimensional finite element analysis, Figure 6.9, is used to verify the method of obtaining the magnetization curve of the cubic sample. The simulation results show that

this anisotropy test bed can be used to obtain magnetization curves under open circuit characterization. In Figure 6.10, the calculated $B-H$ curve, found via open magnetic circuit, follows the $B-H$ curve provided via closed magnetic circuit characterization.

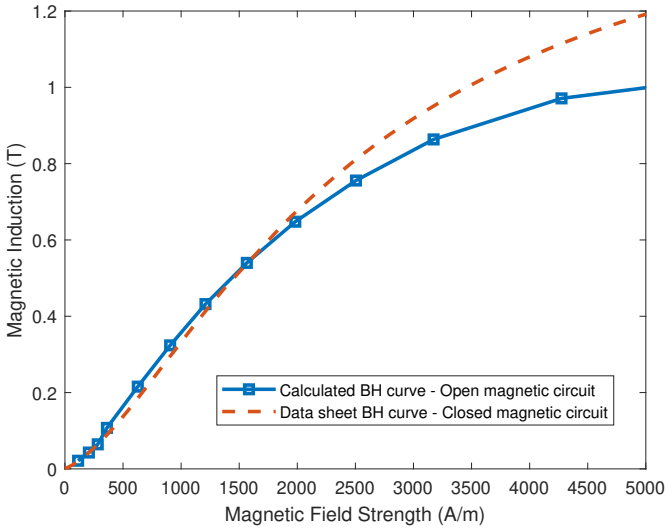

Figure 6.10: 3D FEA results of the magnetization curve obtained with the anisotropy setup. Calculated curve follows the BH curve provided by the catalog within the FEA software. Difference in the intrinsic magnetization curve and the calculated curve under open circuit characterization is shown.

The sheared magnetization curve is due to the airgap between the magnetic core and the cubic sample. A demagnetization field, H_d, occurs and opposes to the applying external magnetic field, H_e, as illustrated in Figure 6.11.

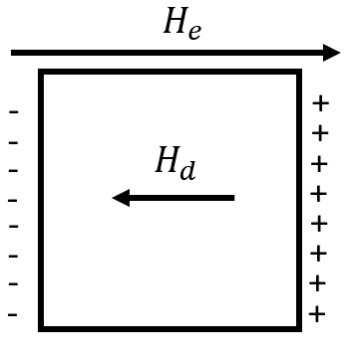

Figure 6.11: Illustration of the demagnetization effect.

This demagnetization effect is different for different shapes of the specimen, [58, 59]. As a result, for the same material, the obtained magnetic induction under open circuit characterization would be smaller than the magnetic induction obtained under close circuit characterization, especially at the same amplitude of external magnetic field strength, [28]. The larger the airgap in the open magnetic circuit, the larger the deviation between the measured curve and the intrinsic magnetization curved, or the magnetization curve obtained with closed circuit characterization. The same airgap must be used for characterization in each direction to ensure that the resulting anisotropy, if any, is not masked by variations in the airgap.

6.2.1 Anisotropy quantifier

The level of magnetic anisotropy can be quantified by the differences in the magnetic field strength required to reach the same level of magnetic induction under different excitation directions.

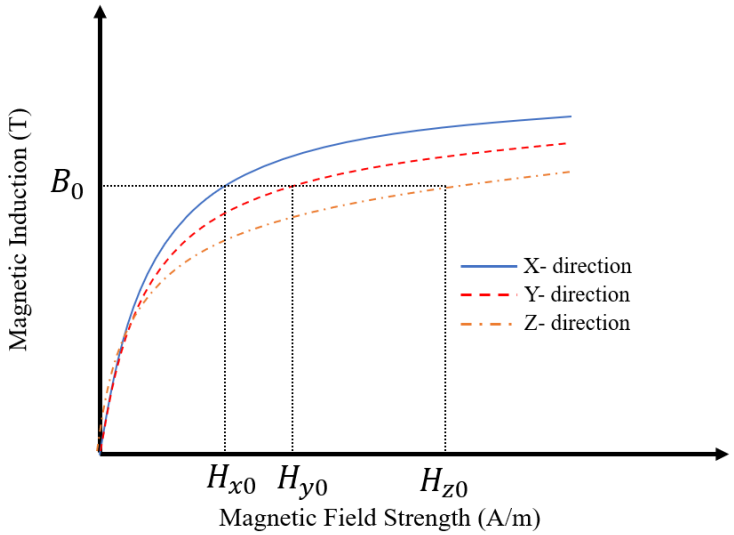

Figure 6.12: Illustration of the magnetization curves of soft magnetic materials experiencing magnetic anisotropy under excitation in X-, Y-, and Z- directions.

For a soft magnetic sample experiencing magnetic anisotropy, as illustrated in Figure 6.12, the magnetic induction B_0 is reached at different magnetic field strength for different excitation directions. These differences can be used to quantify the level of anisotropy as described in (6.7) and (6.8). Here, Δ_y is the difference in percentage between the H_{y0}, compared H_{x0}, when calculated at the same magnetic induction B_0. Similarly, Δ_z is the difference in percentage between the H_{z0}, compared H_{x0}, when calculated at the same magnetic induction B_0.

$$\Delta_y = \frac{H_{y0} - H_{x0}}{H_{x0}} \tag{6.7}$$

$$\Delta_z = \frac{H_{z0} - H_{x0}}{H_{x0}} \tag{6.8}$$

6.2.2 Experimental setup

BJP is used to prepare the cubic iron silicon sample for the magnetic anisotropy characterization. An SMC cube made of Siron®S280b is also prepared for comparison purpose with the BJP iron silicon sample. Parameters of the cube samples are shown in Table 6.1.

Table 6.1: Parameters of the cube samples.

Sample	Cube dimension	N_2
BJP cubic sample	23x23x23 mm	90
Siron®S280b cubic sample	35x35x35 mm	90

The block diagram of the magnetic anisotropy test bed is shown in Figure 6.13. Here, 50 Hz excitation is provided by the function generator, which is then amplified and fed to

the primary windings on the laminated magnetic core. The laminated magnetic core is wound with 400 turn. The current transducer is used to measure the amplitude of the excitation current. In addition, the voltage transducers are used to measure the voltages on the primary windings, the secondary windings, and the sense coils on the magnetic core, Figure 6.14. A transverse Hall effect sensor is placed in the airgap between the cube sample and the magnetic core to measure the magnetic induction in the airgap. LabVIEW data acquisition system is used to log data from the transducers and the sensor in real time.

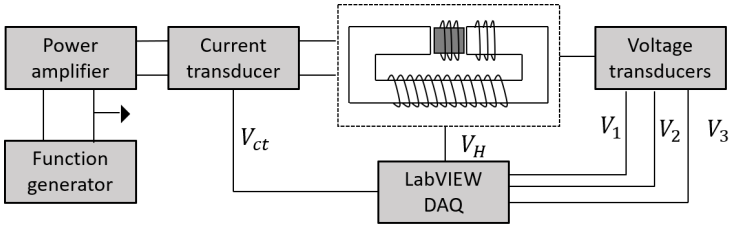

Figure 6.13: Block diagram of the magnetic anisotropy characterization. Here, V_{ct} is the voltage readings of the current transducer, V_H is the readings of the Hall effect sensor. V_1, V_2 and V_3 are the voltage readings of the primary windings, secondary windings, and the sense coils, respectively.

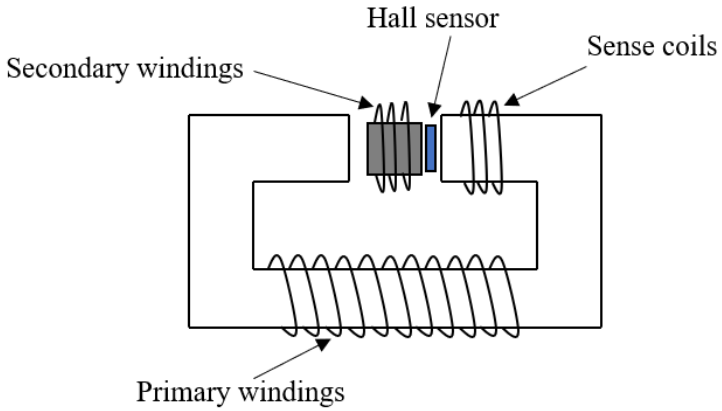

Figure 6.14: Illustration of the primary and secondary windings, sense coils, and Hall effect sensor used in the magnetic anisotropy characterization.

6.3 Results

In the SMC cubic sample, the magnetic induction versus the calculated magnetic field strength is different under all three directions. The magnetic induction in the Z- direction is lower than in the X- and Y- directions, as shown in Figure 6.15. In order to induce a magnetic induction of 0.5 T, excitation in the Z- direction requires an additional 28% in magnetic field strength compared to X- direction. Additionally, an increase of 9% in magnetic field strength in the Y- direction is required to induce 0.5 T, compared to the X- direction. Form factor of the secondary voltage for the characterization of the SMC cubic sample is maintained within the recommended values during the majority of the test, as shown in Figure 6.16.

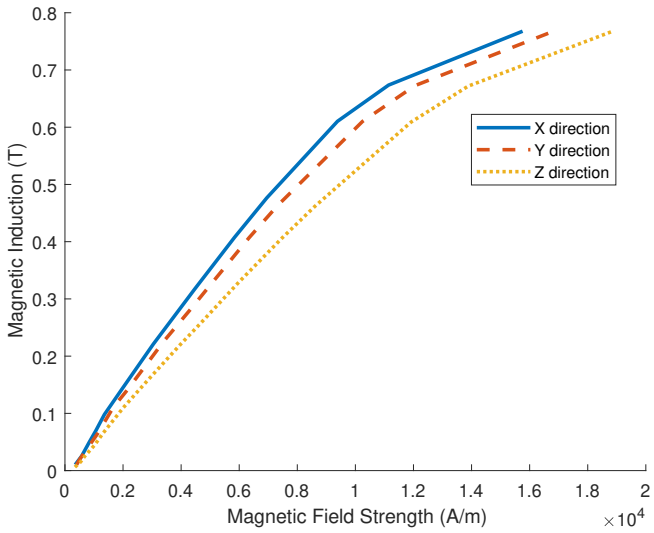

Figure 6.15: Magnetization curves of the Siron SMC cube under X-, Y-, and Z- directions. Excitation frequency is at 50 Hz. Magnetic field strength is calculated under open magnetic circuit characterization.

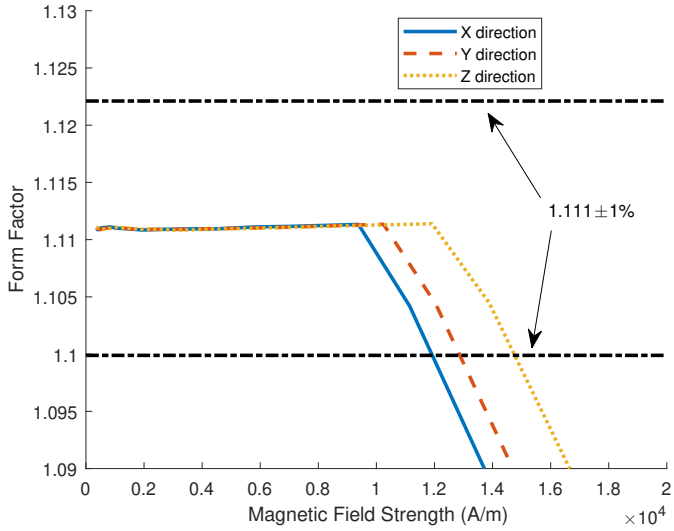

Figure 6.16: Form factor of the secondary voltage for the magnetic anisotropy characterization of the Siron SMC printed cube. Excitation frequency is at 50 Hz.

The 3D printed iron silicon cube also experiences magnetic anisotropy. The magnetic induction in the Z- direction or the build direction is lower compared to both X- and Y- directions, Figure 6.17. At magnetic induction of 0.5 T, excitation in the Z- direction would require an increase in 20% in magnetic field strength compared to the X- direction. On the other hand, the magnetic field strength in the Y- direction needs an additional 5.4% to reach an induction of 0.5 T compared to the X- direction.

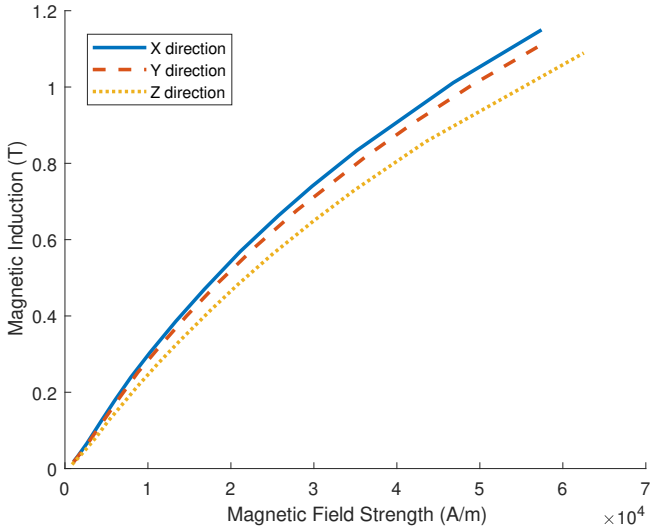

Figure 6.17: Magnetization curves of 3D printed iron silicon cube under X-, Y-, and Z-directions. Excitation frequency is at 50 Hz. Magnetic field strength is calculated under open magnetic circuit characterization.

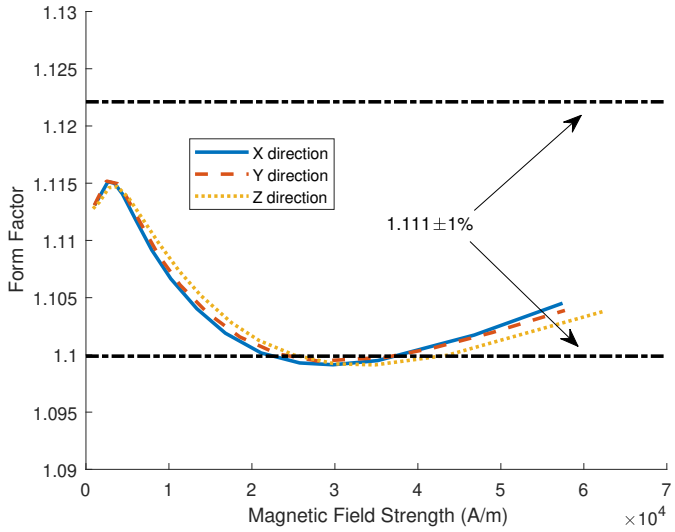

Figure 6.18: Form factor of the secondary voltage for the magnetic anisotropy characterization of the 3D printed cube. Excitation frequency is at 50 Hz.

The magnetic anisotropy for the 3D printed iron silicon increases as the magnetic induction increases. At 1.0 T, excitation in the Z- and Y- direction needs an additional 20% and 6%, respectively, to reach the same level of induction as in X- direction. Form factor of the

secondary voltage for the characterization of the printed cube is also maintained during the experiment, Figure 6.18. Table 6.2 summarizes the magnetic anisotropy quantifiers between the three directions for both the SMC cube and the 3D printed cube.

Table 6.2: Comparison of magnetic anisotropy between SMC and 3D printed iron silicon. Magnetic anisotropy quantifiers are calculated at 0.25 T, 0.5 T, 0.75 T, and 1.0 T.

Magnetic induction B_0	SMC cube		3D printed cube	
	Δ_y	Δ_z	Δ_y	Δ_z
0.25 T	9.3%	29.8%	4.6%	22%
0.5 T	9%	28%	5.4%	20%
0.75 T	7%	20.5%	6.3%	19.4%
1.0 T	N/A	N/A	6%	20%

Chapter 7

Conclusion and Future Work

The airgap flux density in electrical machine is typically manipulated via geometry shaping of the iron core to reach required performance. As the iron core is subjected to a rotating and non-uniform magnetic field, the use of non-homogeneous, multi-permeability iron core opens up an alternative approach in manipulating the airgap flux density behavior. With advancements in AM, it is possible to fabricate non-homogeneous, multi-permeability core which can lead to non-traditional methods in changing the airgap flux. Exploitation of non-homogeneous, multi-permeability iron core for electrical machine applications benefits from a model with low computational cost, compared to FEA. In this work, a multi-permeability modelling technique for the iron core is developed based on MEC. It is used in lieu of FEA to explore the feasibility of a multi-permeability core in shaping the airgap flux density in electrical machine.

The modelling technique allows for the variation of relative permeability in the iron core, which is no longer assumed infinite. This technique requires the discretization of the entire machine geometry into sub-regions/ cells, and the calculation of the cell-dependent winding MMF. Each cell in the iron core is then assigned with a relative permeability, which is allowed to vary. The airgap flux density can then be estimated based on the calculated reluctance elements and the discretized excitation. The resulting multi-permeability modelling technique is applied on a simple 6-slot/ 2-pole SynRM. The estimated airgap flux densities

in both radial and circumferential directions are verified with FEA, for homogeneous and non-homogeneous, multi-permeability iron cores.

The capability of multi-capability core in shaping the airgap flux density is then demonstrated by coupling the multi-permeability model and an evolutionary multi-objective optimization algorithm. The generated non-homogeneous, multi-permeability iron core can modify a specific spatial harmonic order of the airgap flux density, which can either be related to the torque or the torque ripple. Different multi-permeability distribution pattern in the iron core can lead to different variation in the airgap flux density harmonic orders; the generation of such pattern depends on the definition of the optimization problem.

With the potential of a multi-permeability iron core, and the possibility of using AM for fabricating such a core, an initial demonstration of AM in fabricating iron cores with variable levels of relative permeability is necessary. Here, the experimental characterization results of 3D-printed iron cores from two different AM methods, BJP and FFF, show that it is possible to achieve different levels of maximum relative permeability from nearly 1 up to 6000.

AM is a layer-based manufacturing technique. In contrast to subtractive and powder metallurgy manufacturing, AM fabricates individual layer on top of another. Thus, printed iron cores can be subjected to magnetic anisotropy, especially in the build direction or the direction of layer deposition. Magnetic anisotropy characterization of additively manufactured iron cores is thus important, since it helps AM researchers in quantifying the magnetic anisotropy levels. In this work, a simplified magnetic anisotropy characterization test bed that is capable of extracting the $B - H$ magnetization curve of soft magnetic materials is developed. In contrast to other magnetic characterization setups, this test bed requires a magnetic C core, a single Hall effect sensor, and a cubic specimen. The experimental results

from this test bed confirm that BJP iron core can reach similar magnetic anisotropy level as seen in SMC.

Future work includes the demonstration on the manipulation of the airgap flux density via non-homogeneous, multi-permeability rotor core in three dimensions, as illustrated in Figure 7.1. The developed model shows the capability in changing the airgap flux density in a 2D problem. With continuous advancements in AM and multi-material printing, it is possible to deposit material with different relative permeability in the build direction. Thus, the concept of non-homogeneous, multi-permeability iron core can be expanded in the axial direction of a rotating radial machine. This requires the development of the multi-permeability modelling technique that can account for the $\hat{z}$ direction as shown in Figure 7.2.

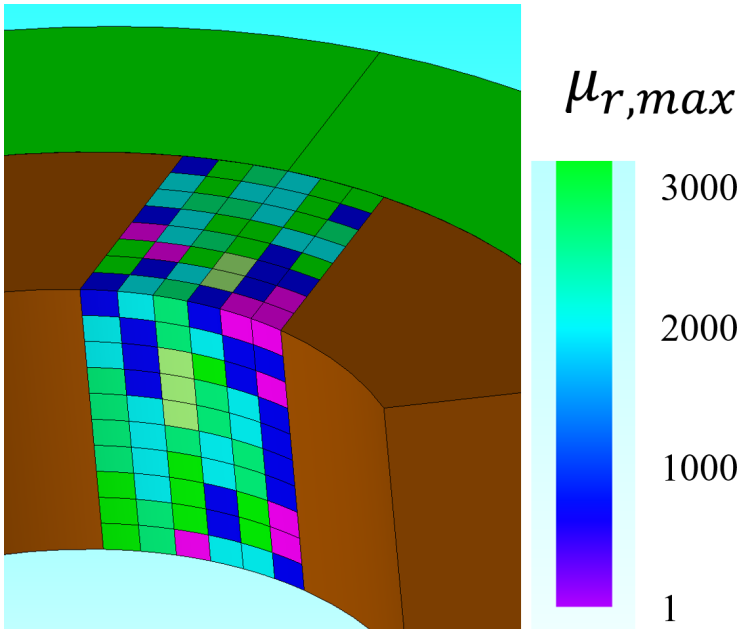

Figure 7.1: Illustration on a 3D multi-permeability iron core. The addition of permeability distribution in the stacking direction adds an additional degree of freedom in the designs space.

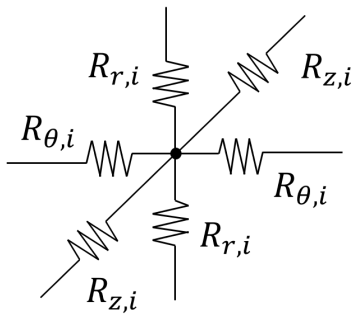

Figure 7.2: Illustration on a node representing reluctance elements for a 3D problem. This node can represent a single sub-region/ cell in the iron core of an electrical machine. Here, $R_{z,i}$ represents the reluctance in the $\hat{z}$ direction of cell i.

Future work also includes additional analysis on improving the modelling technique, especially on the design space. Here, three questions are posed: (1) What should be the optimal size of the cells for the discretization process? (2) What region in the iron core has higher impact in manipulating the airgap flux density and subsequently, the torque characteristics of the machine? and (3) What should be the variation of relative permeability within the iron core. For each question, a design of experiment (DOE) should be created, the multi-permeability MEC model is then calculated, and an optimization algorithm is run to evaluate the output objective space. The DOE can then be used to determine the choice for the cell size (question 1), the region (question 2), and the $\mu_{r,max}$ variation (question 3) by implementing analysis of variance on the objective space. Figure 7.3 shows a possible framework in answering the 3 questions.

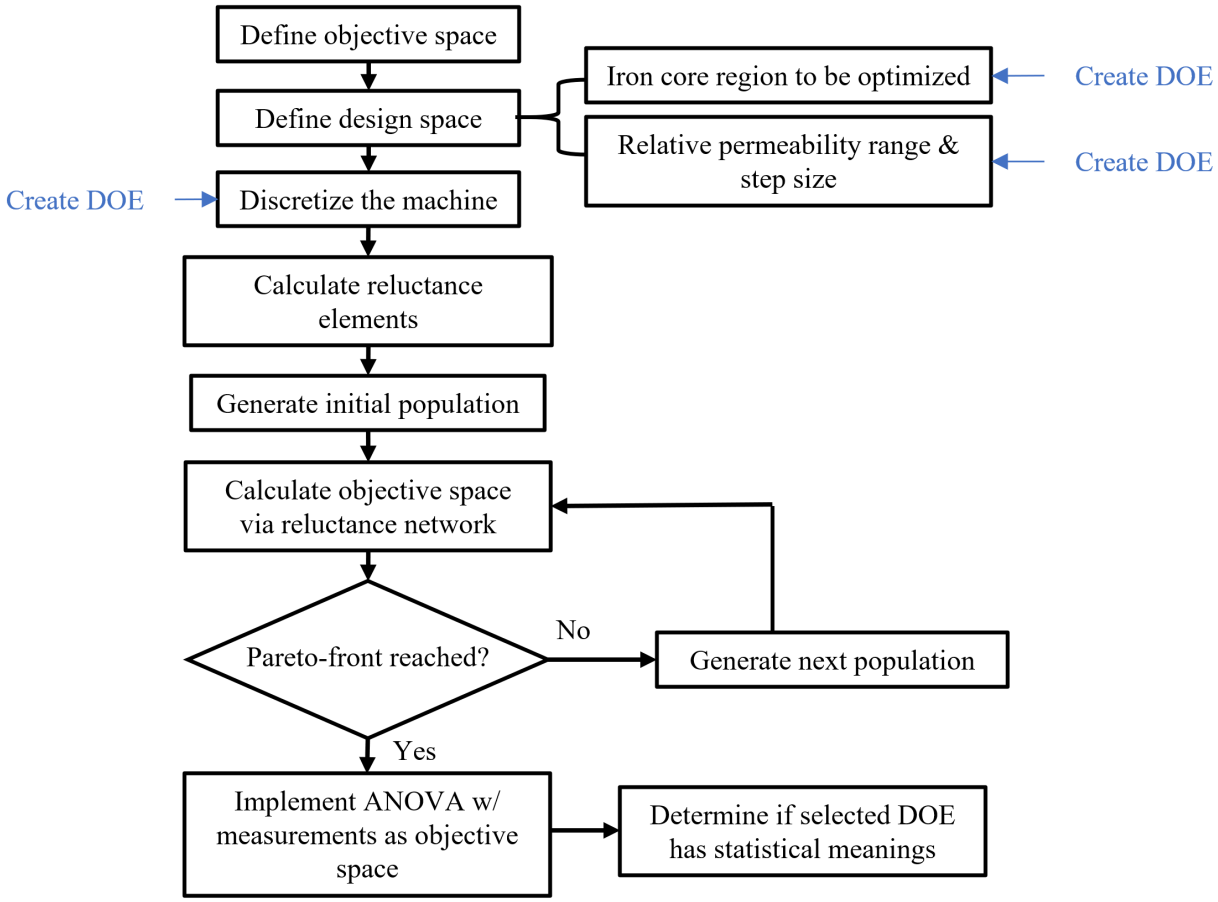

Figure 7.3: Framework for determining the design space for a multi-permeability optimization problem for the iron core.

Additional future work includes numerical demonstrating the manipulation of the airgap flux density via non-homogeneous, multi-permeability rotor core. A multi-permeability rotor core provides extra degrees of freedom in manipulating the airgap flux density. However, as the saliency of the rotor core changes due to introduction of different sub-regions with different levels of relative permeability, the control angle of the excitation current needs to be modified so that optimal torque is achieved. The multi-permeability modelling technique needs to account for variable levels of saliency in the rotor core and be linked with the motor control scheme.

APPENDICES

Appendix A

Customized finite element

The FEA tool here is developed based on Galerkin approach, a special scenario of the method of weighted residuals. Considering a first order triangular element with coordinates (x_i, y_i), (x_j, y_j), and (x_k, y_k) as shown in Figure A.1, the vector potentials at the three nodes are unknown and will be calculated. Assuming that the vector potential linearly varies within the element, the flux density in the element would then be constant, [60]. The relationship between the node vector potential approximates, $\hat{A}_i, \hat{A}_j, \hat{A}_k$ and the coordinates of the element are calculated as in (A.1). The constants C_1, C_2, C_3 can then be solved via Cramer's rule as shown in (A.2), (A.3), and (A.4). The area of the triangular element is designated as Δ.

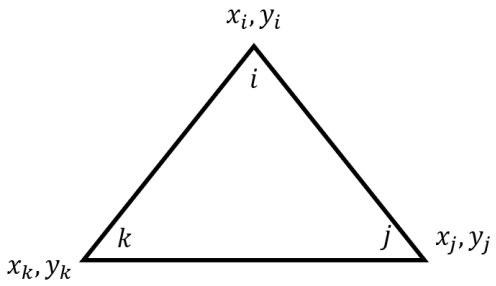

Figure A.1: Illustration of first order triangular element.

For a 2D problem, the relationship between the applied current density J_0 and the magnetic vector potentials is shown in (A.5). Here σ is the conductivity of the medium and w is the angular frequency. Introducing an operator $\mathcal{L}(x) = 0$ on a region Ω with boundary

condition C, its approximation is then shown in (A.6) with R is the residual since $\hat{x}$ is an approximation of x, [60].

$$\begin{aligned} \hat{A}_i &= C_1 + C_2 x_i + C_3 y_i \\ \hat{A}_j &= C_1 + C_2 x_j + C_3 y_j \\ \hat{A}_k &= C_1 + C_2 x_k + C_3 y_k \end{aligned} \tag{A.1}$$

$$C_1 = \frac{\begin{vmatrix} \hat{A}_i & x_i & y_i \\ \hat{A}_j & x_j & y_j \\ \hat{A}_k & x_k & y_k \end{vmatrix}}{2\Delta} \tag{A.2}$$

$$C_2 = \frac{\begin{vmatrix} 1 & \hat{A}_i & y_i \\ 1 & \hat{A}_j & y_j \\ 1 & \hat{A}_k & y_k \end{vmatrix}}{2\Delta} \tag{A.3}$$

$$C_3 = \frac{\begin{vmatrix} 1 & x_i & \hat{A}_i \\ 1 & x_j & \hat{A}_j \\ 1 & x_k & \hat{A}_k \end{vmatrix}}{2\Delta} \tag{A.4}$$

The Galerkin approach states that the integral of the projection of the residual on a weighting function, W, is zero over the domain Ω. In other words, for a domain Ω in 2D,

the integral between R and W is shown in (A.7). Approximating the magnetic potential A with $\hat{A}$, then (A.5) becomes (A.8). Applying (A.7) onto (A.8), we then achieve (A.9).

$$\frac{1}{\mu_r \mu_0}\frac{\partial^2 A}{\partial x^2} + \frac{1}{\mu_r \mu_0}\frac{\partial^2 A}{\partial x^2} = -J_0 + jw\sigma A \tag{A.5}$$

$$\mathcal{L}(\hat{x}) = R \tag{A.6}$$

$$\int_\Omega RW dxdy = 0 \tag{A.7}$$

$$\frac{1}{\mu_r \mu_0}\frac{\partial^2 \hat{A}}{\partial x^2} + \frac{1}{\mu_r \mu_0}\frac{\partial^2 \hat{A}}{\partial x^2} + J_0 - jw\sigma\hat{A} = R \tag{A.8}$$

$$\iint_\Omega W\Big(\frac{1}{\mu_r \mu_0}\frac{\partial^2 \hat{A}}{\partial x^2} + \frac{1}{\mu_r \mu_0}\frac{\partial^2 \hat{A}}{\partial x^2}\Big)dxdy + \iint_\Omega W J_0 dxdy - jw\sigma \iint_\Omega W\hat{A}dxdy = 0 \tag{A.9}$$

Integration by part is then applied to the first term of (A.9). This results in (A.10), where $\hat{n}$ is the normal unit vector to the boundary C. The surface integral in (A.10) can be then approximated as sum of small and numerous surface integrals.

Given the domain Ω meshed with M number of triangular elements, then the approximation of the surface integral becomes (A.11), where W^e is the weighting function, μ^e is the permeability, and $\hat{A}^e$ is the vector potential approximate of a single element, respectively. Here, each element is within the domain Ω^e.

The approximate vector potential at any coordinate (x, y) within an element is calculated

as in (A.12).

$$\iint_{\Omega} \frac{1}{\mu_r \mu_0}\Big(\frac{\partial W}{\partial x}\frac{\partial \hat{A}}{\partial x} + \frac{\partial W}{\partial y}\frac{\partial \hat{A}}{\partial y}\Big)dxdy - \int_{C} \frac{1}{\mu_r \mu_0} W \frac{\partial \hat{A}}{\partial \hat{n}} dC \tag{A.10}$$

$$\sum_{M}\left(\frac{1}{\mu^e}\iint_{\Omega^e}\Big(\frac{\partial W^e}{\partial x}\frac{\partial \hat{A}^e}{\partial x} + \frac{\partial W^e}{\partial y}\frac{\partial \hat{A}^e}{\partial y}\Big)dxdy\right) \tag{A.11}$$

From (A.1), (A.2), (A.3), and (A.4), (A.12) becomes (A.13). Applying the weighting function W^e to be the same as the shape functions (N_i^e, N_j^e, N_k^e), [60], the surface integral for each element in (A.11) becomes (A.14). The second term of (A.9) for an element is then shown in (A.15), assuming that the applied current density is constant over the element. The third term in (A.9) is also shown in (A.16), following the application of the weighting function.

$$\hat{A}^e = C_1 + C_2 x + C_3 y \tag{A.12}$$

$$\hat{A}^e = (N_i^e, N_j^e, N_k^e)\begin{pmatrix} \hat{A}_i^e \\ \hat{A}_j^e \\ \hat{A}_k^e \end{pmatrix} \tag{A.13}$$

$$\frac{1}{\mu^e}\iint_{\Omega^e}\Big(\frac{\partial W^e}{\partial x}\frac{\partial \hat{A}^e}{\partial x}+\frac{\partial W^e}{\partial y}\frac{\partial \hat{A}^e}{\partial y}\Big)dxdy = \frac{1}{4\mu^e\Delta}\begin{pmatrix} b_i^2+c_i^2 & b_ib_j+c_ic_j & b_ib_k+c_ic_k \\ b_ib_j+c_ic_j & b_j^2+c_j^2 & b_jb_k+c_jc_k \\ b_ib_k+c_ic_k & b_jb_k+c_jc_k & b_k^2+c_k^2 \end{pmatrix}\begin{pmatrix} \hat{A}_i^e \\ \hat{A}_j^e \\ \hat{A}_k^e \end{pmatrix} \tag{A.14}$$

Upon defining two local matrices for each element as in (A.17) and (A.18), the solving of

(A.9) in static magnetic analysis becomes (A.19). The process of solving all of the unknowns in $\hat{A}$ involves solving the matrix problem in (A.19).

$$J_0^e \iint_{\Omega^e} W^e dxdy = \frac{J_0^e \Delta}{3} \begin{pmatrix} 1 \\ 1 \\ 1 \end{pmatrix} \tag{A.15}$$

$$\begin{aligned} -jw\sigma^e \iint_{\Omega^e} W^e \hat{A}^e dxdy &= -jw\sigma^e \iint_{\Omega^e} \begin{pmatrix} N_i^e \\ N_j^e \\ N_k^e \end{pmatrix} \begin{pmatrix} N_i^e & N_j^e & N_k^e \end{pmatrix} \begin{pmatrix} \hat{A}_i^e \\ \hat{A}_j^e \\ \hat{A}_k^e \end{pmatrix} dxdy \\ &= -\frac{jw\sigma^e \Delta}{12} \begin{pmatrix} 2 & 1 & 1 \\ 1 & 2 & 1 \\ 1 & 1 & 2 \end{pmatrix} \begin{pmatrix} \hat{A}_i^e \\ \hat{A}_j^e \\ \hat{A}_k^e \end{pmatrix} \end{aligned} \tag{A.16}$$

This includes three steps: 1) for each element, solve for the local matrices P_L and Q_L, 2) placing the local matrices into the global matrices P_G and Q_G, and 3) solve the linear algebra problem $P_G \hat{A} = -Q_G$.

$$P_L^e = \frac{1}{4\mu^e \Delta} \begin{pmatrix} b_i^2 + c_i^2 & b_i b_j + c_i c_j & b_i b_k + c_i c_k \\ b_i b_j + c_i c_j & b_j^2 + c_j^2 & b_j b_k + c_j c_k \\ b_i b_k + c_i c_k & b_j b_k + c_j c_k & b_k^2 + c_k^2 \end{pmatrix} \tag{A.17}$$

The placement of local matrices into the global matrix can be described in [60]. The customized finite element tool in this work assigns two back to back triangular elements into a single sub-region, as shown in Figure A.2. Within this sub-region, the relative permeability

of the two elements are the same.

$$Q_L^e = \frac{J_0^e \Delta}{3} \begin{pmatrix} 1 \\ 1 \\ 1 \end{pmatrix} \tag{A.18}$$

$$\sum_M \left(\hat{A^e}^T P_L \hat{A^e} + \hat{A^e}^T Q_L \right) = 0 \tag{A.19}$$

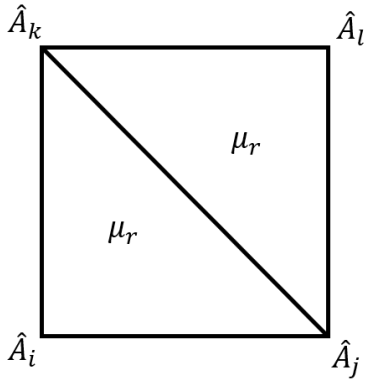

Figure A.2: Illustration of a sub-region made of two elements sharing the same relative permeability.

Figure A.3 shows the flowchart of the FEA algorithm used in this work. For the domain Ω under interest, the triangular mesh is applied for the entire domain. The domain is then divided into sub-regions, where each region takes a value of relative permeability. Upon completion of assigning permeability, each node within the meshed domain is an unknown magnetic potential. The algorithm calculates the local matrices following (A.17) and (A.18) for each element within the domain Ω. After calculation for each element is completed, the algorithm places the local matrices within the global matrices. The algorithm then can find the magnetic potentials at all nodes within domain Ω by solving $P_G \hat{A} = Q_G$.

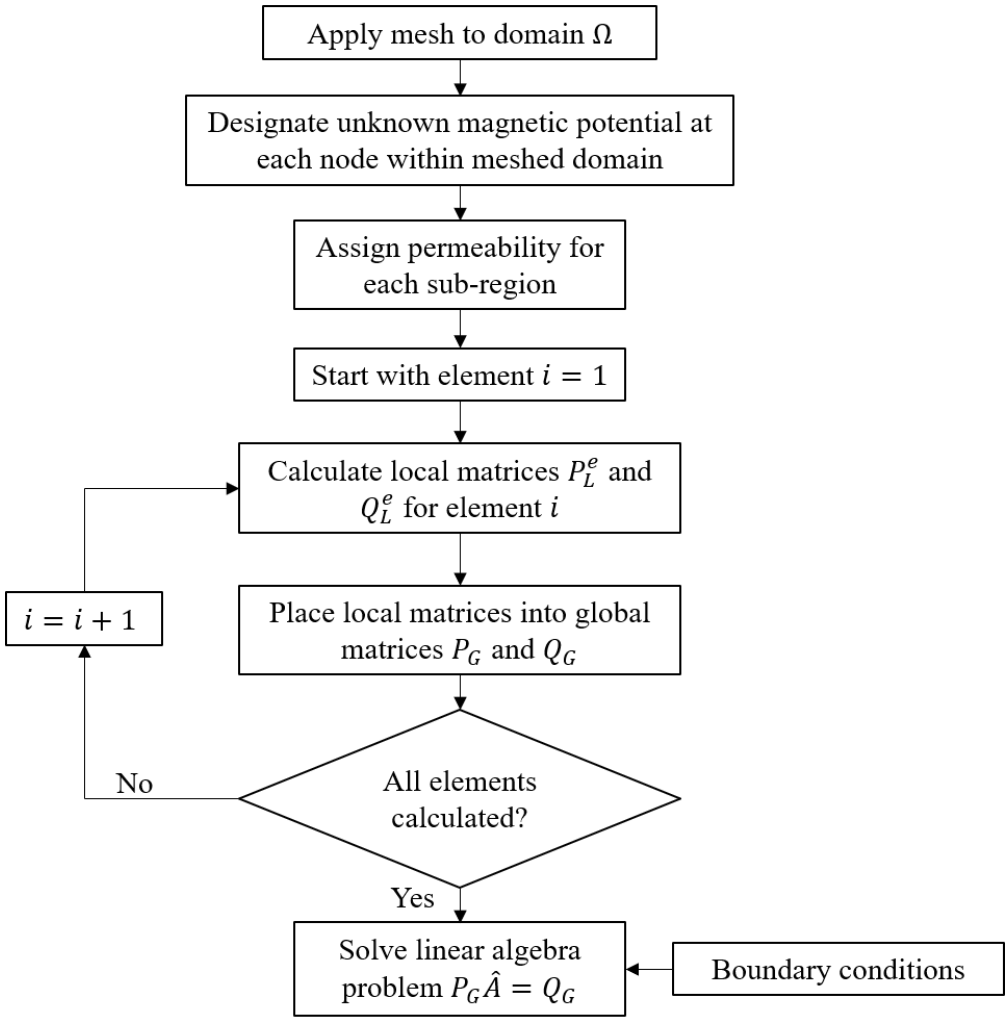

Figure A.3: Flowchart on development of the customized finite element algorithm.

Appendix B

Additional magnetic properties - 3D printed iron silicon

The quasi-static magnetic properties of BJP samples in Table 5.4 is shown in Table B.1. The intrinsic coercivity of printed iron silicon here is less than 1/3 of the typical H_c values seen in SMCs. It is also worth noting that the magnetic induction at 10 kA/m of BJP iron silicon samples is around 1.5 T, which is similar to typical values seen in SMCs. At low magnetic field strength, around 500 A/m, the magnetic induction of BJP iron silicon is significantly higher in comparison to commercial SMCs.

Specific loss density of BJP iron silicon is comparable to commercial SMCs at low excitation frequency, as shown in Figure B.1. At higher excitation frequency, the specific loss density of BJP iron silicon at this moment is higher than commercial SMCs, as shown in Figures B.2 and B.3.

Table B.1: Summary of experimental quasi-static magnetic characteristics of BJP samples.

Sample composition	Boron addition (wt%)	Sintering temperature (°C)	Intrinsic coercivity (A/m)	$\hat{B}$ @ 500 A/m (T)	$\hat{B}$ @ 10 kA/m (T)
$Fe_{97}Si_3$	0.00	1200	103.4	1.08	1.45
$Fe_{97}Si_3$	0.25	1200	88.4	0.85	1.46
$Fe_{95}Si_5$	0.00	1200	89.4	1.03	1.42
$Fe_{95}Si_5$	0.25	1200	69.6	1.01	1.53
$Fe_{97}Si_3$	0.00	1250	102.4	1.09	1.50
$Fe_{97}Si_3$	0.25	1250	89.2	0.83	1.43
$Fe_{95}Si_5$	0.00	1250	88.2	1.03	1.44
$Fe_{95}Si_5$	0.25	1250	75.7	0.95	1.45

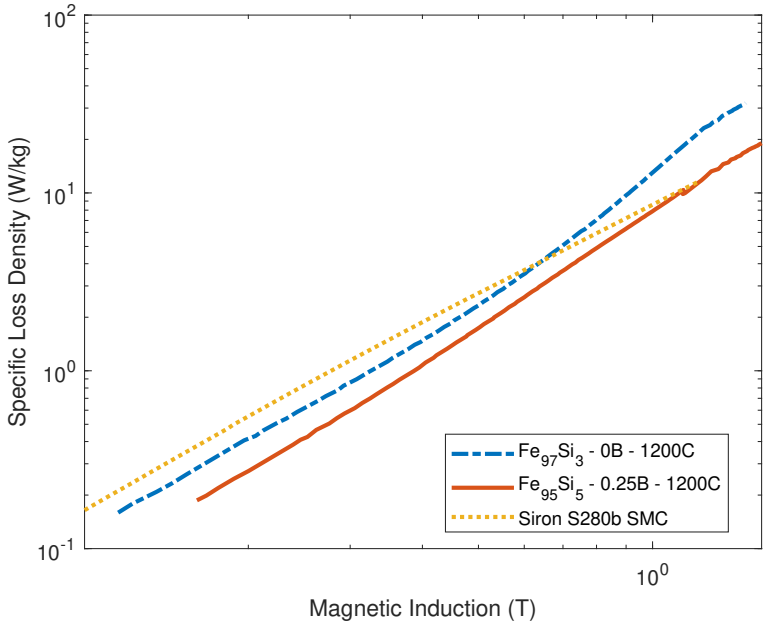

Figure B.1: Experimental specific loss density of BJP samples and SMC sample at 50 Hz.

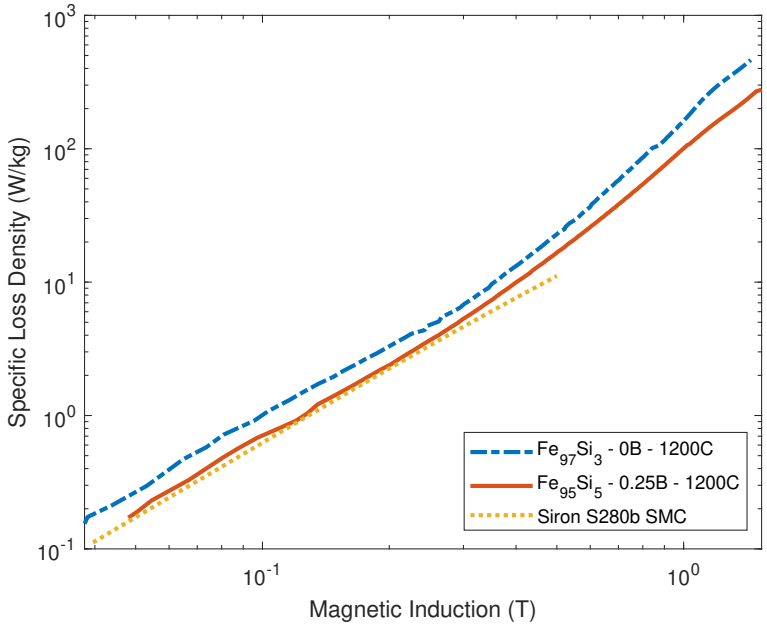

Figure B.2: Experimental specific loss density of BJP samples and SMC sample at 200 Hz.

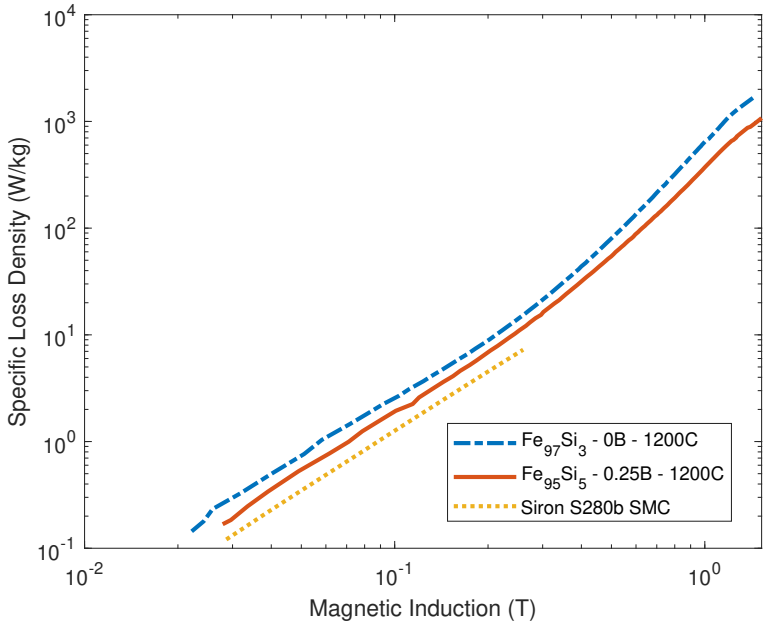

Figure B.3: Experimental specific loss density of BJP samples and SMC sample at 400 Hz.

BIBLIOGRAPHY

BIBLIOGRAPHY

[1] "Electric machines advanced manufacturing," https://www.energy.gov/eere/amo/electric-machines,, Department of Energy.

[2] A. Krings, A. Boglietti, A. Cavagnino, and S. Sprague, "Soft magnetic material status and trends in electric machines," *IEEE Transactions on Industrial Electronics*, vol. 64, no. 3, pp. 2405–2414, March 2017.

[3] J. Pyrhonen, T. Jokinen, and V. Hrabovcova, *Design of Rotating Electrical Machines*. John Wiley & Sons, Ltd, 2008.

[4] Y. Ishikura, J. Imaoka, M. Noah, and M. Yamamoto, "Improved core loss calculation method considering the non-uniform distribution of magnetic flux density in powder cores," *IET Power Electronics*, vol. 12, pp. 1393–1399(6), May 2019.

[5] A. Aggarwal, E. G. Strangas, and A. Karlis, "Review of segmented stator and rotor designs for ac electric machines," in *2020 International Conference on Electrical Machines (ICEM)*, vol. 1, 2020, pp. 2342–2348.

[6] D. N. Dyck and D. A. Lowther, "Automated design of magnetic devices by optimizing material distribution," *IEEE Transactions on Magnetics*, vol. 32, no. 3, pp. 1188–1193, 1996.

[7] L. Wang, Z. Hu, Y. Liu, Y. Pei, and X. Yang, "Multipermeability inductors for increasing the inductance and improving the efficiency of high-frequency dc/dc converters," *IEEE Transactions on Power Electronics*, vol. 28, no. 9, pp. 4402–4413, 2013.

[8] J. Ma, J. Li, H. Fang, Z. Li, Z. Liang, Z. Fu, L. Xiao, and R. Qu, "Optimal design of an axial-flux switched reluctance motor with grain-oriented electrical steel," *IEEE Transactions on Industry Applications*, vol. 53, no. 6, pp. 5327–5337, 2017.

[9] S. Takeda, K. Fujitani, S. Odawara, and K. Fujisaki, "Trial manufacture of magnetic anisotropic motor and evaluation of drag loss characteristics," in *2014 International Conference on Electrical Machines (ICEM)*, 2014, pp. 2055–2061.

[10] A. M. EL-Refaie, "High speed operation of permanent magnet machines," Ph.D. dissertation, University of Wisconsin - Madison, Madison, WI, USA, September 2005.

[11] S. Galioto and A. El-refaie, "Electric machine stator lamination with dual phase magnetic material," US Patent 10,396,615, 2019.

[12] P. B. Reddy, A. M. El-Refaie, M. Zou, D. Pan, J. P. Alexander, N. Tapadia, K. Grace, K.-K. Huh, and F. Johnson, "Performance testing and analysis of synchronous reluctance motor utilizing dual-phase magnetic material," *IEEE Transactions on Industry Applications*, vol. 54, no. 3, pp. 2193–2201, 2018.

[13] C. McGarry, A. McDonald, and N. Alotaibi, "Optimisation of additively manufactured permanent magnets for wind turbine generators," in *2019 IEEE International Electric Machines Drives Conference (IEMDC)*, 2019, pp. 656–663.

[14] N. Simpson and P. H. Mellor, "Additive manufacturing of shaped profile windings for minimal ac loss in gapped inductors," in *2017 IEEE International Electric Machines and Drives Conference (IEMDC)*, May 2017, pp. 1–7.

[15] F. Lorenz, J. Rudolph, and R. Wemer, "Design of 3d printed high performance windings for switched reluctance machines," in *2018 XIII International Conference on Electrical Machines (ICEM)*, Sep. 2018, pp. 2451–2457.

[16] W. Sixel, M. Liu, G. Nellis, and B. Sarlioglu, "Cooling of windings in electric machines via 3d printed heat exchanger," in *2018 IEEE Energy Conversion Congress and Exposition (ECCE)*, Sep. 2018, pp. 229–235.

[17] M. P. Paranthaman, C. S. Shafer, A. M. Elliott, D. H. Siddel, M. A. McGuire, R. M. Springfield, J. Martin, R. Fredette, and J. Ormerod, "Binder jetting: A novel ndfeb bonded magnet fabrication process," *JOM*, vol. 68, no. 4, p. 1978–1982, July 2016.

[18] M. Lindner and R. Werner, "Hysteresis-model oriented test procedure for soft-magnetic properties of printed or laminated toroids," in *2014 4th International Electric Drives Production Conference (EDPC)*, Sep. 2014, pp. 1–8.

[19] D. Goll, D. Schuller, G. Martinek, T. Kunert, J. Schurr, C. Sinz, T. Schubert, T. Bernthaler, H. Riegel, and G. Schneider, "Additive manufacturing of soft magnetic materials and components," *Additive Manufacturing*, vol. 27, pp. 428 – 439, 2019.

[20] L. Liu, C. Ding, S. Lu, T. Ge, Y. Yan, Y. Mei, K. D. T. Ngo, and G. Q. Lu, "Design and additive manufacturing of multi-permeability magnetic cores," in *2017 IEEE Energy Conversion Congress and Exposition (ECCE)*, Oct 2017, pp. 881–886.

[21] TUChemnitz, "3d-multimaterialdruck," https://www.tu-chemnitz.de/etit/ema/AMMM/index.php,.

[22] F. S. Freeman, A. Lincoln, J. Sharp, A. Lambourne, and I. Todd, "Exploiting thermal strain to achieve an in-situ magnetically graded material," *Materials & Design*, vol. 161, pp. 14–21, 2019. [Online]. Available: https://www.sciencedirect.com/science/article/pii/S0264127518308189

[23] A. Krings, M. Cossale, A. Tenconi, J. Soulard, A. Cavagnino, and A. Boglietti, "Characteristics comparison and selection guide for magnetic materials used in electrical machines," in *2015 IEEE International Electric Machines Drives Conference (IEMDC)*, May 2015, pp. 1152–1157.

[24] S. S. Maroufian, "Winding function modeling of synchronous reluctance machines," Ph.D. dissertation, Concordia University, Montreal, Quebec, Canada, October 2018.

[25] A. R. Tariq, "Design, analysis, and operation of ipmsms for hev applications," Ph.D. dissertation, Michigan State University, East Lansing, Michigan, USA, October 2010.

[26] J. Perho, "Reluctance network for analysing induction machines," Ph.D. dissertation, Helsinki University of Technology, Helsinki, Finland, December 2002.

[27] C. B. Rasmussen and E. Ritchie, "A magnetic equivalent circuit approach for predicting pm motor performance," in *IAS '97. Conference Record of the 1997 IEEE Industry Applications Conference Thirty-Second IAS Annual Meeting*, vol. 1, 1997, pp. 10–17 vol.1.

[28] R. Hilzinger and W. Rodewald, *Magnetic Materials*. Wiley, 2013. [Online]. Available: https://books.google.at/books?id=uAiquAAACAAJ

[29] G. Bertotti, "Some considerations on the physical interpretation of eddy current losses in ferromagnetic materials," *Journal of Magnetism and Magnetic Materials*, vol. 54-57, pp. 1556 – 1560, 1986. [Online]. Available: http://www.sciencedirect.com/science/article/pii/0304885386909261

[30] A. B. Kustas, D. F. Susan, K. L. Johnson, S. R. Whetten, M. A. Rodriguez, D. J. Dagel, J. R. Michael, D. M. Keicher, and N. Argibay, "Characterization of the fe-co-1.5v soft ferromagnetic alloy processed by laser engineered net shaping (lens)," *Additive Manufacturing*, vol. 21, pp. 41 – 52, 2018. [Online]. Available: http://www.sciencedirect.com/science/article/pii/S2214860417306103

[31] M. Khajepour and S. Sharafi, "Characterization of nanostructured fe–co–si powder alloy," *Powder Technology*, vol. 232, pp. 124 – 133, 2012. [Online]. Available: http://www.sciencedirect.com/science/article/pii/S0032591012005335

[32] J. Geng, I. C. Nlebedim, M. F. Besser, E. Simsek, and R. T. Ott, "Bulk combinatorial synthesis and high throughput characterization for rapid assessment of magnetic materials: Application of laser engineered net shaping (lens™)," *JOM*, vol. 68, no. 7, pp. 1972–1977, Jul 2016. [Online]. Available: https://doi.org/10.1007/s11837-016-1918-x

[33] Vacuumschmelze, *Soft Magnetic Materials and Semi-finished Products*, https://vacuumschmelze.com/shared/quickNav/Downloads, Vacuumschmelze, 2002.

[34] C. Mikler, V. Chaudhary, T. Borkar, V. Soni, D. Choudhuri, R. Ramanujan, and R. Banerjee, "Laser additive processing of ni-fe-v and ni-fe-mo permalloys: Microstructure and magnetic properties," *Materials Letters*, vol. 192, pp. 9 – 11, 2017.

[35] B. Zhang, N.-E. Fenineche, H. Liao, and C. Coddet, "Magnetic properties of in-situ synthesized feni3 by selective laser melting fe-80%ni powders," *Journal of Magnetism and Magnetic Materials*, vol. 336, pp. 49 – 54, 2013.

[36] C. Mikler, V. Chaudhary, V. Soni, B. Gwalani, R. Ramanujan, and R. Banerjee, "Tuning the phase stability and magnetic properties of laser additively processed fe-30at%ni soft magnetic alloys," *Materials Letters*, vol. 199, pp. 88 – 92, 2017.

[37] J. Wang, M. West, D. Howe, H. Z. D. L. Parra, and W. M. Arshad, "Design and experimental verification of a linear permanent magnet generator for a free-piston energy converter," *IEEE Transactions on Energy Conversion*, vol. 22, no. 2, pp. 299–306, June 2007.

[38] B. Zhang, N.-E. Fenineche, H. Liao, and C. Coddet, "Microstructure and magnetic properties of fe–ni alloy fabricated by selective laser melting fe/ni mixed powders," *Journal of Materials Science & Technology*, vol. 29, no. 8, pp. 757 – 760, 2013.

[39] B. Zhang, N.-E. Fenineche, L. Zhu, H. Liao, and C. Coddet, "Studies of magnetic properties of permalloy (fe–30%ni) prepared by slm technology," *Journal of Magnetism and Magnetic Materials*, vol. 324, no. 4, pp. 495 – 500, 2012.

[40] I. Shishkovsky and V. Saphronov, "Peculiarities of selective laser melting process for permalloy powder," *Materials Letters*, vol. 171, pp. 208 – 211, 2016. [Online]. Available: http://www.sciencedirect.com/science/article/pii/S0167577X16302567

[41] M. Garibaldi, I. Ashcroft, N. Hillier, S. Harmon, and R. Hague, "Relationship between laser energy input, microstructures and magnetic properties of selective laser melted $Fe-6.9\%$wt si soft magnets," *Materials Characterization*, vol. 143, pp. 144 – 151, 2018, metal Additive Manufacturing: Microstructures and Properties.

[42] K. J. Jhong, W.-C. Huang, and W. H. Lee, "Microstructure and magnetic properties of magnetic material fabricated by selective laser melting," *Physics Procedia*, vol. 83, pp. 818 – 824, 2016, laser Assisted Net Shape Engineering 9 International Conference on Photonic Technologies Proceedings of the LANE 2016 September 19-22, 2016 Fürth, Germany.

[43] S. Lammers, G. Adam, H. J. Schmid, R. Mrozek, R. Oberacker, M. J. Hoffmann, F. Quattrone, and B. Ponick, "Additive manufacturing of a lightweight rotor for a permanent magnet synchronous machine," in *2016 6th International Electric Drives Production Conference (EDPC)*, Nov 2016, pp. 41–45.

[44] M. Garibaldi, I. Ashcroft, J. Lemke, M. Simonelli, and R. Hague, "Effect of annealing on the microstructure and magnetic properties of soft magnetic fe-si produced via laser additive manufacturing," *Scripta Materialia*, vol. 142, pp. 121 – 125, 2018.

[45] T. Niendorf, S. Leuders, A. Riemer, H. Richard, T. Tröster, and D. Schwarze, "Highly anisotropic steel processed by selective laser melting," *Metallurgical and Materials Transactions B*, vol. 44, 08 2013.

[46] M. Garibaldi, I. Ashcroft, M. Simonelli, and R. Hague, "Metallurgy of high-silicon steel parts produced using selective laser melting," *Acta Materialia*, vol. 110, pp. 207 – 216, 2016.

[47] C. L. Cramer, P. Nandwana, J. Yan, S. F. Evans, A. M. Elliott, C. Chinnasamy, and M. P. Paranthaman, "Binder jet additive manufacturing method to fabricate near net shape crack-free highly dense fe-6.5 wt.% si soft magnets," *Heliyon*, vol. 5, no. 11, p. e02804, 2019.

[48] *Standard Test Method for Direct Current Magnetic Properties of Low Coercivity Magnetic Materials Using Hysteresigraphs*, ASTM International Std. ASTM A773/A773M-14, 2014.

[49] S. Tumanski, *Handbook of Magnetic Measurements*, ser. Series in Sensors. CRC Press, 2016. [Online]. Available: https://books.google.at/books?id=s0npF4E5jasC

[50] *Standard Test Method Alternating-Current Magnetic Properties of Toroidal Core Specimens Using the Voltmeter-Ammeter-Wattmeter Method*, ASTM International Std. ASTM A927/A927M-18, 2018.

[51] Y. Zhang, L. Poli, E. Garratt, S. Foster, and A. Roch, "Utilizing fused filament fabrication for printing iron cores for electrical devices," *3D Printing and Additive Manufacturing*, vol. 7, no. 6, pp. 279–287, 2020.

[52] *Standard Test Method for Direct Current Magnetic Properties of Low Coercivity Magnetic Materials Using Hysteresigraphs*, ASTM International Std. A773/A773M, 2014.

[53] *Standard Test Method for Alternating-Current Magnetic Properties of Toroidal Core Specimens Using the Voltmeter-Ammeter-Wattmeter Method*, ASTM International Std. A927/A927M, 2018.

[54] J. G. Zhu, J. J. Zhong, V. S. Ramsden, and Y. G. Guo, "Power losses of soft magnetic composite materials under two-dimensional excitation," *Journal of Applied Physics*, vol. 85, no. 8, pp. 4403–4405, 1999.

[55] M. Bali, "Magnetic material degradation due to different cutting techniques and its modeling for electric machine design," Ph.D. dissertation, Technischen Universität Graz, Graz, Austria, april 2016.

[56] J. G. Zhu, J. J. Zhong, Z. W. Lin, and J. Sievert, "Measurement of magnetic properties under 3-d magnetic excitations," *IEEE Transactions on Magnetics*, vol. 39, no. 5, pp. 3429–3431, 2003.

[57] Y. Li, Y. Liu, F. Liu, Q. Yang, and P. Ren, "Magnetic anisotropic properties measurement and analysis of the soft magnetic composite materials," *IEEE Transactions on Applied Superconductivity*, vol. 24, no. 5, pp. 1–4, Oct 2014.

[58] D. X. Chen, J. A. Brug, and R. B. Goldfarb, "Demagnetizing factors for cylinders," *IEEE Transactions on Magnetics*, vol. 27, no. 4, pp. 3601–3619, July 1991.

[59] B. K. Pugh, D. P. Kramer, and C. H. Chen, "Demagnetizing factors for various geometries precisely determined using 3-d electromagnetic field simulation," *IEEE Transactions on Magnetics*, vol. 47, no. 10, pp. 4100–4103, Oct 2011.

[60] S. J. Salon, *Finite Element Analysis of Electrical Machines*. Springer, 1995.